FINAL REPORT

ADAPTABLE STRUCTURAL LOGIC SYSTEM SYNTHESIS WITH BISTABLE SNAP-THROUGH ELEMENTS

Sponsored by
Defense Advanced Research Projects Agency
Strategic Technology Office (STO)
Program: Structural Logic
ARPA Order No. C899/00, Program Code: 0620
Issued by DARPA/CMO under Contract No. HR0011-10-C-0148

Prepared by:

Bing C. Chen, Weiya Zhang
Teledyne Scientific & Imaging, LLC

David Johnson, Manoj Thota, Zhen Wu, Kon-Well Wang
University of Michigan, Ann Arbor

Soobum Lee, Fabio Semperlotti
University of Notre Dame

December, 2012

REPORT DOCUMENTATION PAGE	Form Approved OM8 No. 0704-0188

PLEASE DO NOT RETURN YOUR FORM TO THE ABOVE ADDRESS.

1. REPORT DATE (DD-MM-YYYY)	2. REPORT TYPE	3. DATES COVERED (From - To)
31-12-2012	FINAL REPORT	24-09-2010 to 31-12-2012

4. TITLE AND SUBTITLE

ADAPTABLE STRUCTURAL LOGIC SYSTEM SYNTHESIS WITH BISTABLE SNAP-THROUGH ELEMENTS

5a. CONTRACT NUMBER

HR0011-10-C-0148

5b. GRANT NUMBER

DARPA STO-BAA-10-54

5c. PROGRAM ELEMENT NUMBER

6. AUTHOR(S)

Bing C. Chen, Weiya Zhang, David Johnson, Manoj Thota, Zhen Wu, Kon-Well Wang, Soobum Lee, and Fabio Semperlotti

5d. PROJECT NUMBER

71354

5e. TASK NUMBER

001 to 002

5f. WORK UNIT NUMBER

N/A

7. PERFORMING ORGANIZATION NAME(S) AND ADDRESS(ES)

Defense Advanced Research Projects Agency, Strategic Technology Office
675 North Randolph Street, Arlington, VA 22203-2114

8. PERFORMING ORGANIZATION REPORT NUMBER

Final Report

9. SPONSORING/MONITORING AGENCY NAME(S) AND ADDRESS(ES)

Teledyne Scientific and Imaging, LLC
1049 Camino Dos Rios, Thousand Oaks, CA, 91360

10. SPONSOR/MONITOR'S ACRONYM(S)

DARPA STO

11. SPONSOR/MONITOR'S REPORT NUMBER(S)

N/A

12. DISTRIBUTION/AVAILABILITY STATEMENT

Approved for public release; distribution unlimited

13. SUPPLEMENTARY NOTES

20130118009

14. ABSTRACT

A passive structural logic system composed of bistable snap-through elements and synthesized into structural system with both high stiffness and high damping characteristics was developed. This system was demonstrated to achieve high damping performance and mitigate the shock and vibrations applied by dynamic environments. A ten-cell sub-assembly prototype structural system in axial configuration was designed, fabricated, and characterized to reach loss factor exceeding 1.0 A planar version of sub-assembly beam consists of honeycomb core and hybrid planar bistable snap-through elements was also synthesized, fabricated, and tested to reach loss factor exceeding 1.0 for frequency spectrum from 1 to 10 Hz. A framework to synthesize structural networks of multiple sub-assemblies was developed and allows exploring different serial and/or parallel connection between building blocks and sub-assemblies. The results show that the synthesized structural logic system can become an effective vibration suppression system adaptive to input amplitude and frequencies for sinusoidal and impulse loadings.

15. SUBJECT TERMS

bistable structure, negative stiffness, snap-through, high damping structure, vibration suppression

16. SECURITY CLASSIFICATION OF:			17. LIMITATION OF ABSTRACT	18. NUMBER OF PAGES	19a. NAME OF RESPONSIBLE PERSON
a. REPORT	b. ABSTRACT	c. THIS PAGE			Bing C. Chen
unclassified	unclassified	unclassified	Same as Report (SAR)	75	19b. TELEPHONE NUMBER (Include area code) 805-373-4288

I. TASK OBJECTIVE

The main goal of this program to develop an innovative structural logic system composed of adaptable bistable snap-through periodic element and synthesized into structures system with both high stiffness and high damping characteristics and mitigate the shock and vibrations applied by dynamic environments. Task 1 objective demonstrates the concept of snap-through device building blocks that can ultimately be assembled into structures with high stiffness and damping. Task 2 objective demonstrate using constituent building block element and be integrated to construct adaptive sub-assemblies. To achieve Task 2 objective, we specifically developed a design and optimization framework to synthesize structural logic assemblies based on an available library of structural elements (building blocks). In particular, we explored the following areas:

1. **Development of a prototype bistable oscillator as basic building block library:** Bistable structure element exhibit two stable equilibrium states and the snap-through quickly transitions from one equilibrium state to the other. Analytical analysis and experimental verification were developed to demonstrate the high damping properties associated with snap-through phenomenon.

2. **Development of a general framework for the design and optimization of mechanical assemblies and sub-assemblies based on an existing library of structural elements**: a Matlab-Simulink based analysis tool was developed to provide optimization and integration capabilities for structural logic components. In addition, we developed a Genetic Algorithm (GA) based optimization approach in order to identify optimal design parameters for the constitutive building blocks. This technique was intended to be applied to both the periodic rod and the composite beam assembly to support the final prototype design. We then extended the GA based framework to synthesize structural networks (i.e. an ensemble of multiple sub-assemblies). This extended framework formulation allows exploring different connection conditions (e.g. series, parallel, etc.) between building blocks and sub-assemblies. The main objective was to explore the possibility to further improve the performance and the passive adaptive characteristics of the sub-assemblies by using them in network configurations. The three areas of work are schematically summarized in Figure VIII-.

3. **Development of sub-assembly prototypes for program metrics demonstration:** We investigated several ways to synthesize the subassembly system. Two major configurations were developed to demonstrate high stiffness/high damping program metrics: (1) rod-configuration of nonlinear absorber with snap-through device, and (2) planar-configuration of vibration absorber with snap-through device. These two sets of demonstration prototypes structures developed serves as the most general implementation forms of a military structural platform which can respond to dynamic excitation of environmental shock and vibration.

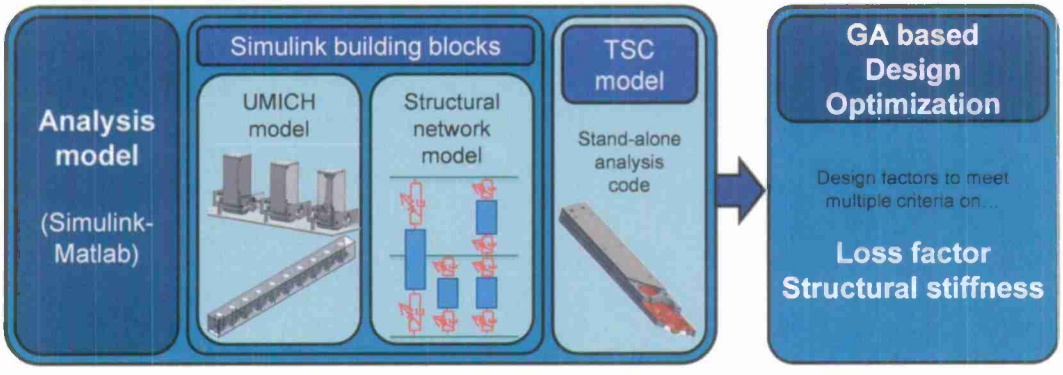

Figure I-1: Schematic of the structural design platform for the design and optimization of structural logic assemblies with concurrent high stiffness/high damping performance.

II. TECHNICAL PROBLEMS

Bistable snap-through elements are used as the basic building blocks to be synthesized into sub-assembly structures, and then incorporated into representative structure to increase overall structural damping. Bistable structures exhibit two stable equilibrium states. The transition from one stable position to the other is achieved by a strongly nonlinear mechanism, known as snap-through. This unstable shape-changing event can be considered as a form of motion amplification as the actuation stroke required to transition the bistable structure from one stable equilibrium position to the other is a fraction of the displacement the bistable structure undergoes.

System with multiple states of equilibrium is considered as a simple realization of nonlinear energy sink. When such a nonlinear energy sink is attached to the main structure, the energy pumping phenomenon from the main structure to the attached structure with multiple equilibrium states has been demonstrated. The energy pumping phenomenon is a controlled one-way channeling of vibrational energy to the attached nonlinear structure. As a result, vibrations of a linear structure subjected to an external excitation can be attenuated via such energy pumping. Figure II-1 illustrates this energy pumping phenomenon from a beam structure to the attached bistable structure of a shallow arch.

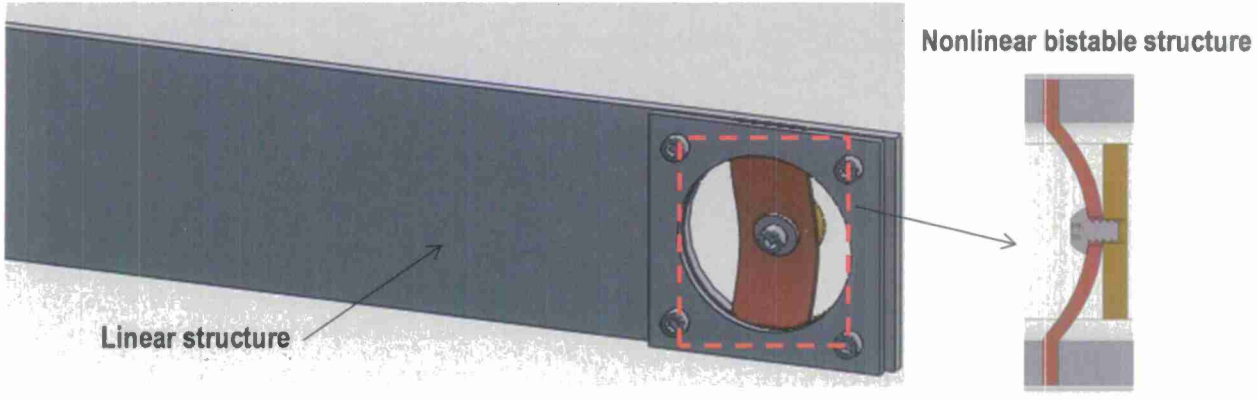

Figure II-1: Beam structure with attached nonlinear bistable structures for energy pumping

The illustrated bistable snap-through element is realized by a shallow arch with an isolated mass placed at the middle of the arch. Due to its geometrical configuration, the transverse deflection of the arch takes on the cubic nonlinear stiffness. When such nonlinear devices are attached to the beam, the one-way channeling of energy from the beam to the attached bistable snap-through element is observed. We have use experiment method to characterize transient responses, after the stoppage of external excitation and observed significant vibration attenuation

In addition to the shallow arch structure demonstrated in Figure II-1, there are many potential implementations. A snap-through truss, a buckled beam, and bistable composite plate, are just a few examples structure which can be implemented as dynamically inducing bistable snap-through damping devices to achieve high damping performance.

The most critical feature shared among these bistable structures is the cubic nonlinearity in stiffness and the associated "W-shape" double-well potential energy well. The force-displacement curve of a generic bistable structure, such as the shallow arch structure, is shown in

Figure II-2. This cubic stiffness nonlinearity was experimentally characterized and can be curve-fit by a 3rd order polynomial. The negative slope region between the two critical loads for the structure to undergo snap-through motions results in significant increase in the energy dissipation and is the underlying physics attributing to high damping mechanism. Detailed elaboration on the concept, modeling and characterization will be presented in the following sections

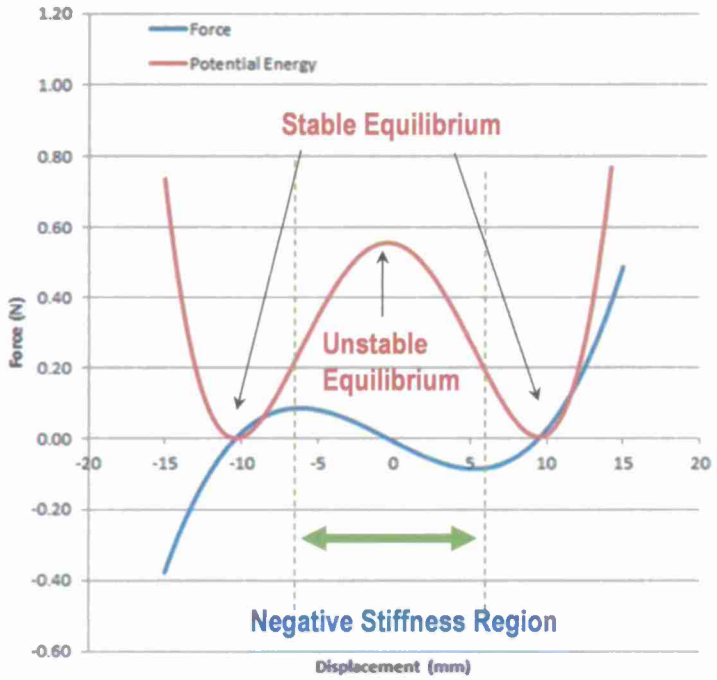

Figure II-2: Cubic stiffness nonlinearity of bistable structure and its W-shape double-well potential energy

In terms of a potential energy function, the two statically stable configurations of a bistable structure correspond to stable equilibria points separated by an unstable equilibrium. The force-displacement curve and its associated 'double-well' potential energy function (in red color) are depicted in Figure II-2. To trigger snap-through from one stable state to the other, sufficient energy needs to be put into the system such that it is pushed up and over the energy hilltop separating the two potential wells. Imagine a ball representing system's state. The dynamic response of a bistable structure is restricted to oscillations confined to one stable state unless enough energy is put into the system to elevate its state beyond the hilltop. In physical terms, this hilltop analogy is defined as a force threshold or critical load. The critical force of bistable structure is the most critical parameter of bistable snap-through element.

III. GENERAL METHODOLOGY

(III.1) Relevant Prior Work

Investigations have been conducted to achieve adaptable damping with passive designs. Cho, et al [67] recognized the complexity of using magnetorheological (MR) damping systems on large structures: many MR dampers are needed, along with a multitude of power supplies, sensors, and control electronics in order to make the system function. They devised a passive MR damper which incorporates an electromagnetic induction system (EMI). The EMI supplies electricity to activate the MR damper in proportion to vibration motion, thus providing adaptable damping in a passive manner. They show computationally that this strategy has either comparable or better performance than a typical semi-active MR damping system for several examples. Choi, et al [8] successfully demonstrated the feasibility of using an EMI system to dynamically alter the damping properties of an MR damper via laboratory testing.

In recent years, there have been some interesting studies on designing strongly nonlinear devices to enhance structural damping in a passive manner. Vakakis, et al [46] have conducted studies of essentially nonlinear (non-linearizable) structural attachments which are commonly called Nonlinear Energy Sinks (NES). The NES causes broadband, passive, and irreversible energy transfer from the host structure, which was generally assumed to have linear dynamics before attaching the NES. The NES can maintain high damping across a broad frequency range. Some researchers have studied fitting structures with nonlinear devices having multiple stable equilibrium states. Buzhinskii [5] presented a simplified model and laboratory experiment of a snap-through oscillator for limiting the response of its host structure. Avramov and Mikhlin [3] investigated a snap-through truss as an attachment to a (previously) linear host structure as a means of absorbing vibration. Gendelman and Lamarque [15] studied the free response dynamics and energy transfer of a nonlinear attachment with multiple states of equilibrium, uncovering three regions of behavior depending on initial conditions and system specifications.

Structures incorporating negative stiffness elements have also been investigated to produce high damping performance in a passive manner. Lakes, *et al* [20, 21, 22] studied negative stiffness inclusions in a positive stiffness matrix, demonstrating that the damping of the overall material is many times larger than common materials. Wang and Lakes [48] investigated the stability and dynamics of a lumped parameter viscoelastic element which incorporates negative stiffness, demonstrating the high damping and the stability of the system. On a structural level, Li, *et al* [24] found that the optimum value of stiffness in certain bridge connections is a negative value in order to produce the maximum damping in the structure.

(III.2) Snap-through Oscillator

Inspired by some of the prior studies which use nonlinear elements to enhance damping passively, a passive bistable damped oscillator for producing high and adaptable damping via snap-through actions is explored. As will be described further in following sections, the device under consideration has two stable equilibria separated by an unstable equilibrium. In between the two stable equilibria is a region of negative stiffness. The dynamic transition between the two stable equilibria is rapid and sweeps out a large stroke, so including viscous damping could provide high levels of energy dissipation. These features are highlighted in the schematic and accompanying plot in Figure II. Additionally, there could be at least two response regions – one of small amplitude motion around one stable equilibrium, and one of large amplitude motion

about both stable equilibria. Transition between these regimes could lead to different levels of loss factor.

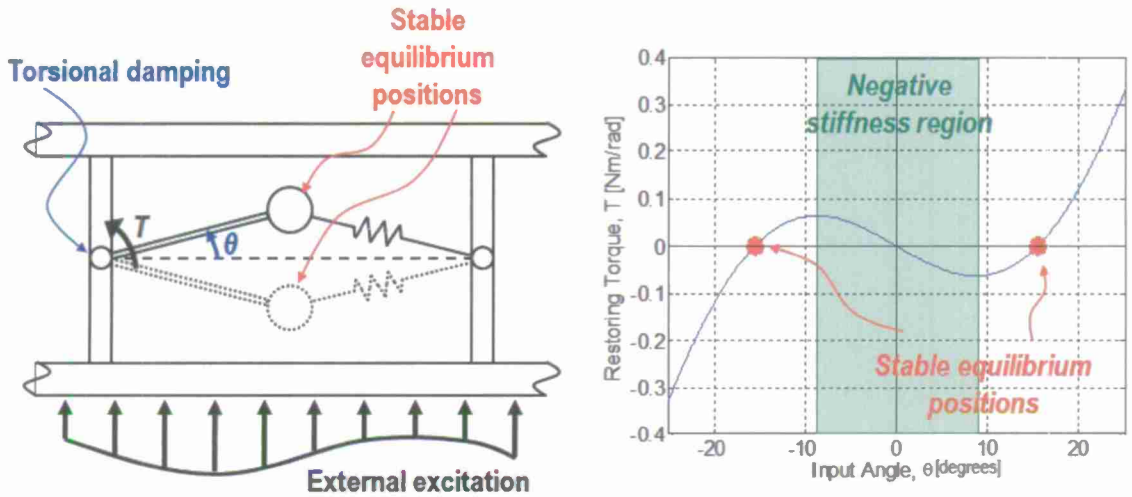

Figure III-1: Schematic of a bistable oscillator and a plot of restoring torque vs. input angle, showing a negative stiffness region.

Due to a change in input conditions, the response of the device could change significantly and yield useful effects:

- Relatively high damping due to the large motion (high displacement and velocity) generated as the device experiences snap-through and oscillates between the stable equilibrium positions.

- Passively adaptable damping, as the energy dissipation loss factor can change significantly depending on input amplitude and frequency.

To demonstrate these points, numerical analysis and experimental investigations are performed.

(III.3) Subassembly Synthesis

We've investigated several ways to synthesize the subassembly system. For brevity of the report, two configurations are presented to demonstrate the concept: nonlinear absorber with snap-through device and vibration absorber with snap-through device. Numerical integration method is applied in all the analysis.

The first of the topologies for subassembly we investigated is to integrate nonlinear absorber together with snap-through device. From previous study, we found out that as frequency and input amplitude increase, loss factor will increase for nonlinear absorber. However, it tends to deliver low loss factor for low frequencies and input amplitudes. To achieve a high loss factor throughout all frequencies, we propose to additionally design snap-through device to cover low frequencies range.

For the second topology is to combine vibration absorbers with snap-through devices. The main idea is to utilize the effect of designed vibration absorber to attenuate the vibration of main structural member and effective trigger the bistable device to dissipate out the energy.

IV. TECHNOLOGY RESULTS

(IV.1) Development of Bistable Snap-Through Element as Basic Building Blocks

Modeling of a Single Rotational Snap-Through Oscillator

A model of an inertially activated bistable oscillator is presented in this section to characterize the dynamics of such a device and also to investigate the possibility of creating a structure that can meet the Task 1 metric of loss factor higher than 0.5 ($\eta > 0.5$) and also can adapt to changes in the input. A schematic of such a device is given in Figure IV-1. In this depiction, the oscillator is situated between the plates of a sandwich panel with the pivots of the device attached to the supporting ribs of the panel. As the panel is excited (here, in the form of prescribed displacement $y(t) = Y\cos(\omega t)$, where Y is the excitation amplitude and ω is the excitation frequency), motion is transferred to the mass m via the rigid link of length R and the lumped spring of unstretched length l_0, where the configuration of the system with the spring unstretched is depicted in the schematic. The lumped spring has linear spring constant k, where k is the linear proportionality constant relating the force and spring deflection in the lengthwise direction of the spring. Here, lateral bending of the spring is not considered, only lengthwise deformation. L describes the distance between the two pivots where the rigid rod and the spring connect to the internal ribs of the sandwich panel. A viscous torsional damper with damping constant c_t is applied at the pivot between the rigid rod and the rib of the sandwich panel. Finally, the position of the mass is described by θ, the angle between the horizontal and the rigid link.

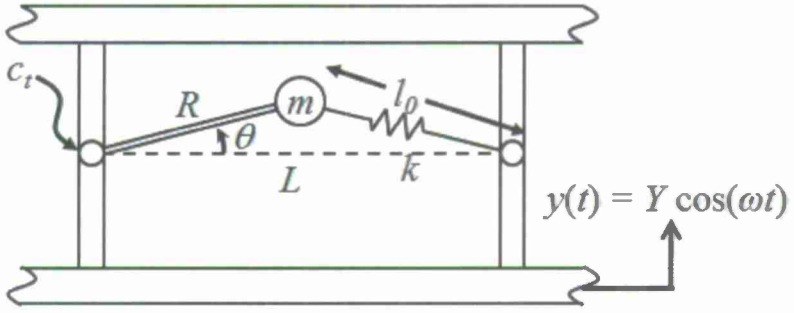

Figure IV-1: Schematic of an inertially activated bistable snap-through oscillator.

The equation of motion for this device is derived using dynamic force balance:

$$mR^2\ddot{\theta} + c_t\dot{\theta} + \frac{kLR\left(\sqrt{R^2 + L^2 - 2LR\cos\theta} - l_0\right)}{\sqrt{R^2 + L^2 - 2LR\cos\theta}}\sin\theta = mYR\omega^2\cos\omega t\cos\theta \tag{1}$$

where each over-dot denotes one-time derivative. Setting time derivatives and excitations to zero and solving for θ gives the equilibrium positions of the mass with respect to the frame:

$$\theta = 0 \tag{2a}$$

$$\theta = \cos^{-1}\left(\frac{L^2 + R^2 - l_0^2}{2LR}\right) \tag{2b}$$

$$\theta = -\cos^{-1}\left(\frac{L^2 + R^2 - l_0^2}{2LR}\right) \tag{2c}$$

These are the three equilibrium angles for $-\pi/2 < \theta < \pi/2$. An eigenvalue analysis of the linearized equation of motion shows that (2a) is an unstable equilibrium while (2b) and (2c) are stable equilibria as long as the free length of the spring plus the length of the rigid link is greater than the horizontal distance between the pivots; i.e., $l_0 + R > L$ (in other words, the spring is compressed when $\theta = 0$). Incidentally, if $l_0 + R \leq L$, then the system has a single stable equilibrium position at $\theta = 0$ and no longer exhibits bistable behavior.

Derivation of Loss Factor

Many measures of damping which work well for linear systems become undefined for nonlinear systems such as the bistable snap-through oscillator. For example, the method of logarithmic decrement is not applicable since free response will occur in at least two regimes: one of orbits about both stable equilibria, followed by a region of orbits about only one stable equilibrium. Presumably, the logarithmic decrement would be different in each of these regions. Methods using the hysteresis loop also have concerns. The area enclosed by the hysteresis loop gives the energy dissipated per cycle by the structure. However, the response of a nonlinear structure can have many harmonics of the input, and can also be aperiodic or chaotic in nature. These types of responses may not form an enclosed loop, so it is difficult to calculate the energy dissipated using this method in such cases.

Adapting the concept of loss factor gives one viable method for quantifying the energy dissipation of the device. The spirit of loss factor is to calculate the energy dissipated by the structure per radian of input excitation divided by the maximum energy stored by the structure. These are basic engineering quantities which are fairly straightforward to measure, particularly for the system under consideration.

The maximum energy stored in the structure is taken to be the maximum of the kinetic energy plus the potential energy:

$$\Pi = \max(KE + PE) = \max\left(\tfrac{1}{2} mR^2\theta^2 + \tfrac{1}{2} k\delta^2\right), \tag{3}$$

where the deflection of the spring δ can be derived from the kinematics of the device and is expressed as:

$$\delta = \sqrt{R^2 + L^2 - 2LR\cos\theta} - l_0. \tag{4}$$

Note that the argument of the max function, i.e., the total stored energy, in (3) is time varying since the kinetic and potential energies in the system are varying dynamically as the system vibrates. Taking the maximum value of the total stored energy during the time segment of response under consideration removes the time dependence of the stored energy, creating a single number which can be used in the calculation of loss factor.

The energy dissipated per radian is computed by way of the power dissipated by the device. The instantaneous power dissipated by the device over time is the resistive torque generated by the viscous damper multiplied by the angular velocity of the inertial element:

$$P_i(t) = T_{damper}(t)\dot{\theta}(t) = \left[c_t\dot{\theta}(t)\right]\left[\dot{\theta}(t)\right] = c_t\theta^2 . \tag{5}$$

Averaging (5) for a time segment of length τ gives the average power dissipated:

$$P_{avg} = \frac{1}{\tau}\int_0^{\tau} P_i(t)dt . \tag{6}$$

The excitation period of the device is given by $T = 2\pi/\omega$; the time needed for one radian of excitation to take place is $t_r = T/2\pi$. Then, the energy dissipated by the device per radian of excitation is

$$D = P_{avg}t_r = \frac{P_{avg}}{\omega} . \tag{7}$$

where, again, ω is the excitation frequency in radians per second. Putting together (3) and (7), the loss factor can be computed as

$$\eta = \frac{D}{\Pi} . \tag{8}$$

Numerical Analysis a Single Rotational Snap-Through Oscillator

Equation (1) is numerically integrated in order to analyze the response of the device and to compute the loss factor for different input conditions. Some example responses of the device are given in Figure IV-2. Parameters selected for the simulations are m = 0.4 kg, c_t = 0.012 N-s/m, k = 1400 N/m, l_0 = 0.055 m, L = 0.106 m, and R = 0.055 m.

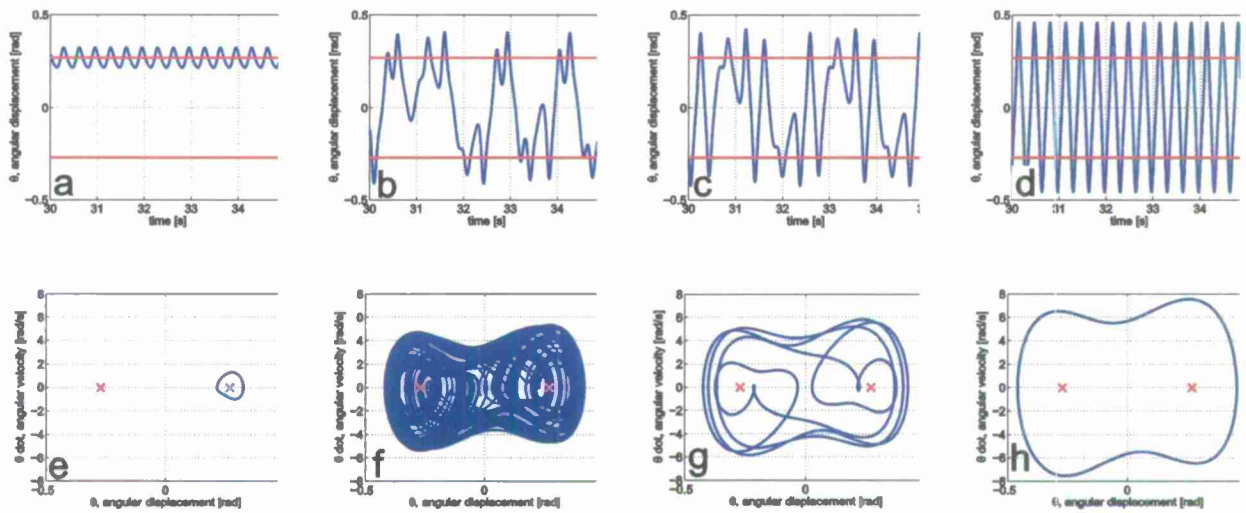

Figure IV-2: Time response (a – d) and phase diagrams (e – h) for the response to base excitation of the bistable device. Four levels of base excitation amplitude are given: 5 mm (a, e), 10 mm (b, f), 11 mm (c, g), and 13.5 mm (d, h).

The structure is excited at 3 Hz while varying the base excitation amplitude Y among 5 mm (Figure IV-2a,e), 10 mm (Figure IV-2b,f), 11 mm (Figure IV-2c,g), and 13.5 mm (Figure IV-2d,h). Figure IV-2a-d shows the time response, output angle θ vs. time, for an interval of steady state motion. In Figure IV-2e-h, the phase diagrams – the output angular velocity $d\theta/dt$ vs. output angle θ – are plotted. Four different response types in three different response regimes are observed. For smaller excitation amplitudes, the device exhibits small amplitude response of oscillations about one of the stable equilibria. This is shown in Figure IV-2a,e by low orbits around one of the stable equilibria. The stable equilibria are indicated by the two horizontal lines in the time response plots and by the two crosses in the phase plot. For relatively high levels of excitation amplitude, the device undergoes periodic snap-through, where there are clear, high, and periodic orbits of response about both stable equilibria as in Figure IV-2d,h. In between these regimes there is a transition regime where complicated dynamic response is possible. Responses in the transition regime may consist of either aperiodic motion (Figure IV-2b,f) or multiharmonic motion (Figure IV-2c,g). Regimes of either aperiodic or multiharmonic motion are small and intermingled with each other, so we lump both of these types of responses into one *transition* regime which clearly lies between the small and large response regimes. These four types of responses are also reported in for a snap-through oscillator.

Before computing the loss factor for this device, (6) will be investigated to determine whether or not the average power dissipated by the device converges. It seems reasonable that the average power dissipated for periodic motion, such as in the small response (Figure IV-2a,e), multiharmonic response (Figure IV-2c,g) and periodic snap-through (Figure IV-2d,h) regimes would converge to a constant value since each trajectory repeats cyclically. In the case of aperiodic snap-through (Figure IV-2b,f), there is no repeatable trajectory nor cyclic motion, so there is no indication that the power dissipated would necessarily converge to a constant value.

Using (7), we can illustrate that for all response regimes, the average power dissipated does indeed converge as long as a sufficient time segment of response, τ, is considered. In figure 4, average power dissipated is calculated over a time segment of response of length τ. so the plots attempt to show that as more data is averaged, the power converges to a relatively constant value. These results are shown in Figure IV-3, where convergence bounds of ±5% (black, dotted, horizontal lines) and ±2% (red, dashed, horizontal lines) of the final value (taken to be at 400 seconds) are also indicated. Note that the small response, multiharmonic response, and periodic snap-through regimes (Figure IV-3a, c, and d, respectively) converge to their final value quite quickly. In the aperiodic case, the convergence is slower, requiring about 10 seconds of response to be averaged in order to settle inside the 5% bound according to this example. About 190 seconds of response is needed to converge inside the 2% bound. Nevertheless, as long as enough data is averaged, the average power dissipated by the device converges to a relatively constant value, even for the case of aperiodic response.

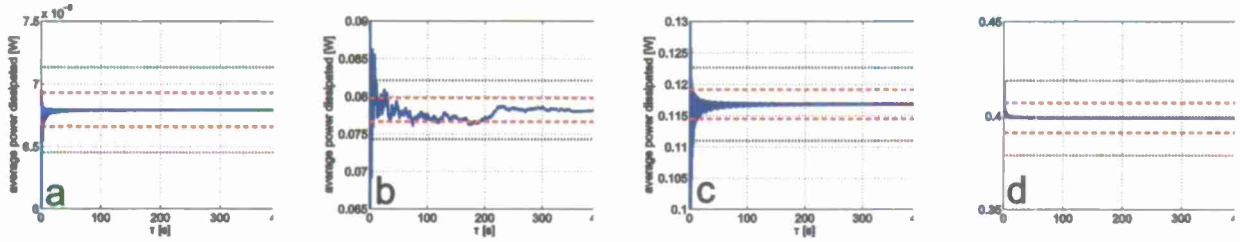

Figure IV-3: Average power dissipated vs. length of averaged time segment of response (blue, solid line). Convergence bounds for ±5% (black, dotted lines) and ±2% (red, dashed lines) of the final value are also drawn. Results show that the average power computed by (7) converges, even for aperiodic response. Figures a – d here correspond to Figure IV-2a – d, respectively.

Evidence of convergence of average power for aperiodic responses is further shown in Figure IV-4. Average power vs. τ is plotted for several combinations of system and excitation parameters which produce aperiodic response, and convergence is observed in all cases. Phase diagrams of the response are produced in plots a-d and the corresponding average power is plotted in e-g, respectively.

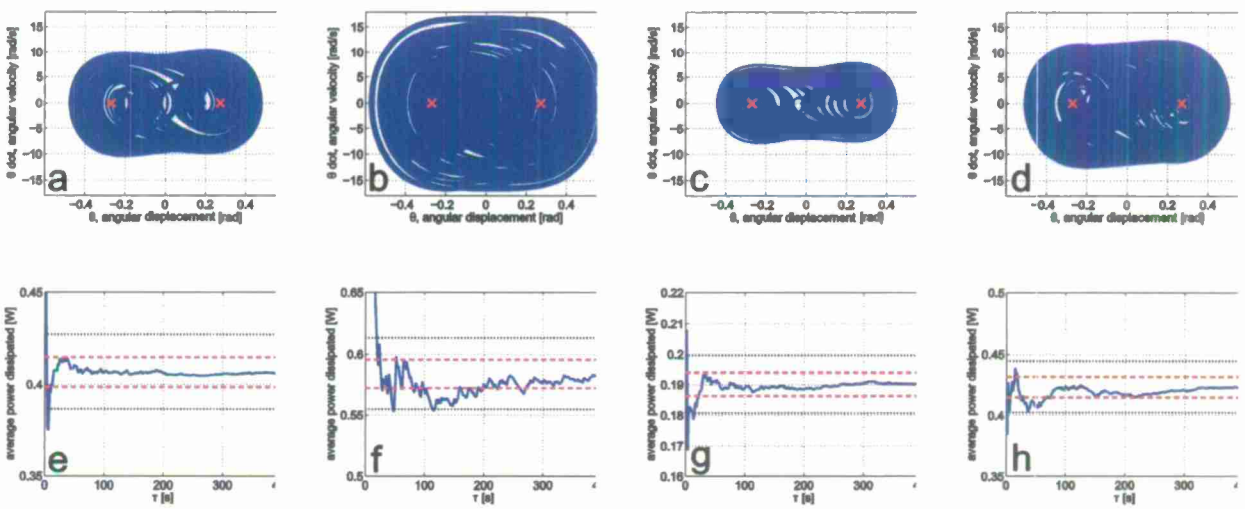

Figure IV-4: Examples of aperiodic response (a-d) and corresponding evidence of convergence of average power (e-h) for a variety of system and input parameters.

Using (8), the loss factor can be calculated for the device for various input frequencies and amplitudes. Figure IV-5 shows a plot of loss factor vs. input amplitude for an input frequency of 3 Hz. At lower amplitudes where the device response is small, the loss factor is also low, but when the input amplitude grows larger, eventually the device exhibits periodic snap-through and there is a significant increase in the loss factor. In this case, the snap-through motion increases the loss factor by more than a factor of 3 compared with small amplitude orbits. The onset of this abrupt change in system behavior and increase in loss factor is called the *snap-through threshold*.

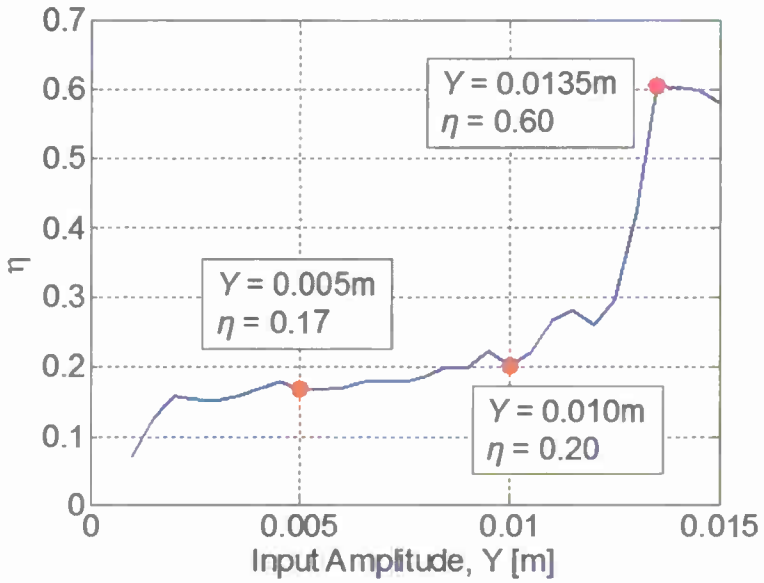

Figure IV-5: Loss factor vs. input amplitude profile for the bistable oscillator.

To demonstrate the device performance in terms of loss factor over varying input amplitude and frequency, a 3-dimensional (3D) surface plot is generated (Figure IV-6). Overall, the plot demonstrates that the device is predicted to exceed the Task 1 loss factor metric of $\eta > 0.5$. Additionally, the adaptability of the device to change loss factor depending on input frequency and amplitude is demonstrated. Some interesting performance features are highlighted in the figure. First, the snap-through threshold is indicated by a dashed line, and this amplitude, which defines the onset of snap-through, changes depending on the excitation frequency. Equivalently, the snap-through threshold defines the frequency at which snap-through occurs given a level of input amplitude. In this way, the device has adaptability to both frequency and amplitude, with the potential to provide a significant change in damping with respect to changes in either input variable. A second observation is that the greatest values for loss factor occur along the snap-through threshold in the periodic snap-through response regime. Thirdly, the three regimes of response are evident in this 3D loss factor surface and are indicated in the figure.

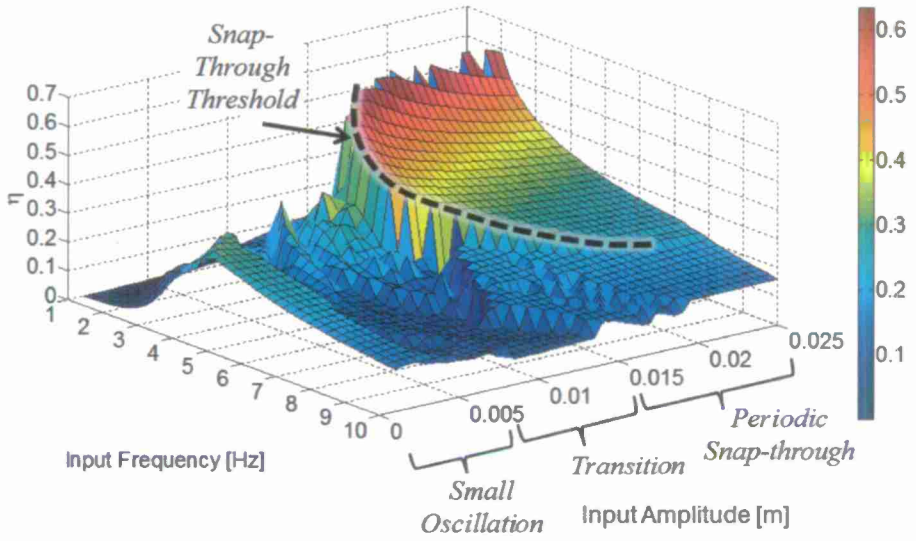

Figure IV-6: Loss factor vs. input frequency and amplitude, with snap-through threshold indicated by the dashed line. The three response regions (small oscillation, transition, and periodic snap-through) are also evident as indicated.

The results shown in Figure IV-7 demonstrate the tuning potential of the device. Two contour maps of the loss factor performance for varying input frequency and amplitude are plotted. In the left pane of Figure IV-7, the parameters are the same as defined above, while in the right pane, m = 0.6 kg and k = 2100 N/m, while other parameters are the same. Two major distinctions can be observed between the two performance plots. First, Device A, which corresponds to the left plot, produces a higher maximum loss factor of around 0.63 than Device B, which corresponds to the right plot and produces maximum loss factor of around 0.34. Second, the snap-through threshold is higher for Device A than for Device B. In short, Device A has higher damping than Device B, but Device A also requires larger input amplitude to reach its maximum loss factor than Device B.

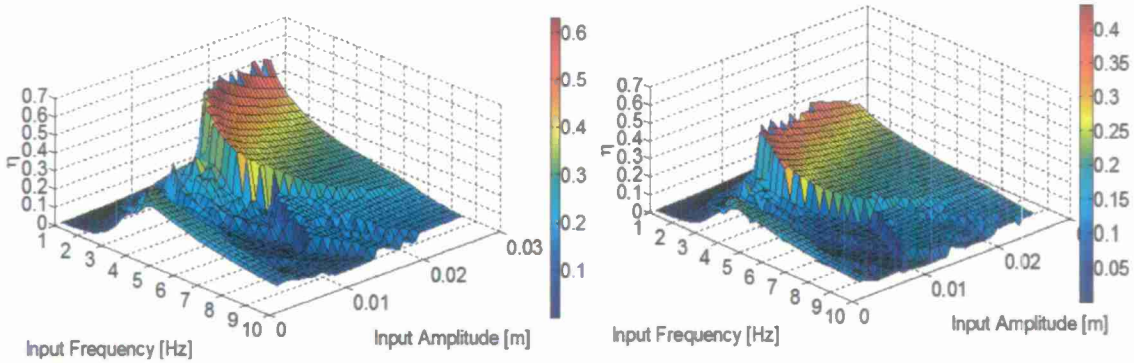

Figure IV-7: Comparison of the loss factor contours for varying input frequency and amplitude for two different device configurations.

Scaling study of a Single Rotational Snap-Through Oscillator

A scaling study of the single rotational snap through oscillator was performed in order to determine whether a device could be rescaled in terms of parameters and still achieve a high performance. Equation (9) shows the nondimensionalized equation of motion (compared with the dimensional equation of motion, Equation (1)), along with the nondimensionalized parameters in Equations (10). The equation is nondimensionalized in an attempt to minimize the number of parameters we need to study.

$$\Theta + \mu_t \Theta + \frac{\sqrt{\beta^2 + 1 - 2\beta\cos\Theta} - \lambda}{\beta\sqrt{\beta^2 + 1 - 2\beta\cos\Theta}} \sin\Theta = \Gamma\cos\bar{\omega}\bar{t}\cos\Theta \tag{9}$$

$$\bar{t} = \omega_n t, \beta = \frac{R}{L}, \lambda = \frac{l_0}{L}, \omega_n^2 = \frac{k}{m}, \mu_t = \frac{c_t}{m\omega_n R^2}, \bar{\omega} = \frac{\omega}{\omega_n}, \Gamma = \frac{Y\bar{\omega}^2}{R} \tag{10}$$

Theoretically, keeping the equation of motion the same will lead to the same performance in the scaled device as in the current device. Observing the equations, one can note the following:

- Scaling the vibration parameters (m, c_t, k) proportionally does not change the equation of motion
- Scaling the geometry (L, R, l_0) proportionally requires a change in input amplitude Y and damping constant c_t to keep the equations of motion the same
- Scaling the geometry (L, R, l_0) proportionally down increases μ_t, making more effective use of available torsional damping

Alternative Design of the Snap-Through Oscillator

As the project progressed toward Task II, the team saw that the rotation snap through device could be improved. An alternative design of the snap through oscillator was created which uses translational motion of the snap through mass instead of rotational motion – see Figure IV-8. As will be discussed in the experiment section, the translational device has few components than the rotational device, which makes the design and assembly simpler, and should lead to a more robust device. The translational device has less complicated dynamics than the rotational device, and we anticipated that it would produce a better model validation.

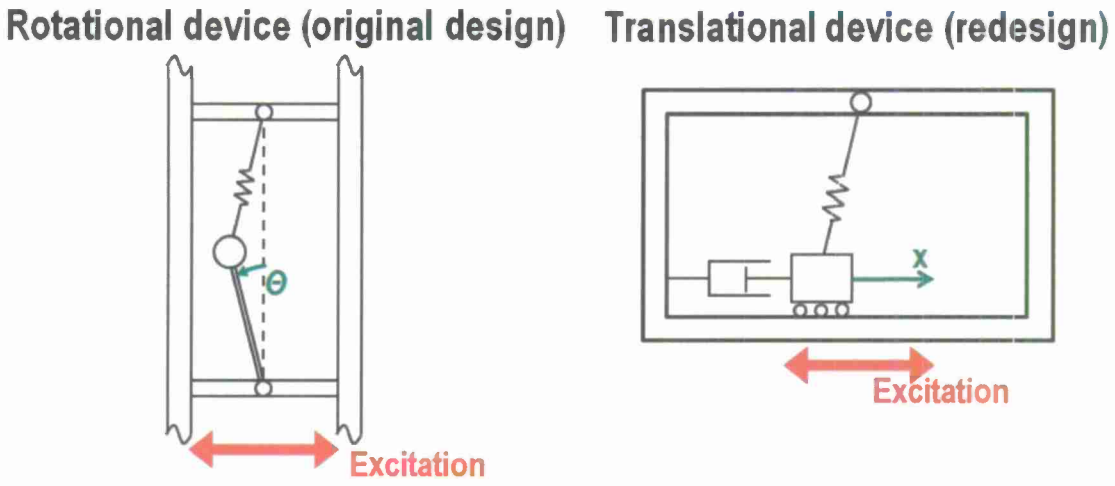

Figure IV-8: Comparison of schematics of rotational snap through device and translational snap through device.

A more detailed schematic of the translational snap through device is provided in Figure IV-9, where m is the oscillating mass, l_0 is the unstretched length of the linear spring with spring constant k. A viscous damper with constant c is attached to the mass. The vertical distance between the spring pivot and the mass is given by d. The motion of the mass is coordinate x while $y(t) = Y\cos(\omega t)$ is the base excitation amplitude of the outer, rigid frame, which represents the load bearing element of the structure. The degree of freedom of the system is specified by $z = x - y$. The equation of motion of the device is

$$m\ddot{z} + cz + kz\left(\frac{\sqrt{z^2 + d^2} - l_0}{\sqrt{z^2 + d^2}}\right) = mY\omega^2\cos(\omega t) \tag{11}$$

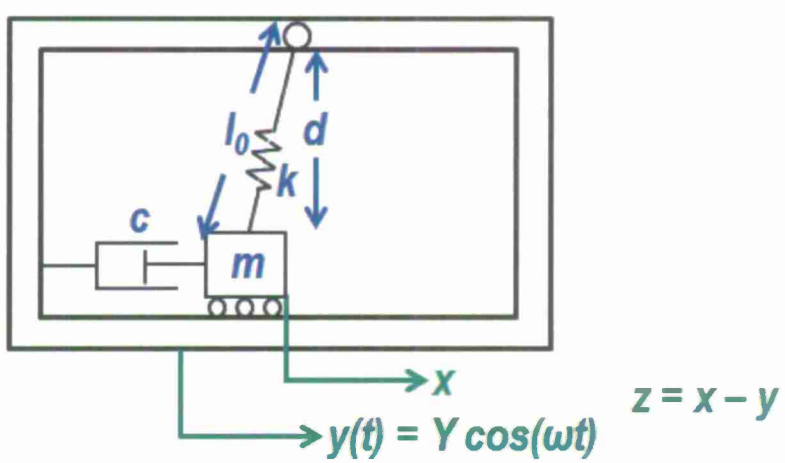

Figure IV-9: Detailed schematic of the translational snap through device.

Parameters chosen for simulation are m = 0.4 kg, c = 7 N-s/m, k = 60000 N/m, d = 0.1 m, and l_0 = 0.1005 m. When excited at 3 Hz, the device exhibits the same qualitative behavior as the rotational device. For example, the small oscillation, transition, and snap through regions of dynamic response are present when the structure is excited at three different base excitation amplitudes; this is demonstrate by the simulation results of Figure IV-10.

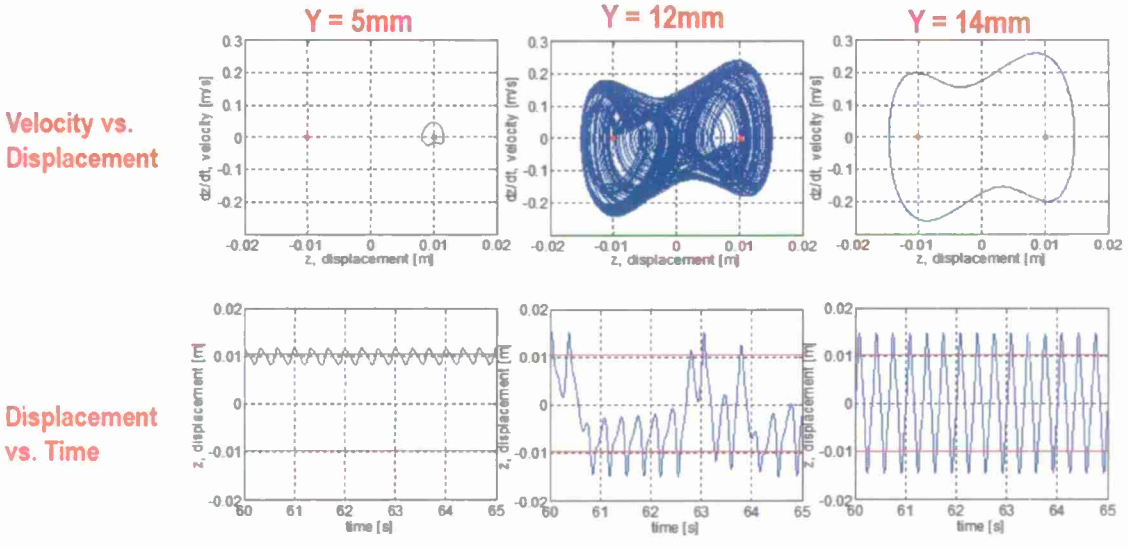

Figure IV-10: Phase diagrams and time histories of the translational snap through device for three different base excitation amplitudes. Regions of small amplitude, transition, and snap through response are present.

Figure IV-11 presents a 3D loss factor performance plot, and the reader will note features which are qualitatively very similar to the rotational snap through device performance in Figure IV-6. The adaptability to frequency and amplitude is demonstrated, and the loss factor is predicted to be in excess of the Task 1 metric of 0.5. Due to the benefits of the translational device compared with the rotational device, the translational device (after experimental validation) is carried forward as the design of choice for Task 2.

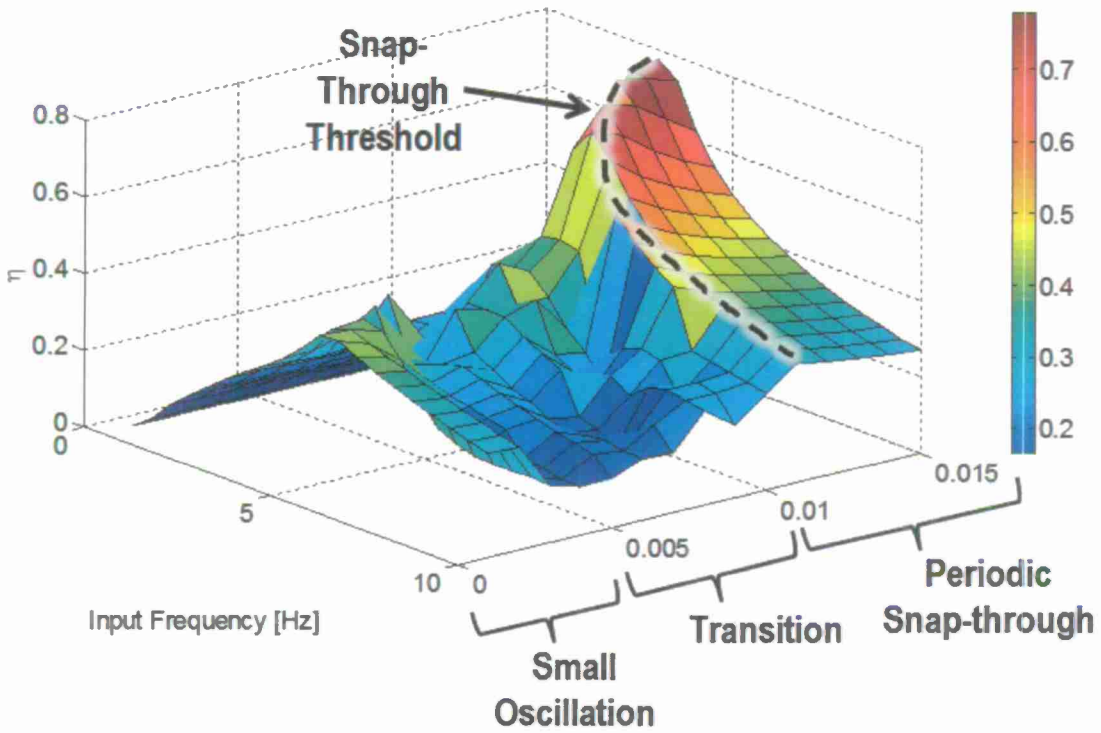

Figure IV-11: 3D loss factor performance plot for the translational snap through device. The results show that the translational device has the same qualitative behavior, as well as potential for adaptability and high loss factor, as the rotational device.

Subassembly Configuration I (nonlinear absorber with snap-through device)

We started with 20 nonlinear resonators and design the systems to have large vibration amplitude for certain resonators (low frequencies resonator) and large vibration amplitude for high frequencies resonators. To improve the performance for low frequencies, we add in snap-through device on top of low frequency resonators. Schematics are shown in Figure IV-12.

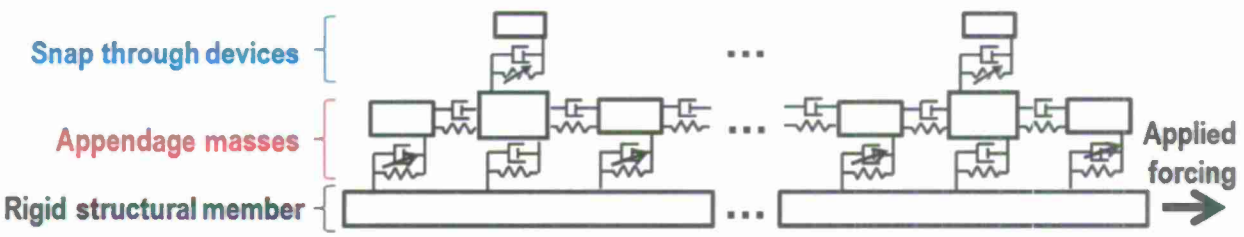

Figure IV-12: Schematic drawing for proposed subassembly structure

One result was shown for loss factor versus frequencies in Figure IV-13. We can see that the hybrid system (system with nonlinear damper and snap-through device) does increase the loss factor of the system for low frequencies. The reason it also increases the loss factor for high

frequency range is that the input force is large enough to excite the snap-through device for all frequencies. However, after exhausted parameter search, we found it difficult to achieve program metric with reasonable add-on mass. Hence, we proposed the second synthesis method.

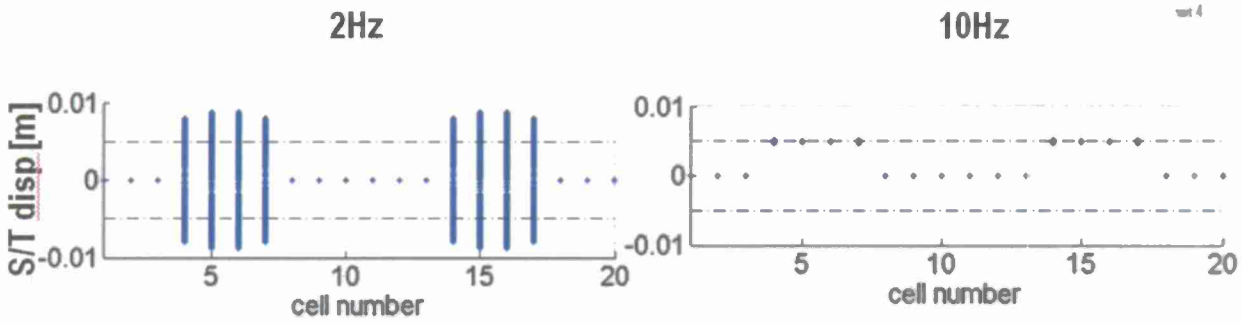

Figure IV-13: Response of the snap-through device for low frequency (2Hz) demonstrating that the devices are triggered as designed.

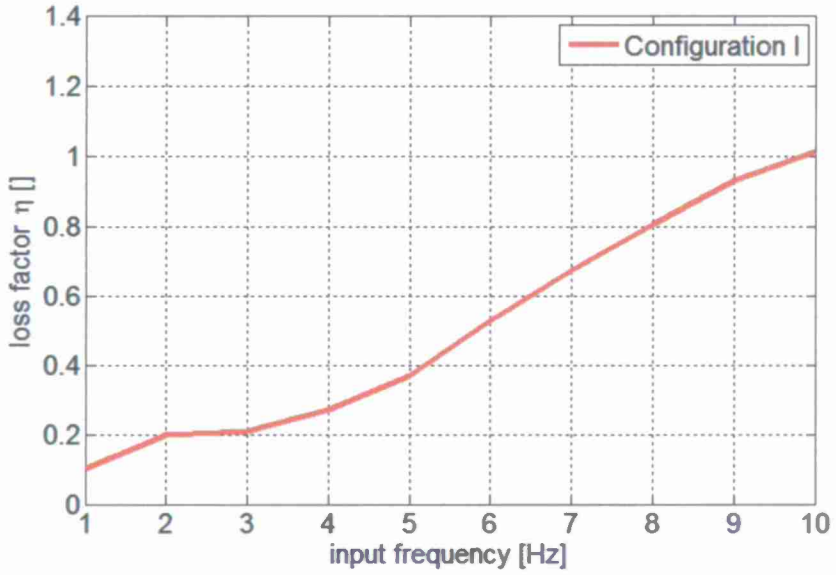

Figure IV-14: Loss factor for performance for configuration I

Sub-assembly Configuration II (vibration absorber with snap-through device)

To achieve a broad band high loss factor performance, we tuned 10 linearized vibration absorbers ranging from 1Hz to 10Hz. The schematic drawing (Figure IV-15) and the simulation result for the system (Figure IV-16) is shown. The equations of motion for i-th snap through device, i-th appendage mass and the structural member are respectively as follows:

$$m_{si}\ddot{x}_{si} + c_{si}\dot{x}_{si} - c_{si}\dot{x}_{ri} + k_{1i}x_{si} - k_{1i}x_{ri} + k_{3i}\left(x_{si} - x_{ri}\right)^3 = 0$$

$$m_{ri}\ddot{x}_{ri} + \left(c_{si} + c_{ci} + c_{ri}\right)\dot{x}_{ri} - c_{si}\dot{x}_{si} - c_{ri}\dot{x}_b + \left(k_{1i} + k_{ci} + k_{ri}\right)x_{ri} - k_{1i}x_{si} - k_{ri}x_b - k_{3i}\left(x_{si} - x_{ri}\right)^3 = 0$$

$$m_b\ddot{x}_b + \sum_{i=1}^{N}\left[c_{ri}\dot{x}_b - c_{ri}\dot{x}_{ri} + k_{ri}x_b - k_{ri}x_{ri}\right] = f$$

where subscript s, r and b stand for snap-through, appendage and structural member respectively.

As it can be seen, we have already achieved loss factor over 1 from 7 to 10 Hz with a reasonably amount of add on mass.

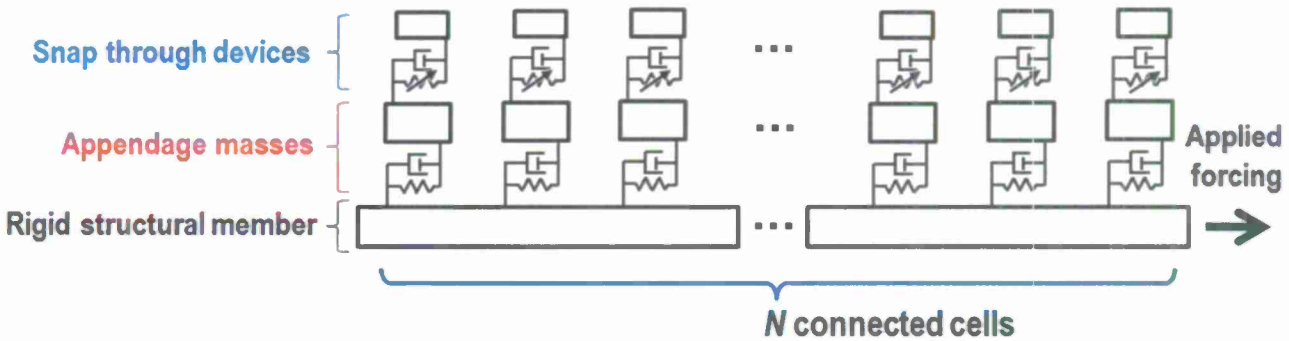

Figure IV-15: Schematic drawing for vibration absorber with snap-through device system.

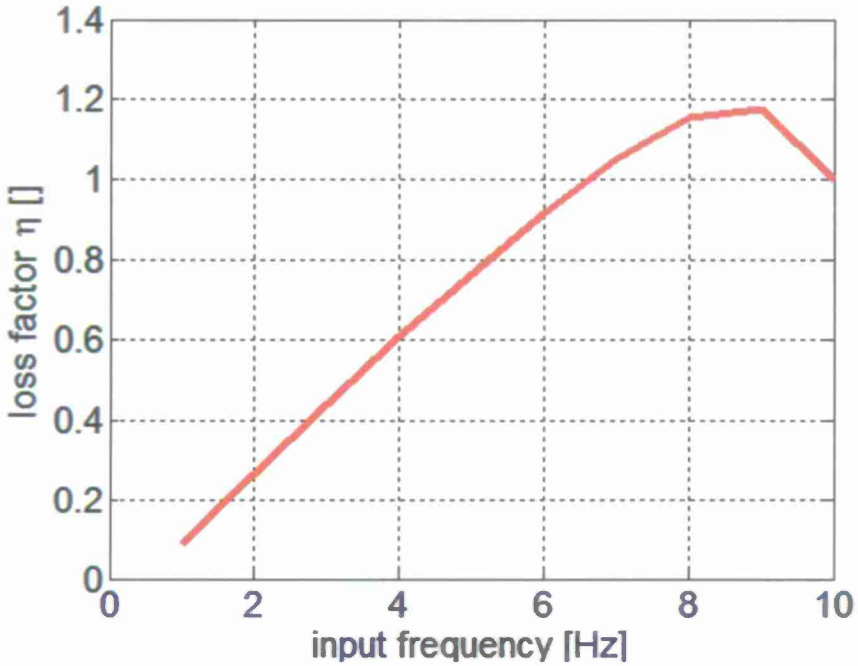

Figure IV-16: Configuration II. At 100 N, loss factor is greater than 1 from 7 to 10Hz

After fine tuning of the parameters, we generated a set of parameters that satisfies Program Task II metric. The finalized parameters are shown in Table Figure IV-1below, where x_0, ks_1, cs, m_s, c_r, m_r, and k_r represents equilibrium position, linear stiffness, mass and damping constant of snap-through device, as well as damping constant, mass and stiffness of appendage mass respectively. The weight of the structural member used in the simulation is 10kg.

Table Figure IV-1: Finalized system parameters from simulation

	X0(m)	Ks1 (N/m)	Cs (N/m/s)	Cr (N/m/s)	Ms (kg)	Mr (kg)	Kr (N/mm)
Cell1	0.009	-7	2.3	1.5	1.1	2.5	0.09
Cell2	0.005	-30	1.5	2.3	1.1	2.2	0.32
Cell3	0.009	-38	2.3	2.3	1.1	2.2	0.75
Cell4	0.013	-16	2.3	1.5	1.1	1.6	0.96
Cell5	0.009	-9	1.5	2	1.1	1.6	1.45
Cell6	0.015	-21	2	2.3	1.1	1.6	2.18
Cell7	0.015	-32	2.3	2.3	1.1	1.8	3.36
Cell8	0.007	-26	1.5	2	1.1	1.6	3.95
Cell9	0.005	-5	2.3	2	1.1	1.6	4.97
Cell10	0.015	-23	2	2.3	1.1	1.6	6.07

The loss factor performance of the sub-assembly system is presented with forcing amplitude at 10N and frequency from 1 to 10 Hz. The result is shown in Figure IV-17, where vertical axis is loss factor value and horizontal axis is frequency. As one can see, the system achieves loss factor performance over 1 from 1 to 10 Hz, satisfying the first requirement of program Task II metric.

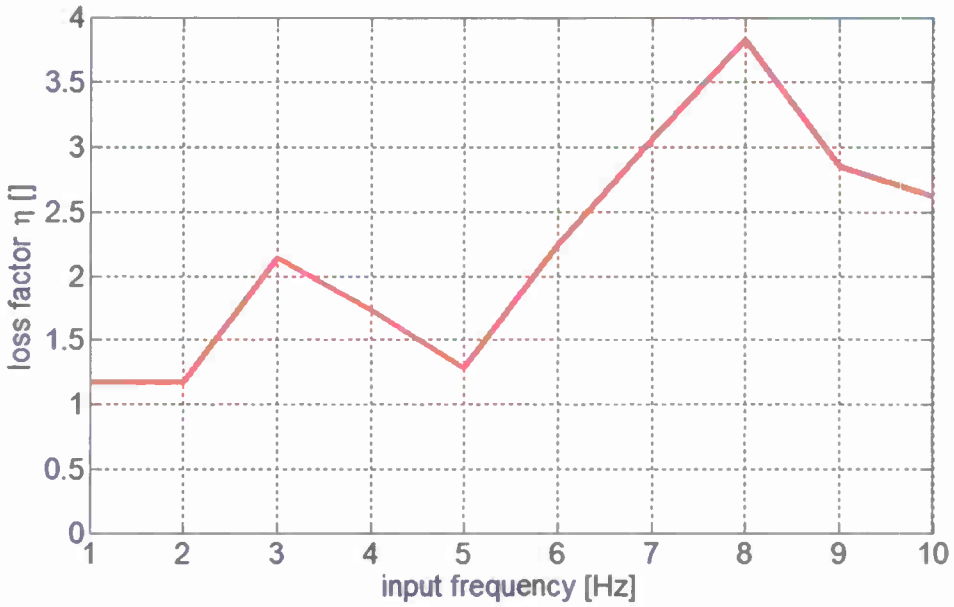

Figure IV-17: Simulation result of System III.
At 10 N, loss factor is greater than 1 from 1 to 10Hz

To further study the performance of the system, we did a parametric study by sweeping through the forcing amplitude (5N to 50N) and input frequency (1Hz to 10Hz). The loss factor performance is shown in Figure IV-18 below. Results show that with this configuration, we can achieve loss factor over 1 from 1 to 10 Hz for all the forcing amplitudes in between 5N to 50N. In addition, the high loss factor performance is very consistent throughout the one order of magnitude range of dynamic loading. This means the designed system is also very robust under harmonic loading. Lastly, we also simulated the impact test with finalized parameters. The main structure is attached to ground with a stiff spring (400000N/m) and an impact force of 4000N with duration 0.01s is applied to the structure. The simulation result is shown in Figure IV-19, where the displacement of structural member is plotted over time. Both cases with snap-through device locked and unlocked are presented for comparison. It can be observed that with all snap-through devices activated, the settling time of the system is significantly reduced to about 2s. This indicates that the designed system is also very effective for shock loading, satisfying another program Task II metric.

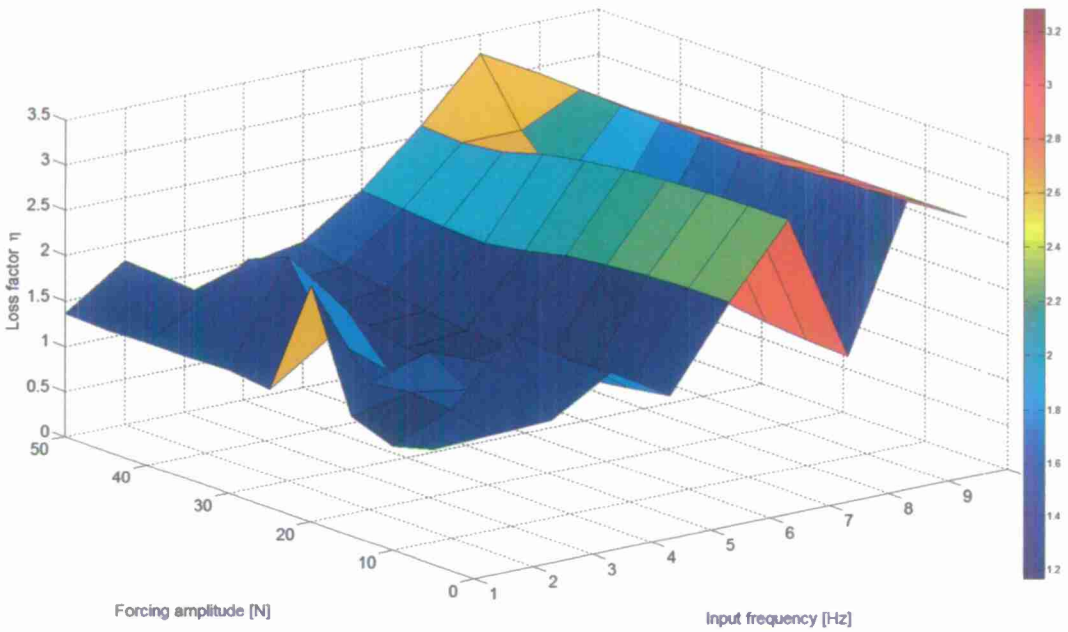

Figure IV-18: Loss factor performance of Configuration II by varying input frequency and forcing amplitude. Study shows that Configuration II can achieve loss factor over 1 throughout the frequency range of interest while maintaining the high performance over one order of magnitude range of dynamics loading.

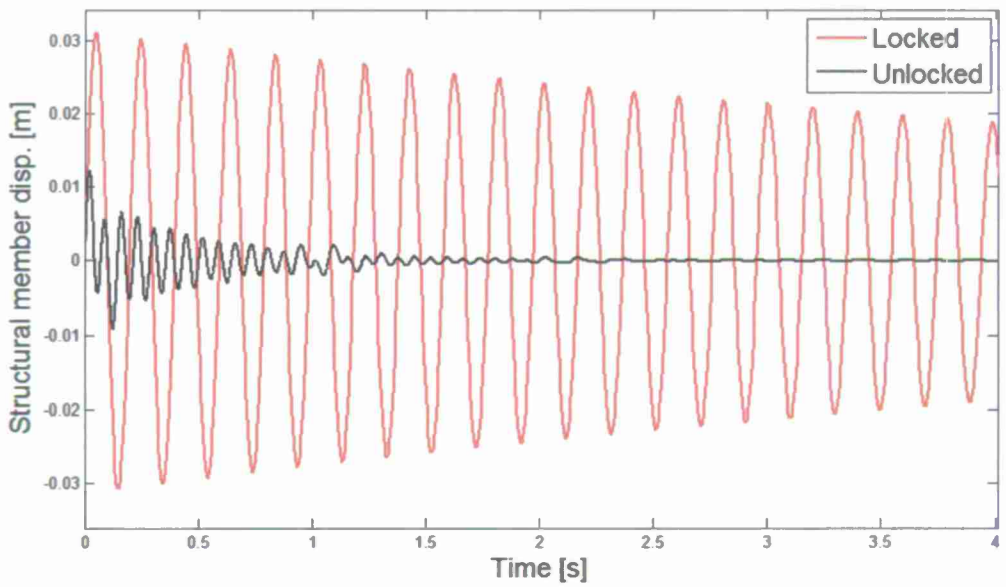

Figure IV-19:Impact response of the designed system. Comparison between the two cases suggests that the subassembly is effective to shock loading.

Rotational Snap-Through Device Experiment

In parallel to the analytical efforts, an experimental investigation is performed to demonstrate the damping performance and passive adaptability of the bistable oscillator. Two variants of bistable oscillators were developed for this experiment validation.

Figure IV-20 illustrates the experimental hardware and corresponding schematic of the rotational bistable oscillator being tested. The test device consists of a snap-through mass that is attached to a frame by an inclined spring on one side and a rigid link on the other, also inclined. As discussed earlier, this kind of geometric arrangement provides two stable equilibrium positions and one unstable equilibrium position of the mass. An off-the-shelf, torsional damper, connected to one of the pivot points, provides approximately viscous damping to the oscillator. The parameters of the test device are summarized in Table Figure IV-2.

Table IV-2: Rotational bistable oscillator's parameter used in experiment

Parameter	Value
Free length of spring, l_0	57.0 [mm]
Distance between pivots, L	110.3 [mm]
Length of rigid link, R	54.0 [mm]
Stiffness of spring, k	14,000 [N/m]
Damping constant, c_t	0.0468 [N-s-m]
Snap-through mass, m	0.2 [kg]

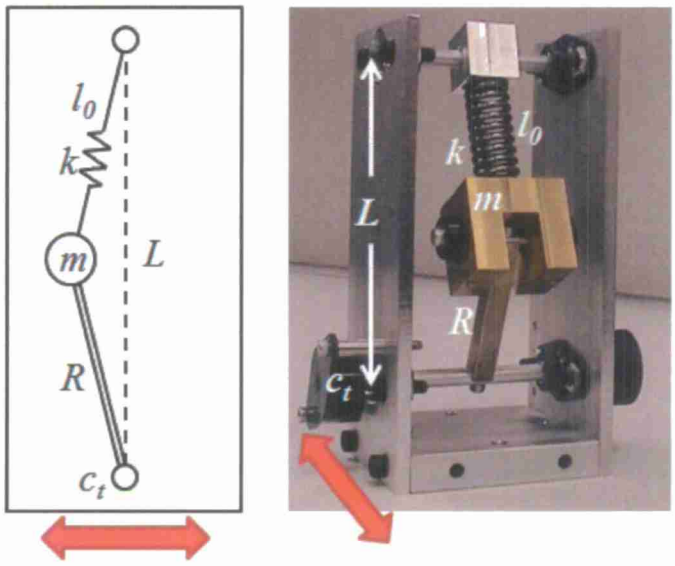

Figure IV-20: Schematic and photo of Rotational bistable oscillator test device. Thick, red, double-headed arrows indicate excitation direction.

Figure IV-21 illustrates the overall test setup. The bistable oseillator is rigidly mounted on top of a shaker table. A potentiometer is used to measure the displacement of the shaker table (the base exeitation amplitude) and the angular displaeement sensor measures the position of the snap-through mass.

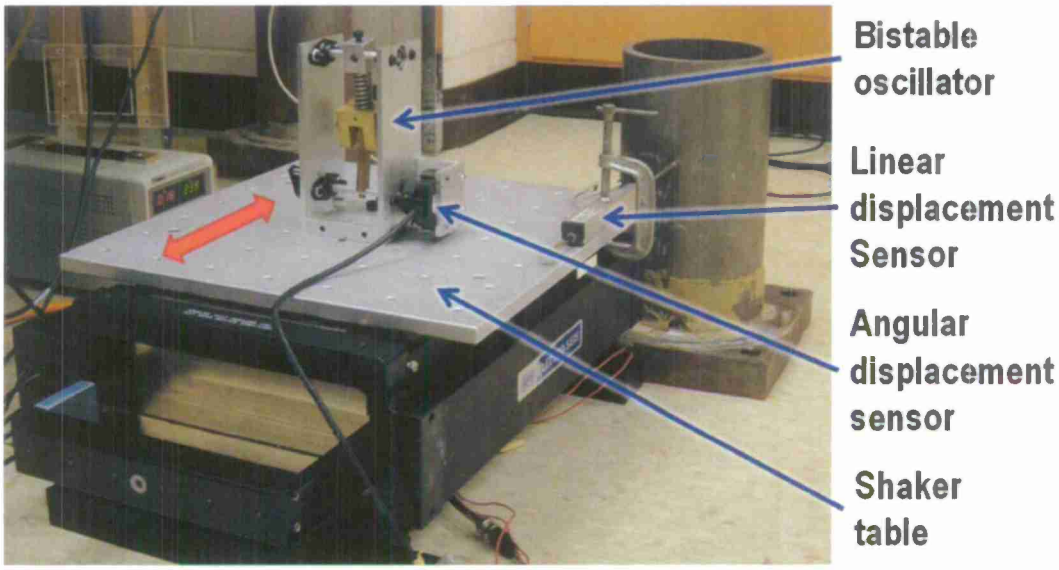

Figure IV-21: Rotational Bistable oscillator experimental setup with key components indicated. Excitation direction is indicated by the thick, red, double-headed arrow.

Figure IV-22 illustrates the time response (a – d) and phase plots (e – h) of the snap-through mass at 11.3 Hz for different input amplitudes. The two red lines in the time response plots and the two red crosses in the phase plots correspond to the two stable equilibrium positions of the

snap-through mass. The vertical axis in the time response plot is the angular displacement of the snap-through mass. The horizontal axis of the phase plot is the angular displacement of snap-through mass and vertical axis is the angular velocity of snap-through mass. As can be seen from the test data, when the input amplitude is low, the snap-through mass only oscillates about one of the stable equilibrium positions. At intermediate input amplitudes, the snap-through mass oscillates in an aperiodic or multiharmonic fashion between the two equilibrium positions. Finally, when the input amplitude reaches certain threshold, the snap-through mass oscillates in a periodic fashion between the two equilibrium positions. Comparing with analysis, the dynamic behavior of the experiment matches well qualitatively with the results of the analysis.

Loss factor is computed for the experiment as described previously. Figure IV-23 shows experimentally determined loss factor plotted for varying input amplitude for a variety of input frequencies. The black dotted line in this plot corresponds to the snap-through threshold amplitude. This is the input amplitude at which the bistable oscillator enters into the periodic snap-through regime. As can be seen in this plot, that loss factor increases significantly as a result of snap-through motion. Additionally, the results show that the loss factor profile is adaptable with input amplitude and frequency.

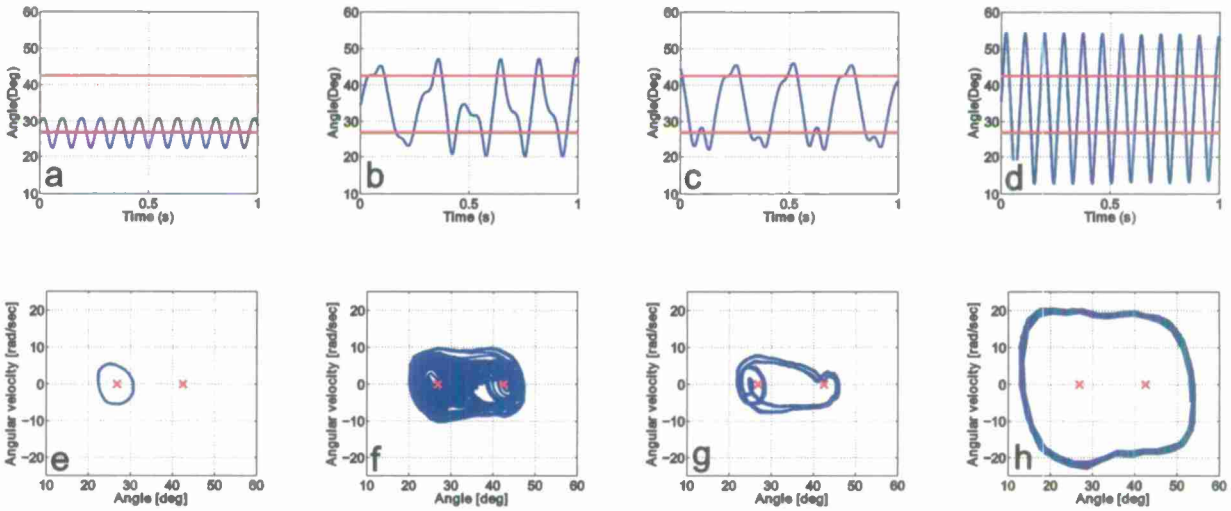

Figure IV-22: Experimentally recorded time response (a – d) and phase diagrams (e – h). The oscillator is excited by an 11.3 Hz load at four levels of base excitation amplitude: 1.58 mm (a, e), 2.89 mm (b, f), 2.92 mm (c, g), and 3.72 mm (d, h).

Overall, it should also be noted that the trend shown in the time response plots (Figure IV-22a-d), the phase plots (Figure IV-22e-h), and the loss factor performance data (Figure IV-23) are very similar to the predictions from the numerical analysis presented previously. In other words, we can conclude that the analytical model and the corresponding results can capture the qualitative behavior of the experimental oscillator quite well.

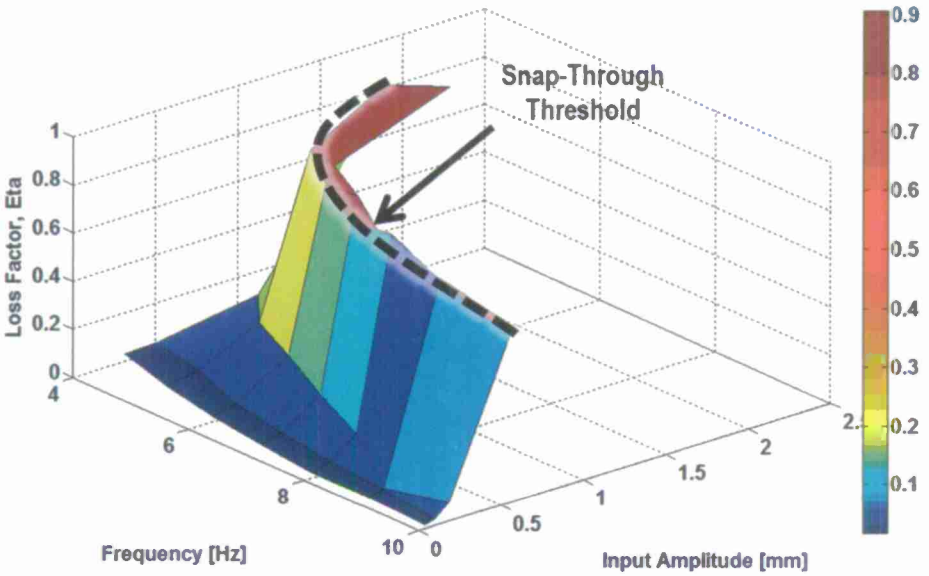

Figure IV-23: Experimentally determined loss factor vs. input amplitude for a variety of input frequencies. The increase in loss factor as a result of snap-through is notable.

Translational Snap-Through Device Experiment

A second variant of the bistable device is a Translational snap-through device. Both the bistable devices as shown in Figure IV-24 share the same operating principles and have same characteristic response. The rationale behind looking into Translational device is that, this variant is simpler to design, easier to fabricate and hence it will be more robust option for the sub-assembly integration.

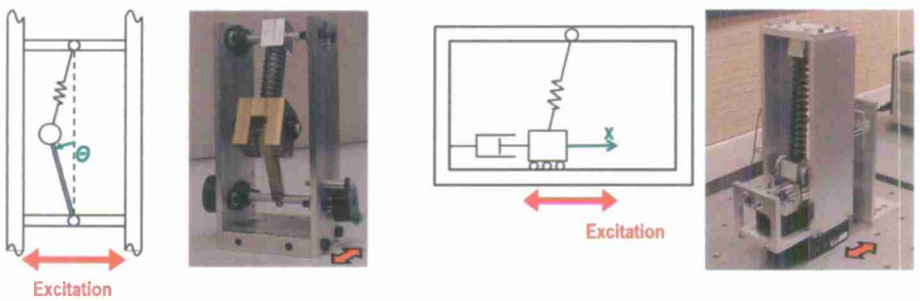

Figure IV-24: Two different variants of bistable oscillators. On the left is rotational device and on the right is Translational device

Figure IV-25 illustrates the experimental hardware and corresponding schematic of the Translational bistable oscillator being tested. The test device consists of a snap-through mass that is attached to a frame by an inclined spring, where the frame is excited in the horizontal direction. This kind of geometric arrangement provides two stable equilibrium positions and one unstable equilibrium position of the mass. Low friction ball bearings are used between the snap-

through mass and the frame. The off the shelf linear dampers used have different damping characteristics in their pull and push modes. Therefore, two dampers are oriented in such a way that, when one damper is in its pull mode, the other one is in its push mode. In this way it is ensured that the damping is symmetrical in both forward and backward directions of excitation. The parameters of the test device are summarized in Table IV-3.

Table IV-3: Translational bistable oscillator's parameters used in experiment

Parameter	Value
Free length of spring	114.4 [mm]
Distance between stable equilibriums	29.3 [mm]
Stiffness of spring	40.0 [KN/m]
Mass of frame	1.04 [Kg]
Snap-through mass	0.27 [Kg]
Natural frequency	7.5 [Hz]

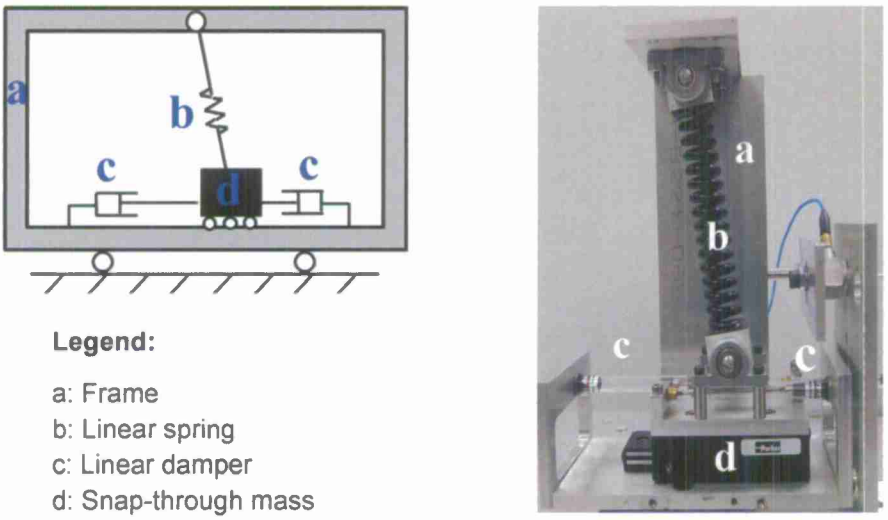

Figure IV-25: Translational bistable oscillator

Figure IV-26 illustrates the overall test setup. The bistable oscillator is mounted on top of a shaker table through a load cell. A potentiometer is used to measure the displacement of the frame and the laser vibrometer measures the displacement and velocity of the snap-through mass.

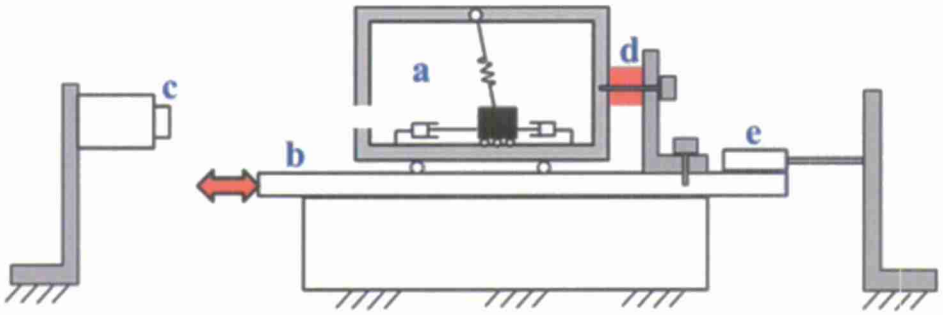

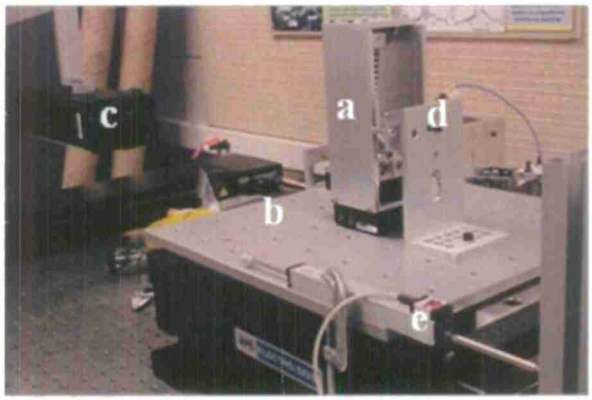

Legend:

a: Bistable oscillator

b: Shaker table

c: Laser Vibrometer

d: Load cell

e: Potentiometer

Figure IV-26: Translational Bistable oscillator experimental setup with key components indicated. Excitation direction is indicated by the thick, red, double-headed arrow.

Figure IV-27 illustrates the time response and phase plot of the snap-through mass at different input amplitudes and Figure IV-28 shows experimentally determined loss factor plotted for varying input amplitude for a variety of input frequencies.

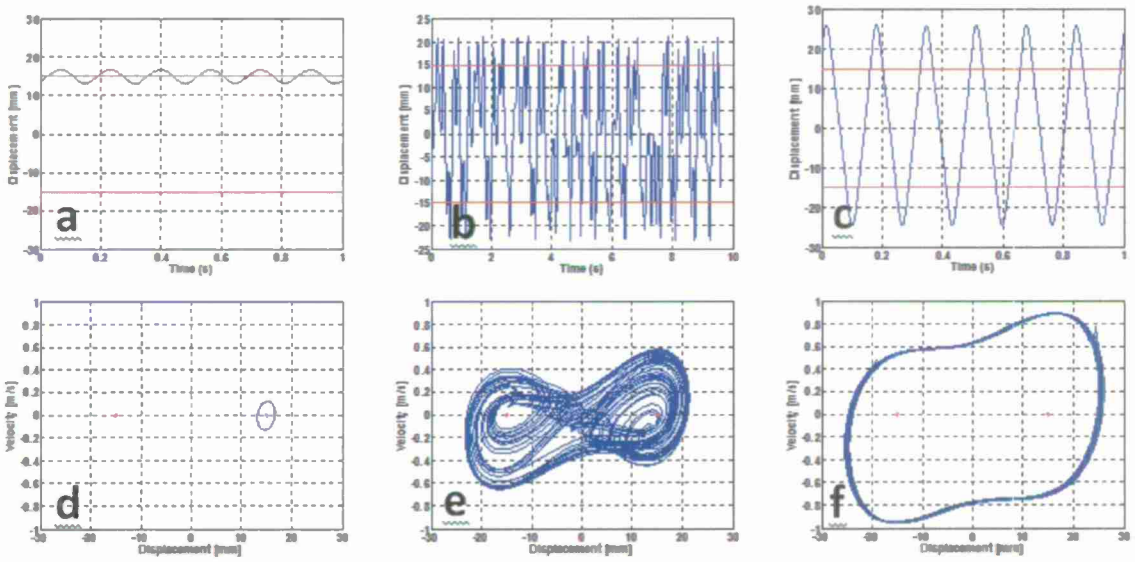

Figure IV-27: Time response (a – c) and phase diagrams (d – f) for the response to base excitation of the bistable oscillator. Experimental data at three levels of base excitation amplitude are shown: 2.08 mm (a, c), 4.22 mm (b, e), 7.10 mm (e, f).

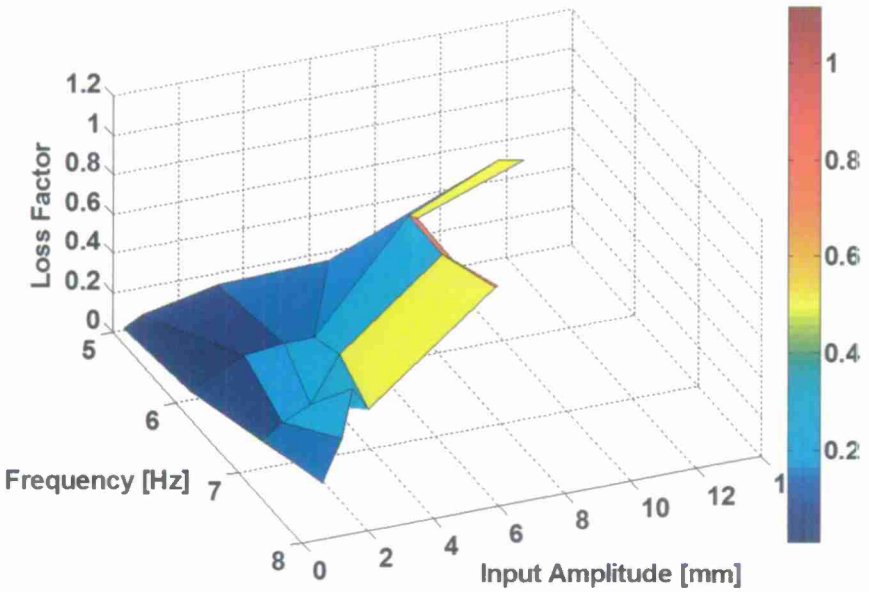

Figure IV-28: Experimentally determined loss factor vs. input amplitude for a variety of input frequencies. The increase in loss factor as a result of snap-through is notable.

Over all, based on the experiment results as shown in Figure IV-27 and Figure IV-28, translational device has same trend as that of rotational device.

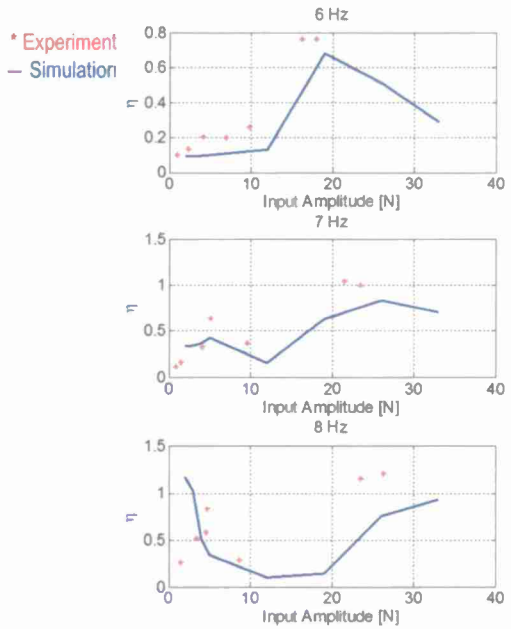

Figure IV-29: Experimentally derived and theoretically predicted loss factor profile of translational bistable oscillator

Having all parameters in hand, numerical analysis is performed and the correlation between the numerical predictions and experimental data is obtained. Figure IV-29 shows the loss factor profile of the oscillator at different excitation frequencies. The red dots correspond to the loss factor derived from test data and the blue solid line corresponds to the loss factor generated through numerical analysis using the analytical model. It can be seen that there is a very good match between the analysis and experimental results and hence this validated model can be used as a tool for sub-assembly synthesis and design.

(IV.2) Development of Synthesis Framework for Sub-Assemblies Structures

Numerical Modeling of the Building Blocks: a Simulink Based Approach

For this thrust, we performed the following tasks:

(a) developed the Simulink models of the main building blocks involved in the periodic rod design

(b) Performed a parametric study to analyze the effect of snap-through devices on the damping performance

(c) Developed the numerical model for the simulation of the composite beam

Numerical model of the periodic rod: unit cell and sub-assembly

The selected modeling technique, based on the Simulink environment, guarantees large flexibility in combining multiple (either identical or different) structural elements while still allowing the use of user-defined analytical models to properly capture the dynamic behavior of the different components (such as the snap-through device). This approach was initially identified as the most suitable modeling strategy to enable the analysis of different sub-assembly and assembly configurations in the subtask 2 and 3.

The first step consisted in developing the Simulink model of the nonlinear appendage embedded in the unit cell of the periodic rod. This model consists in a Single Degree Of Freedom (SDOF) oscillator connected to a nonlinear spring and a linear damper in parallel. The nonlinear spring integrates two components (1) a negative linear terms (providing the negative stiffness), and (2) a positive cubic term providing the nonlinear behavior. This model is consistent with the approach for the modeling and simulation of their building block. A schematic of the SDOF model and of the force-displacement curve produced by the nonlinear spring are depicted in Figure IV-30. A series of simulations were performed to validate the qualitative behavior of the Simulink based model against the numerical (Matlab based) models. The model parameters are listed in Table I. As expected, the model exhibits two stable equilibrium positions at x_0=±1.46e-2 (m).

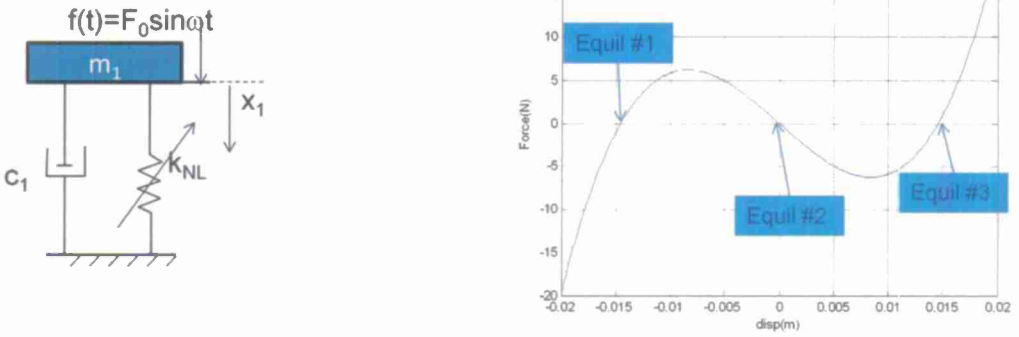

Figure IV-30 Schematic of the single degree of freedom snap-through device and of the force-displacement relationship for the nonlinear spring.

Table IV-4 Model parameters for the single DOF system

parameter	value	note
m_1	1 (kg)	
c_1	10 (N s/m)	
$k_{NL}(x)$	5.241e6 x^3-1112 x	Snap though as depicted in Figure IV-30

Figure IV-31 shows the time response from the SDOF nonlinear model at different input force levels (*2N* and *8N*). The displacement time history indicates that the model is able to correctly capture the amplitude-dependent behavior of the SDOF snap-through device by switching from low amplitude oscillation around one stable equilibrium (x_0=1.46e-2(m)) to high amplitude snap-through oscillation (between $\pm x_0$) as the external forcing function is increased.

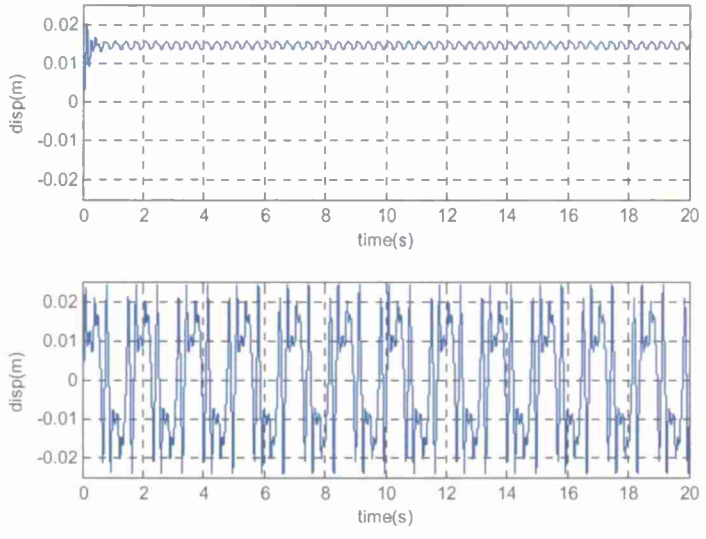

Figure IV-31: SDOF displacement history at different excitation amplitudes (F_0 = 2N (top), 8N (bottom)). ω = 6π rad/s (=3 Hz).

As part of the validation process of the Simulink model we extracted the frequency and amplitude dependent loss factor profile. The loss factor η is calculated according to the following equation:

$$\eta = \frac{E_\tau^d / 2\pi}{\max_\tau (T+U)} = \frac{\frac{1}{n_\tau}\int_\tau [c_1 x(t)][x(t)]dt / 2\pi}{\max_\tau \left(\frac{1}{2} m_1 \dot{x}^2(t) + \int_{x_0}^{x} k_{NL}(x(t))dx\right)} \quad (12)$$

where E^d is the dissipated energy, T is the kinetic energy, U is the potential energy, k_{NL} is the nonlinear spring force. The subscript τ indicates the timeframe during the last multiple cycles after the response reaches a steady state (τ=[T_{max}-ΔT T_{max}], where T_{max} is the final instant of simulation (here chosen at 20s)). ΔT is selected to include multiple quasi-periodic responses. n_τ is the number of excitation period during τ or $n_\tau = \Delta T \times \omega/2\pi$. Equation (1) was used to generate a surface plot showing the variation of the loss factor for different driving conditions. For the chosen paramcters (Table IV-4), the snap though threshold is located around at F_0=6N. The maximum loss factor 0.4408 is observed at (F_0, ω) = (6N, 8π). These results are consistent, from a qualitative standpoint, with the numerical models and experimental results and support the validity of the Simulink-based model.

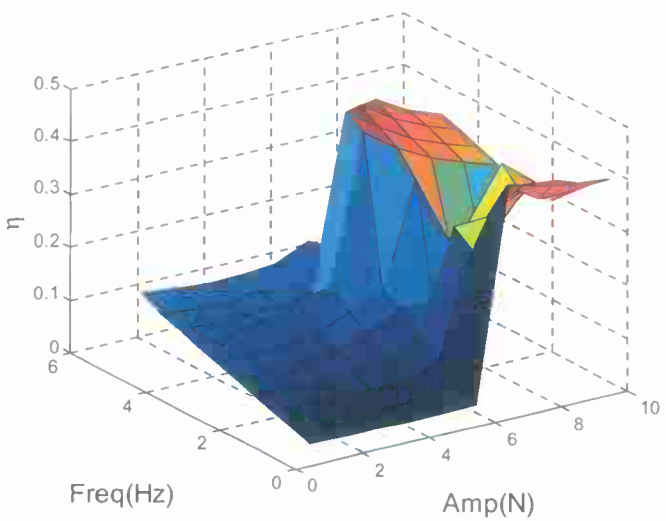

Figure IV-32: Loss factor as a function of the input force amplitude and frequency.

The SDOF model was used as a constitutive building block to simulate the response of the periodic rod with nonlinear absorbers. An example representing a three cell periodic rod subassembly is shown in Figure IV-33. The masses m_1, m_3, m_5, and the stiffness k_{L1}, k_{L3}, k_{L3}, represent the discretized rod structure while the masses m_2, m_4, m_6, represent the nonlinear absorber appendages. The absorbers are connected to the main structure via linear dampers c_1, c_2, c_3, and nonlinear springs k_{NL1}, k_{NL3}, k_{NL3}. The qualitative response of the model (including the characteristic threshold-like behavior inferred by the snap-through elements) is consistent with

the single-DOF models. The simulation shows that the 3-cell assembly provides an equivalent loss factor η=*0.43*.

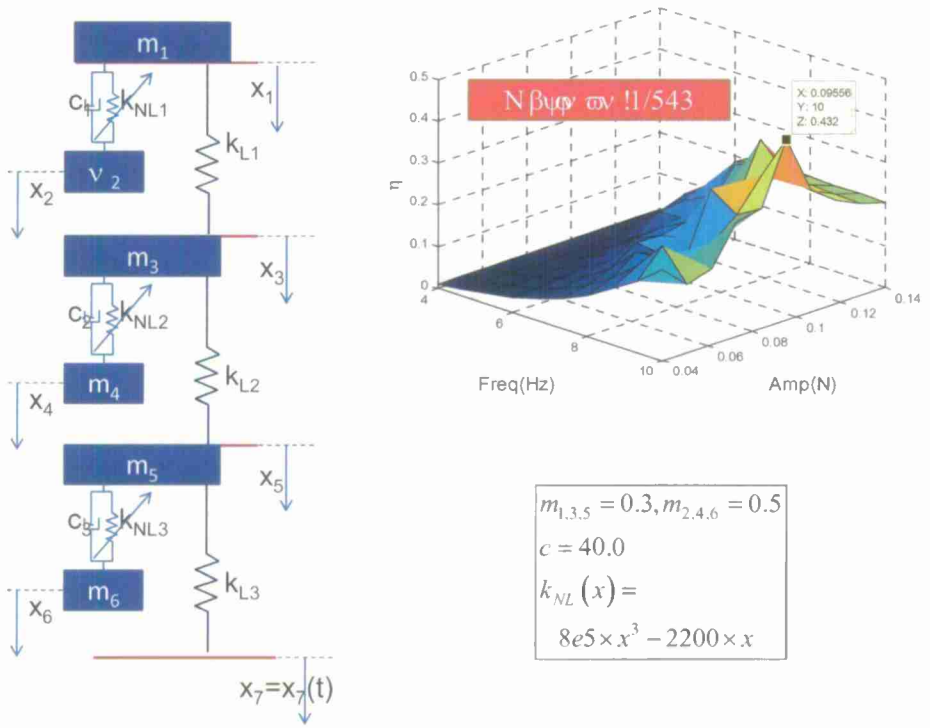

Figure IV-33: Schematic of the MDOF model representing the periodic rod unit substructure and its loss factor.

Building block development in the Simulink environment

As previously mentioned, the loss factor performance of both the constitutive building blocks and the structural assemblies can be tailored by (i) modifying the structural parameters and/or (ii) by properly connecting multiple unit structures (cells). In order to investigate this design space and explore the performance of different mechanical assemblies and networks (i.e. ensembles of different mechanical assemblies), we developed a general (and easily expandable) analysis and design framework able to synthesize optimal structural assemblies. The framework allows exploring a large design space created by different types of building blocks, different types of connections, and types of structural parameters. In order to allow connecting multiple sub-assemblies together we developed two dedicated blocks: (1) the unit substructure and (2) the joint block. The unit substructure includes the entire model of a complex sub-assembly built based on the building blocks available in the library. This unit substructure block is particularly useful when exploring multiple sub-assemblies configurations and structural networks. The joint block represents the equivalent of a mechanical joint and it is defined by a lumped mass and stiffness.

The use of the sub-structure and the joint block is schematically represented in Figure IV-34. Figure IV-34 shows a substructure (blue blocks) connected with two joints (red elements) at each

end. In particular, this example shows an application of the proposed design and modeling approach by using the lumped parameter model of Figure IV-33. Clearly, different type of substructures can be defined. This modeling approach allows treating any sub-assembly, independently of their complexity, as a black-box with input and output ports. The ports provide an easy way to connect multiple black boxes (each one including identical or different sub-assemblies) together by exploiting different configurations. The substructure block has two input ports for the force at the interface and two output ports for the displacement. The joint block has two input ports for displacement and one output port for force. In order to estimate the equivalent loss factor when using this "sub-structuring approach" the energy terms in Eq. **Error! Reference source not found.** are calculated component-wise and summed up at system level. Note that in Figure IV-34 Ed = E^d (dissipated energy), E_k=T (kinetic energy), E_s=U (Potential energy).

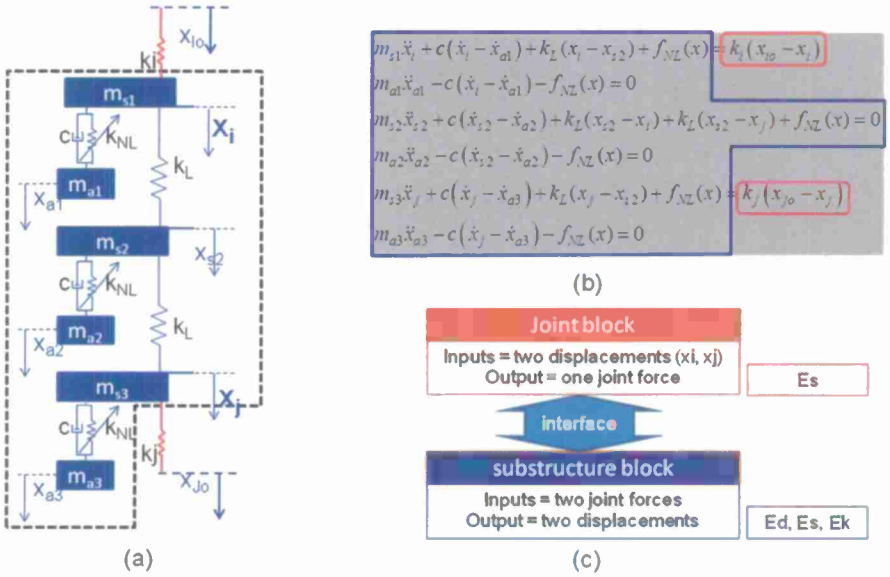

Figure IV-34: Substructure and joint blocks; (a) schematic view of the sub-structure block connected to two joint blocks, (b) system equations, (c) interfacing parameters between joint and substructure.

To enable the network design using the substructure and joint block, an additional block element was defined: the "level" block. The level block is used to connect multiple substructures in parallel. An example of an assembly with three sub-structures connected over three levels is shown in Figure IV-35. This feature is particularly useful when using the design framework for network synthesis, where multiple sub-assemblies are connected together according to different series and parallel configurations.

Figure IV-36 shows the corresponding Simulink models of the different blocks. These constitutive building block models are available in the design framework and can be selected independently by the algorithm to form optimal network having assigned performance. For each block the input and output parameters are indicated using light yellow and purple color, respectively. The number of input ports in the level block can be adjusted as needed depending

on how many substructures are connected to the same level (Figure IV-36 shows an example using four input ports).

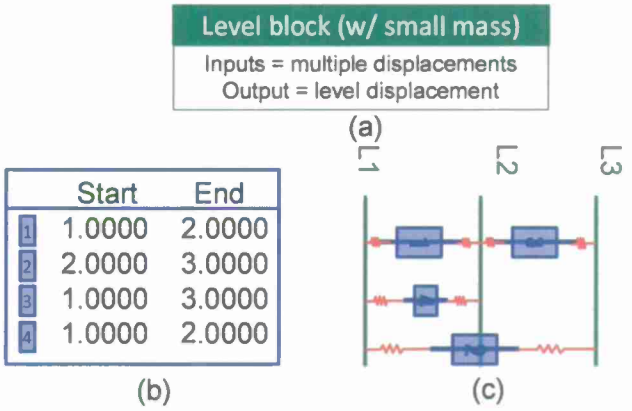

Figure IV-35: (a) Input and output ports of the level block used to share DOF between substructures (b) example of network connectivity (c) corresponding physical network.

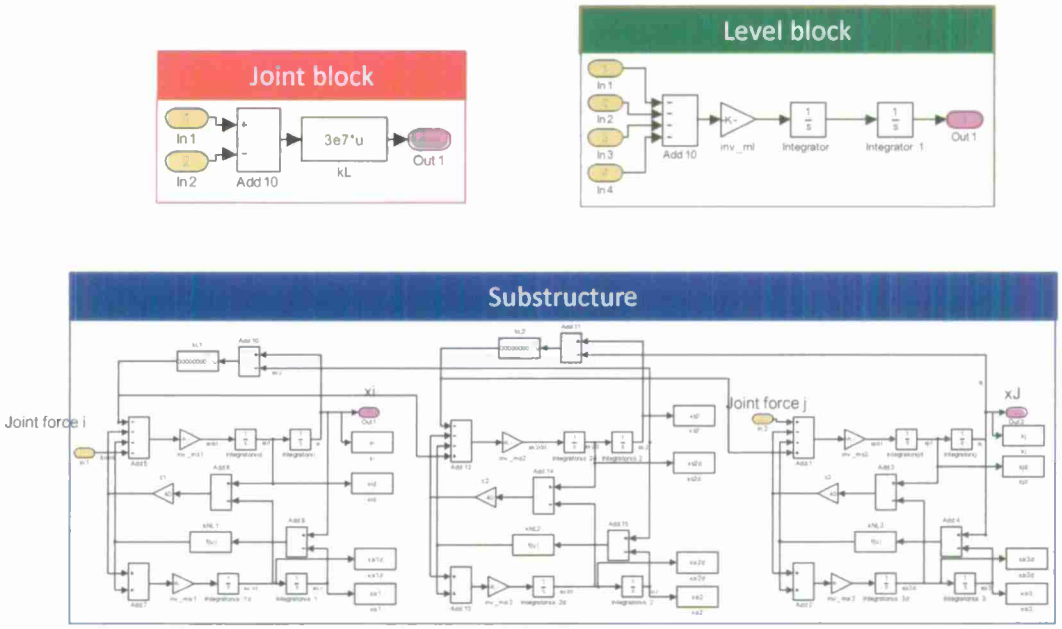

Figure IV-36: Simulink models for each one of the block used for the substructuring modeling approach used for the subassembly and network design.

Model development of composite beam with planar snap-through units

In order to perform the optimal design of the planar composite-beam sub-assembly, we developed a Finite Element model that was not integrated in the design framework. The model was developed in Matlab and it can be integrated into the Simulink based optimization framework for future applications. The model simulates the bending vibration of the metal beam (as shown in Figure IV-37) with attached SDOF snap-through resonators.

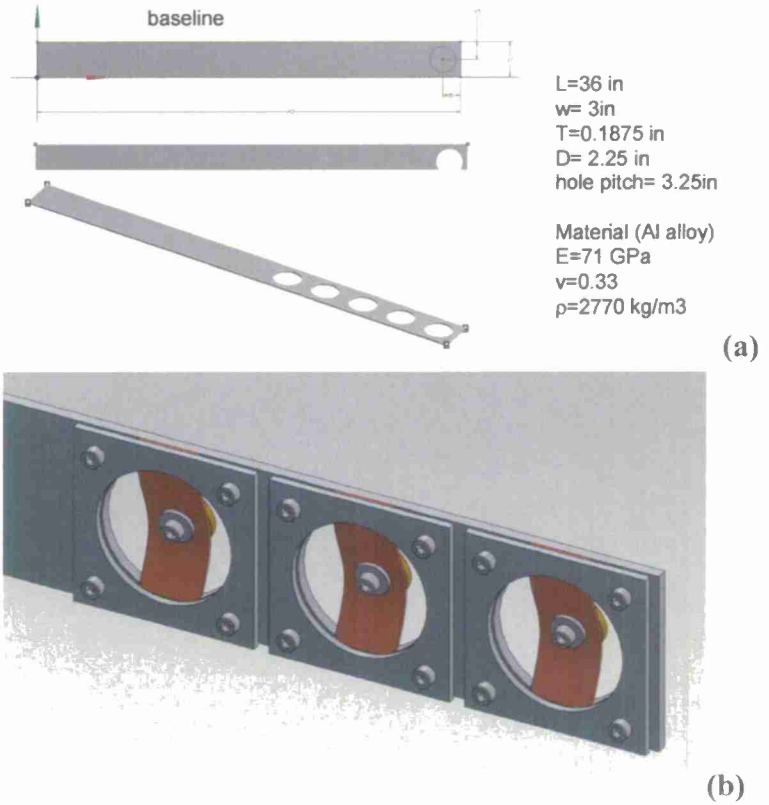

Figure IV-37: Planar snap-through assembly - beam model and its properties. (a) schematic of the composite beam including geometric and material properties. (b) snap-through device attachment

The FEM model is constructed using beam elements having 2 DOF (transverse displacement (w) and rotational angle (θ)) at each node and linear shape functions. The snap-through appendages are modeled as lumped mass connected to the beam via a nonlinear spring (using the same formulation introduced in the previous section) and a linear damper. The schematic of the FEM model is shown in the following figure.

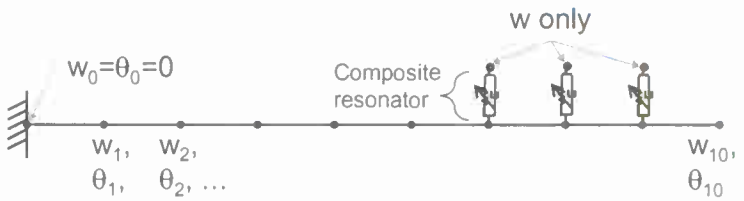

Figure IV-38: The FEM model for beam with embedded planar snap-through devices.

For verification purposes, the resonant frequency and mode shapes produced by the beam model without resonators were compared with commercial FE model. Figure IV-39 shows the first two mode shapes.

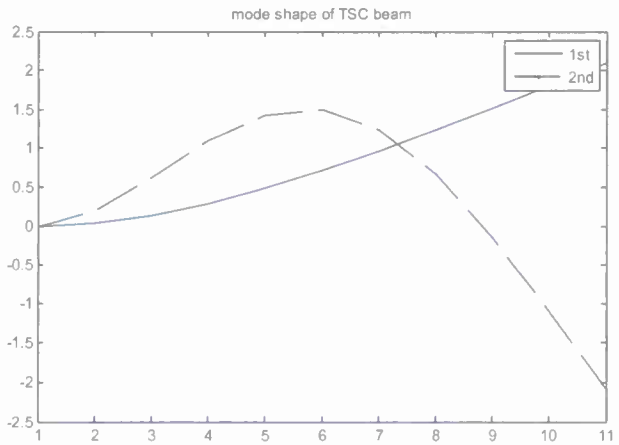

Figure IV-39: First two mode shapes of the composite beam (without resonators) by FEM

The FEM formulation of the cantilever beam is described by the following equation:

$$\left[-\omega^2 \mathbf{M}^G_{2n\times 2n} + j\omega \mathbf{C}^G_{2n\times 2n} + \mathbf{K}^G_{2n\times 2n}\right]\mathbf{X}^G_{2n\times 1} = 0, \qquad (13)$$

where $\mathbf{X}^G = e^{j\omega t}\times[w_0\ \theta_0\ w_1\ \theta_1\ \ldots\ w_n\ \theta_n]^T$ and n=11 (total number of nodes), and $\mathbf{M}^G$, $\mathbf{C}^G$, $\mathbf{K}^G$ are the global mass, damping, and stiffness matrices (dimension $2n\times 2n$), respectively. When the rotational DOF is fixed (θ_0) at node 0, we can sweep out the second row and the second column corresponding to θ_0 DOF from $\mathbf{M}^G$, $\mathbf{C}^G$, and $\mathbf{K}^G$ matrices to reduce their dimension (**M**, **C**, **K**, $(2n\text{-}1)\times(2n\text{-}1)$ matrices) and have a new $\mathbf{X}= e^{j\omega t}\times[w_0\ w_1\ \theta_1\ \ldots\ w_n\ \theta_n]^T$. If the transverse harmonic velocity ($w_0=A_0\omega\, e^{j\omega t}$) is given at node 0, Eq. (13) is rewritten as:

$$-\omega^2\mathbf{M}\begin{bmatrix} w_0 \\ w_1 \\ \theta_1 \\ \cdots \\ \theta_n \end{bmatrix} + j\omega\begin{bmatrix} c_{11} & c_{13} & c_{14} & \cdots & c_{1(2n)} \\ c_{31} & & & & \\ c_{41} & & \ddots & & \\ \cdots & & & & \\ c_{(2n)1} & & & & c_{(2n)(2n)} \end{bmatrix}\begin{bmatrix} A_0 \\ w_1 \\ \theta_1 \\ \cdots \\ \theta_n \end{bmatrix} + \mathbf{K}\begin{bmatrix} w_0 \\ w_1 \\ \theta_1 \\ \cdots \\ \theta_n \end{bmatrix} = 0,$$

$$-\omega^2\mathbf{M}\mathbf{X} + j\omega\begin{bmatrix} 0 & c_{13} & c_{14} & \cdots & c_{1(2n)} \\ 0 & & & & \\ 0 & & \ddots & & \\ \cdots & & & & \\ 0 & & & & c_{(2n)(2n)} \end{bmatrix}\mathbf{X} + \mathbf{K}\mathbf{X} = -j\omega A_0\begin{bmatrix} c_{11} \\ c_{31} \\ c_{31} \\ \cdots \\ c_{(2n-1)1} \end{bmatrix}, \qquad (14)$$

$$\therefore -\omega^2\mathbf{M}\mathbf{X} + j\omega\mathbf{C}_\mathbf{R}\mathbf{X} + \mathbf{K}\mathbf{X} = -j\omega A_0\mathbf{C}_\mathbf{L}.$$

Note that $\mathbf{C_L}$ is the first column of $\mathbf{C}$, and $\mathbf{C_R}$ is $\mathbf{C}$ with its first column zero. The gain (acceleration/velocity)^2 is obtained as

$$\left|\frac{\mathbf{X}}{\omega A_0}\right| = \left|\left[-\omega^2\mathbf{M} + j\omega\mathbf{C}_\mathbf{R} + \mathbf{K}\right]^{-1}\left(-j\mathbf{C}_\mathbf{L}\right)\right|,$$

$$\therefore \left|\frac{\omega^2\mathbf{X}}{\omega A_0}\right|^2 = \omega^4\left|\left[-\omega^2\mathbf{M} + j\omega\mathbf{C}_\mathbf{R} + \mathbf{K}\right]^{-1}\left(-j\mathbf{C}_\mathbf{L}\right)\right|^2 \qquad (15)$$

The nonlinear appendages were modeled in a similar fashion to the nonlinear absorbers used in the periodic rod model that is using a lumped mass connected via a nonlinear spring and a linear damper. In order to tune the dynamic response of the nonlinear resonators, the composite beam FE model was integrated with the GA based optimization approach to perform parameter tuning.

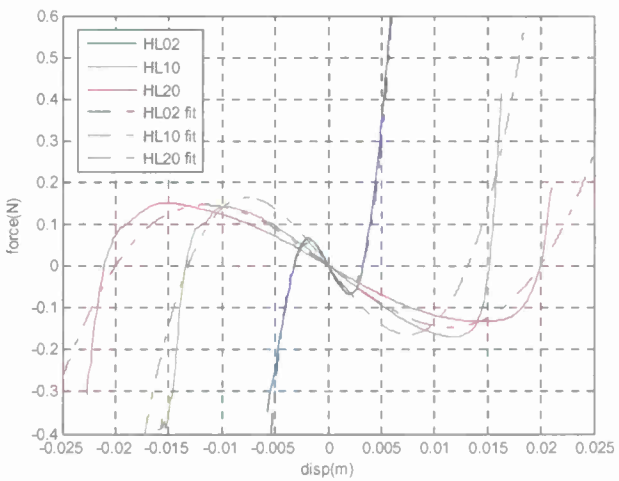

Figure IV-40: Force-displacement relations for the snap-through devices made of different viscoelastic material. The equivalent spring parameters were extracted by curve fitting.

Three kinds of snap-through attachments (HL02, HL10, HL20) were considered according to the available shallow-arch snap-through devices. Each one of these attachments corresponded to a different viscoelastic material. The spring data to be used in the FEM model were obtained by interpolation of the experimental force-displacement curves, as shown in Figure IV-40. The viscous damping constants are based on material tests conducted by on the viscoelastic material used to fabricate the snap-through elements.

Simulations were performed to test the dynamic response of the beam model with attached snap-through elements. Figure IV-41 shows the time response in terms of relative transverse displacement of the attached resonators. The input is a sinusoidal force at 5Hz with amplitude increasing from 50 to 400 N. As expected, the qualitative response of the system is similar to that of the periodic rod sub-assembly with nonlinear resonators. As the amplitude of the driving force is increased, the transition from non-snapping to aperiodic and, finally, to periodic snapping behavior is clearly visible.

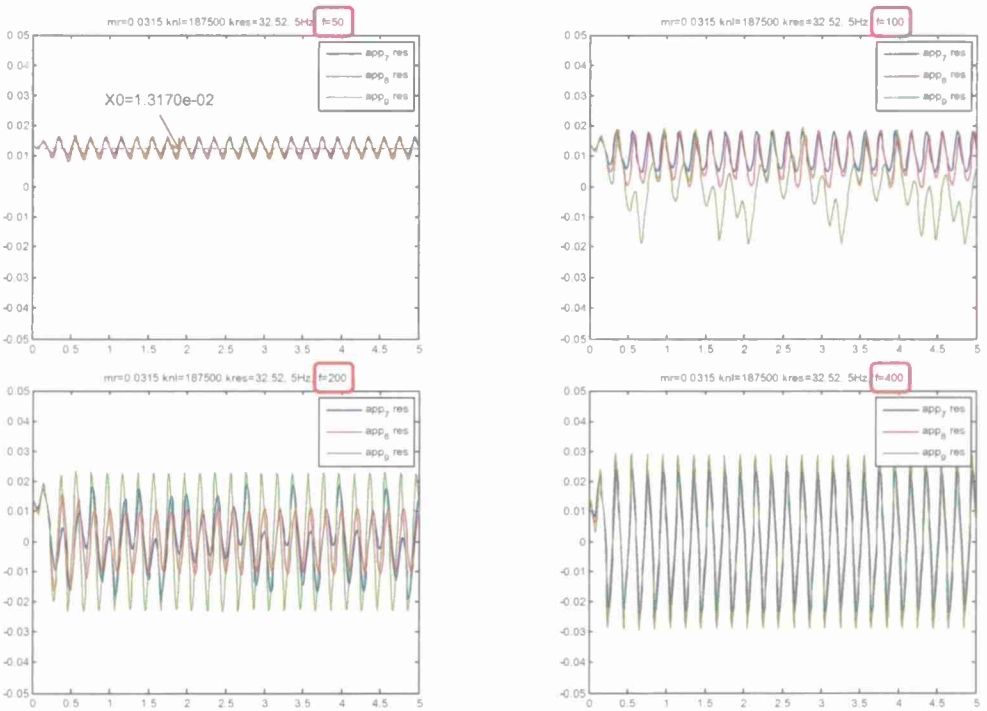

Figure IV-41: Dynamic response of the snap-through appendages for increasing input force.

We have developed the main modeling procedure and the corresponding numerical models to simulate the two sub-assembly mechanical systems. Despite this simulation technique was applied to two specific structural assemblies, the modeling approach based on constitutive blocks and sub-structures allows for a very flexible design framework that can potentially be extended to integrate several types of constitutive building blocks. This modeling approach represents the foundation of the design and optimization strategy.

Optimization of the System Performance using Genetic Algorithms (GA)

In this thrust, we (i) integrated the modeling approach with a Genetic Algorithm based optimization teehnique and (ii) we performed optimization analysis to identify possible optimal configurations for the design of the final prototypes.

Detailed objeetives inelude:

- Implementation of the optimization process by selecting appropriate optimization strategies (ineluding single-objeetive and multi-objective techniques).
- Parametric study to investigate the effect of different design parameters (joints/substructures/connections) on the overall performance.
- Conducting optimization analysis to select possiblc candidates for the fabrication of the final prototypes.

Optimization Strategy

The Simulink based modeling approach, was integrated with a Genetic Algorithm technique in order to develop an integrated environment able to synthesize optimal sub-assemblies exhibiting either optimal or user-assigned performance. In particular, we have investigated the following two scenarios:

- Synthesizing optimal configurations for the fabrication of (i) the periodic rod sub-assembly prototype and (ii) the composite beam prototype. The optimal configuration was intended to minimize the inertial mass of the attaehed nonlinear absorbers while still satisfying the required damping and stiffness performance according to the program metrics.
- Devcloping an optimization based procedure for the synthesis of either sub-assemblies or structural networks able to deliver user-defined performance.

A schematic of the overall optimization strategy for the synthesis of structural sub-assemblies and network is shown in Figure IV-42.

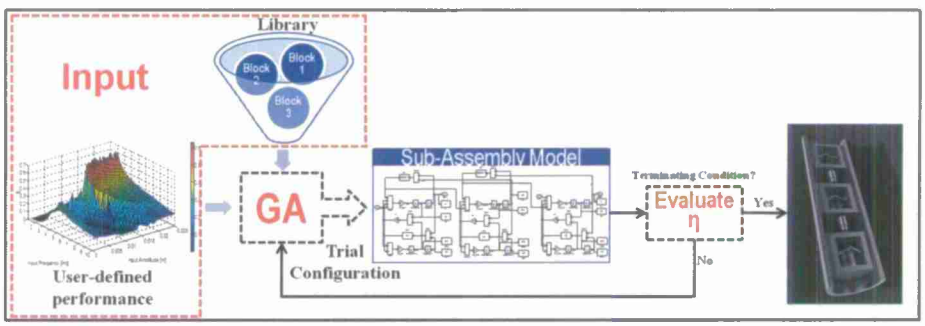

Figure IV-42: Schematic of the overall optimization approach for the synthesis of sub-assemblies and structural networks.

Two optimization strategies were investigated:

- **Single-objective optimization**: this approach was intended for the synthesis of structural configurations where no specific loss factor profiles or passively adaptive performance are required. This type of approach is suitable to obtain minimum mass design while fulfilling the minimum damping and stiffness requirements. In this case, the problem is set up as a mass minimization problem where the damping requirement is imposed as a constraint.

- **Multi-Objective optimization**: pareto-optimality concepts are used to identify optimal structural configurations (either sub-assemblies or networks) where the loss factor profile is provided as an input parameter. That is, we seek possible structural configurations (synthesized based on the available building block library) able to provide user-defined loss factor performance.

Design synthesis of the periodic rod subassembly

The single-objective optimization study was used to identify an optimal configuration for the fabrication of the periodic rod prototype (3-cell structure). The optimal configuration is intended to minimize the inertial mass of the attached nonlinear absorbers while still meeting the required damping and stiffness performance.

To identify the final optimal design, we define the structural parameters (i.e. coefficients of the snap-through springs, damping, and lumped masses) as design variables. The model for this analysis is shown in Figure IV-43. The details of the design variables are listed in Table IV-5. At each cell, six design variables are assigned (eighteen design variables in total). The design problem is formulated in order to minimize the objective function which is the inertial mass of the appendages. The loss factors at three excitation frequencies (4Hz, 6Hz, and 9Hz) are constrained to be larger than $\eta=1$, in order to satisfy program metrics. In this design, it is assumed that each mass is mostly effective at a specific frequency, so each cell is design to have a preferential linearized resonant frequency. Also the inertial masses m_r and m_s are constrained to be larger than 0.3Kg and 0.5kg to facilitate the fabrication of the experimental setup by using off-the-shelf components. The stiffness coefficient of the spring k_r is determined by imposing that the resonance frequency of the appendage satisfies the frequency requirements as the mass of the appendage is varied. An approximate relation for the linearized resonant frequency ($k_r = (m_r\ m_s)*\omega^2$) is used for this purpose. The excitation amplitude is fixed as 0.25mm. The optimization formulation is shown in Figure IV-44 which also displays a 3-unit-cell rod sub-assembly used in this design study.

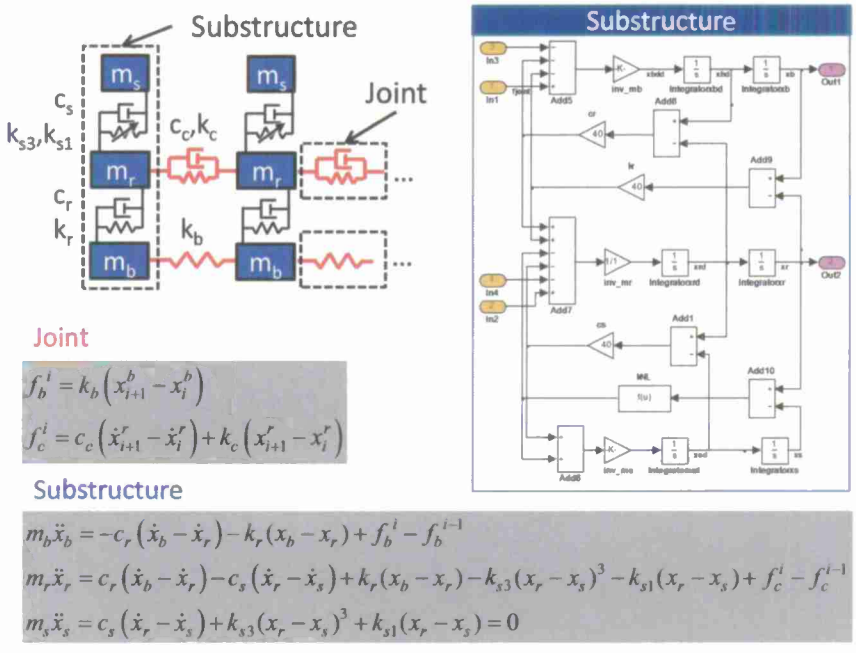

Figure IV-43: Schematic of the periodic rod subassembly and the corresponding Simulink substructure block. The force equilibrium equations for the joint and substructure are also shown.

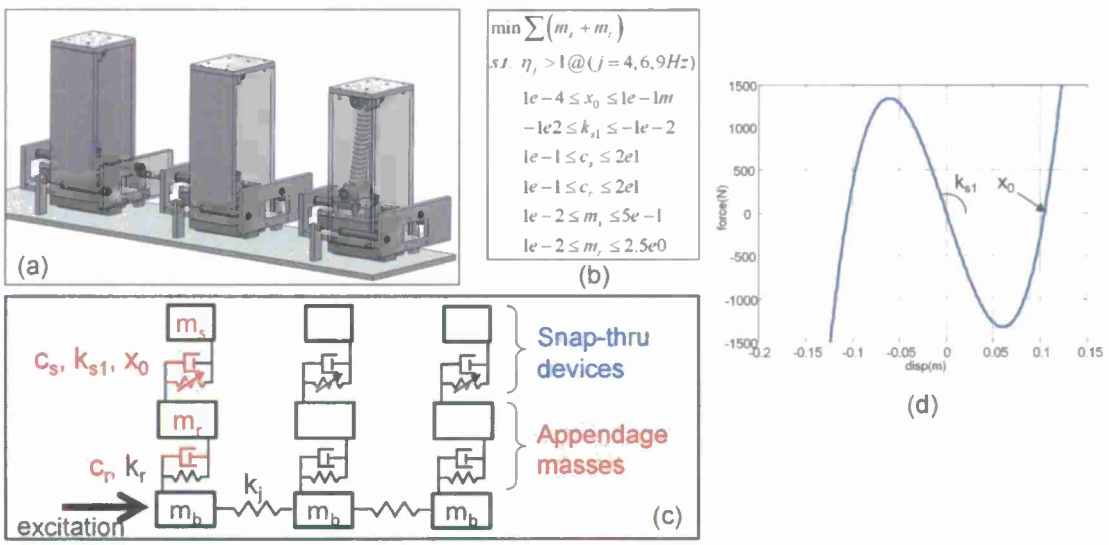

Figure IV-44: Schematic description of the modeling approach for the synthesis of the final prototype of the periodic rod sub-assembly using single-objective optimization. (a) 3 unit cell rod sub-assembly, (b) design formulation (c) schematic of the lumped model for 3-cell periodic rod sub-assembly(d) k_{s1} and x_0 in snap-through element.

Table IV-5: Design parameters

symbol	description	symbol	description
x_0	Equilibrium position*	c_r	appendage damping coefficient
k_{s1}	Linear stiffness*	m_s	Snap-thru mass
c_s	Snap-thru damping coefficient	m_r	Appendage mass

*Parameters for snap-thru spring (see Figure 1(d))

Using the single-objective optimization approach as described above, we identified an optimal configuration yielding a significant mass reduction of about 45% while satisfying all the constraints – the loss factors at the three selected excitation frequencies are 1.09, 1.07, and 1.02, respectively. These results provide one possible design for the 3-cell periodic rod sub-assembly that represents one of the two final prototypes used as proof of concept of the periodic rod design.

Note that without constraining the minimum mass value of the appendages (in order to meet the requirements to use specific off-the-shelf components) we can achieve an optimized configuration delivering a 63% mass reduction with respect to the initial configuration. Also, the loss factor satisfies the design requirement as shown in Figure IV-45.

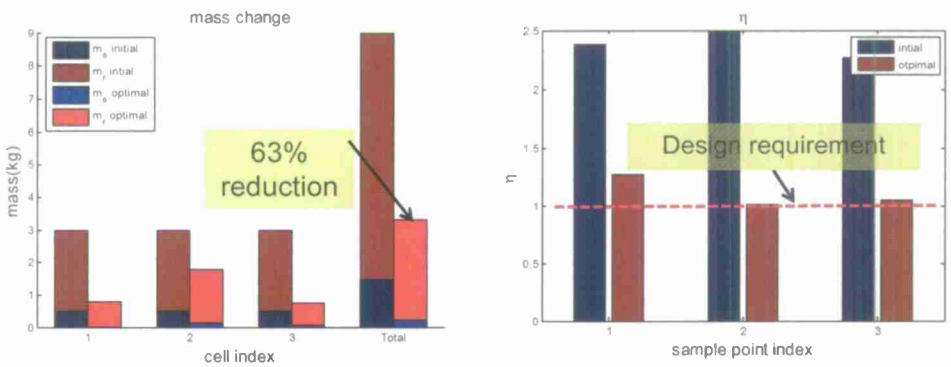

Figure IV-45: Optimization results for the 3-cell model. (a) mass reduction, (b) loss factor constraints.

A similar modeling and analysis approach was used to synthesize the final design of the 10-cell periodic assembly. The design problem is formulated to find the optimal combination of the design factors to minimize the inertial masses (both snap-through and appendages). The optimization formulation is shown in Eq. (16). The loss factors at the selected excitation frequencies (1 to 10 Hz) are constrained in the optimization formulation in order to yield final performance consistent with the program metrics. The excitation amplitude is fixed as 1mm.

$$\begin{aligned}
&\min \sum\left(m_s + m_r\right) \\
&s.t.\ \eta_j > 1 @ (j = 1,...,10Hz), 1mm\,excitation \\
&\quad x_0 = [0.001, 0.003, ..., 0.015](m) - 8\,candidates \\
&\quad k_{s1} = [-40, -39, -38, ... -5](N/m) - 36\,candidates \\
&\quad c_s = [1.5, 2.0, 2.5, 3.0, 3.5](Ns/m) - 5\,candidates \\
&\quad c_r = [1.5, 2.0, 2.5, 3.0, 3.5](Ns/m) - 5\,candidates \\
&\quad m_s = [0.3, 0.31, 0.32, ..., 0.5](kg) - 21\,candidates \\
&\quad m_r = [0.8, 0.85, 0.90, ...2.500](kg) - 35\,candidates
\end{aligned} \tag{16}$$

Through this optimization study we identified an optimal configuration yielding a mass reduction from 30 kg to 19.32 kg while satisfying the program metric – the loss factors at each excitation frequency are larger than 1.0. Table IV-6 shows in detail the resulting optimal design.

Table IV-6: Optimal configuration for the 10-cell model w/ discrete variables

	X0 (m)	Ks1(N/m)	Cs(N/ m/s)	Cr(N/ m/s)	Ms (kg)	Mr (kg)	**η**
Cell1	0.009	-7	3.5	1.5	0.33	2.5	**1.046**
Cell2	0.005	-30	1.5	3	0.35	2.2	**1.465**
Cell3	0.009	-38	2.5	3.5	0.37	2.2	**1.117**
Cell4	0.013	-16	3.5	1.5	0.46	1.5	**1.125**
Cell5	0.009	-9	1.5	2	0.39	1.15	**1.163**
Cell6	0.015	-21	2	3.5	0.46	1.3	**1.157**
Cell7	0.015	-32	2.5	3.5	0.35	1.8	**2.062**
Cell8	0.007	-26	1.5	2	0.34	0.9	**1.178**
Cell9	0.005	-5	3	2	0.44	0.95	**1.044**
Cell10	0.015	-23	2	3	0.38	0.95	**1.031**
Active at Lower bound (red) and Upper bound (blue)							

An additional design study was performed in which we considered a safety factor (α=0.2) applied on the design loss factor as shown in the following equation:

$$\begin{aligned}
&\min \sum\left(m_s + m_r\right) \\
&s.t.\ \eta_j > 1 + \boldsymbol{\alpha}\ at\ j = 1, 2, ..., 10Hz, (1mm\,excitation)
\end{aligned} \tag{17}$$

The safety factor was intended to account for inaccuracies in the modeling parameters and in the fabrication process so to guarantee that the performance of the final prototype meets the required metric.

Through this optimization study we found more conservative designs compared to the design shown in Table IV-6. In this design, in fact, the mass was reduced from an initial value of 30kg to 20.52 kg while all the loss factors were found to be larger than 1.20. Table IV-7 shows the

design optimization results. The design results were used to support the fabrication of the final prototype.

The mass reduction and the loss factors are displayed in Figure IV-46 for the optimized results on the 10-cell structure.

Table IV-7: Design result for 10-cell model w/ discrete variables and α=0.2

	X0 (m)	Ks1(N/m)	Cs(N/ m/s)	Cr(N/ m/s)	Ms (kg)	Mr (kg)	**η**
Cell1	0.003	-33	2.5	1.5	0.3	2.5	**1.464**
Cell2	0.005	-12	2	2.5	0.45	2.25	**1.592**
Cell3	0.009	-21	3	2	0.42	1.8	**1.282**
Cell4	0.007	-11	2	2.5	0.31	1.9	**1.788**
Cell5	0.013	-16	2	3	0.39	1.4	**1.234**
Cell6	0.005	-34	3	3.5	0.32	1.7	**1.391**
Cell7	0.009	-34	2	2.5	0.46	1.1	**1.253**
Cell8	0.009	-15	2.5	2.5	0.37	1.45	**1.890**
Cell9	0.009	-29	2.5	2.5	0.37	1.4	**1.885**
Cell10	0.009	-8	3	3	0.48	1.15	**1.238**
Active at Lower bound (red) and Upper bound (blue)							

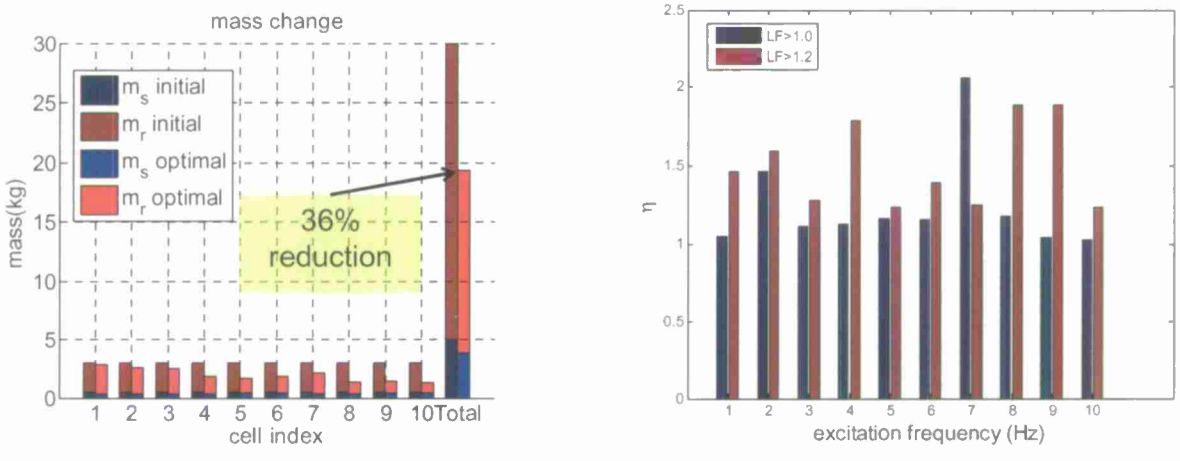

Figure IV-46: Optimization results for 10-cell model (a) mass reduction for η(loss factor)>1.0 case, (b) loss factors for the optimized design (η>1.0 and η>1.2 cases).

Multi-objective design optimization for the synthesis of passive adaptive structural assemblies

As previously mentioned, the second optimization approach we have investigated was based on multi-objective techniques. In particular, we used pareto-optimality concepts to identify optimal structural configurations (either sub-assemblies or networks) exhibiting predefined loss factor profiles. That is, we searched the design space for possible structural configurations (synthesized based on the available building blocks in the library) able to provide user-defined

loss factor performance. By pursuing this design approach we developed an optimization strategy able to synthesize structures having passive adaptive performance specified by the end-user.

In order to illustrate the proposed design technique, we selected a case study as shown in Figure IV-47. The numerical model used to test the design procedure consists in the 3-cell periodic rod subassembly shown in Figure IV-44. In the multi-objective design approach, we assign a loss factor profile as input and synthesize a possible structure (based on the available building blocks) able to provide the best fit to the required input.

In the example of IV-47, we assume a pre-determined loss factor profile that describes the performance required to the final structural assembly ("sampling points and target values" in the figure). An assigned loss factor profile is discretized in a finite number of sampling points (only four in this example). These discrete design points, describing the performance of the subassembly at prescribed frequencies and amplitudes, are then translated into objective functions and imposed via a multi-objective optimization approach. At this stage, the optimization problem is posed in the form of a constrained surface fitting problem, or

$$\min\left\{\eta_i - \eta_i^T\right\}^2 \; at \; s_i(sample \;\; points) \tag{18}$$

where η_i is the target loss factor value at the sampling point s_i. The optimization problem is solved in terms of a pareto-optimal approach. The pareto-optimal approach provides as final result a set of feasible solutions that best fit the assigned target points. The error sum square of the fitness functions is then used to compare the different solutions at the pareto-frontier and to extract the candidate solution(s). In the example provided in Figure IV-47, solutions #6 and #7 provide the best fit of the loss factor surface as indicated by the error sum square of the fitness functions. The resulting loss factor surface plot corresponding to the pareto-solutions are obtained by re-running the dynamic response of the optimized structure. Both these results show a very good approximation to the original loss factor profile provided as input.

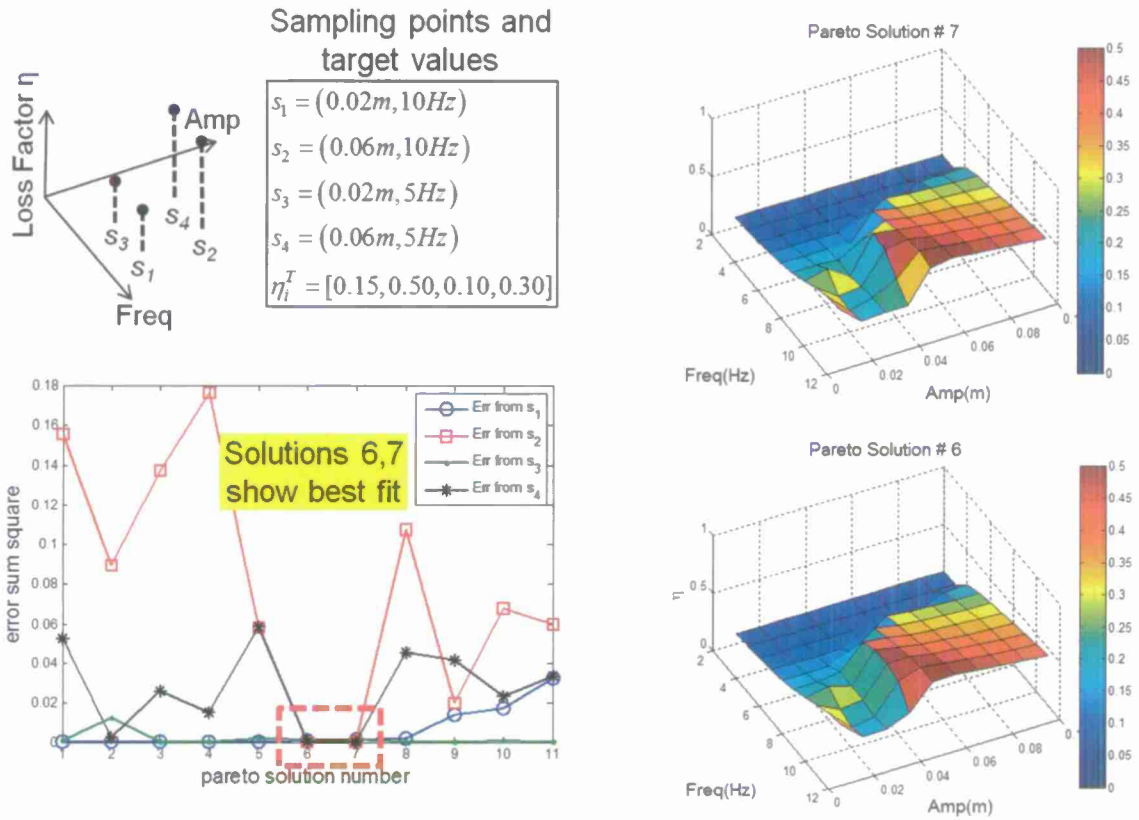

Figure IV-47: Results investigating the performance of multi-objective pareto-optimization for the synthesis of structural assemblies having pre-defined loss factor performance.

In this thrust we have accomplished two main results: (1) we have integrated the Simulink based model environment with a Genetic Algorithm approach to create a design and optimization framework able to synthesize structural assemblies according to the structural logic requirements, and (2) we performed numerical simulations using the newly developed optimization framework in order to synthesize optimal configurations for the fabrication of the periodic rod prototype.

Two main optimization approaches were investigated: the single objective and the multi-objective approach. The single objective function approach was mainly formulated to minimize the structural mass of the nonlinear appendages while still fulfilling the program metrics on the overall loss factor. The multi-objective function approach was instead investigated as a possible technique to design passively adaptive sub-assemblies.

By using the optimization framework, we have also synthesized two possible optimal configurations for the 3-cell and 10-cell periodic rod in order to support the fabrication of the final prototype.

Design of Structural Networks

The main objectives of this thrust were (i) to analyze the effect of nonlinear joints on the loss factor performance and (ii) to expand the Simulink-Matlab based framework to explore the design of structural networks (i.e. combinations of multiple sub-assemblies). In particular, we:

- Performed preliminary numerical investigation to evaluate the effect of nonlinear joints connecting multiple substructures and their effect on the overall loss factor performance.
- Updated the GA based algorithm (particularly, the chromosome definition) to handle structural networks assembled based on different combinations of blocks, connections, and parameters at sub-assembly and assembly level.

Approach and Accomplishments

The technical details concerning the updates to the GA code in order to account for the nonlinear joints and for the network design were discussed in the monthly reports and are not repeated again in this document.

Here below we report some of the main results of our numerical investigation on the effect of nonlinear joints on the loss factor performance. Multiple scenarios have been analyzed to understand the effect of either snap-through joints or different configurations of structural sub-assemblies.

Design strategy for the synthesis of mechanical networks

We first investigated the effects of different design factors of the mechanical network. In particular, we studied the effect of three main design parameters: (1) the sub-assembly configuration, (2) the joint type (linear vs. nonlinear spring), and (3) the number of substructures.

In case study (1) we investigated the effect on the loss factor produced by the sub-assembly configuration looking in particular to series and parallel connenctions. For this analysis we used the structure blocks defined in Figure IV-48. The series connection (Figure IV-48 (a)) does not require a level block because there are not shared DOFs between multiple substructures. On the contrary, the parallel connection (Figure IV-48(b)) does require one level block at the right end.

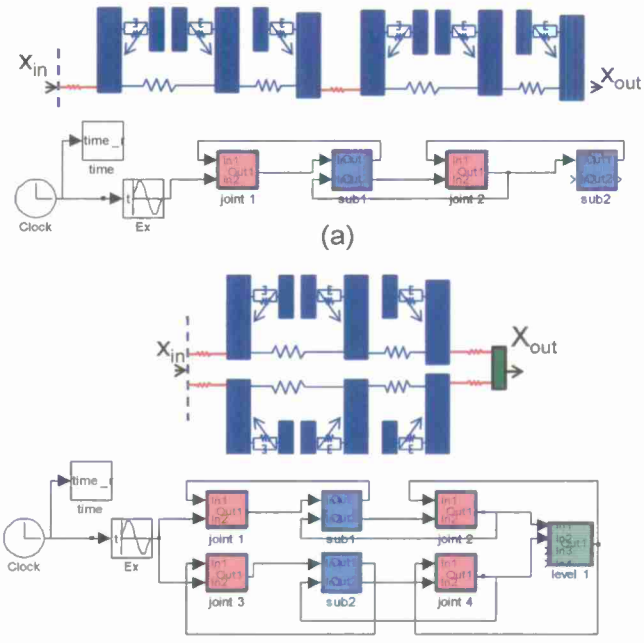

Figure IV-48: Schematic of two basic network configurations with the corresponding Simulink models. (a) series connection and (b) parallel connection.

In the case of two substructures connected in series, the loss factor is shown in Figure IV-49. The joint stiffness is chosen to be equal to the substructure stiffness so to not compromise the overall stiffness of the structural assembly. The loss factor performances are very similar to that of the single substructure. This result is not surprising given that connecting two substructures in series is equivalent to a single substructure (rod) with double length, mass and damping elements. This configuration results in higher dissipated and stored energy but does not alter their ratio, which ultimately determines the loss factor. A similar situation is obtained when the sub-structures are connected in parallel. The loss factor of the resulting assembly remains basically unchanged.

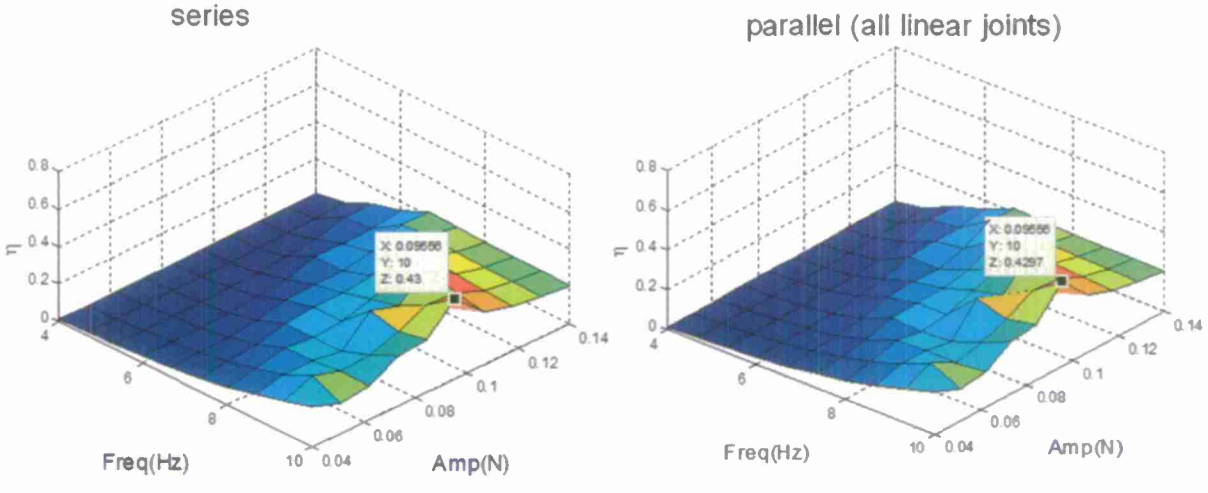

Figure IV-49: Loss factors for basic structural networks (series and parallel connection).

In order to improve the performance of the network, we investigated the use of nonlinear joints (case study 2). Preliminary analyses conducted using a snap-through joint type indicated that both adaptability and high loss factor performance can be achieved.

Figure Figure IV-50 shows a schematic view of the mechanical assembly used in this numerical study. The system consists in two substructures connected in parallel by using a combination of linear and nonlinear joints. The nonlinear joint is assumed to be a bi-stable (snap-through type) joint exhibiting a dynamic response qualitatively similar to the snap-through appendages. The two substructures are identical (as indicated in Figure IV-30), and the single substructure exhibits a maximum loss factor of 0.432. In the specific example only the joint 1 is assumed to be nonlinear. The nonlinear joint is modeled as a damper (c_{j1}) and snap-through spring (k_{j1} in Figure IV-30) connected in parallel. Joint 2, 3 and 4 are represented by linear springs.

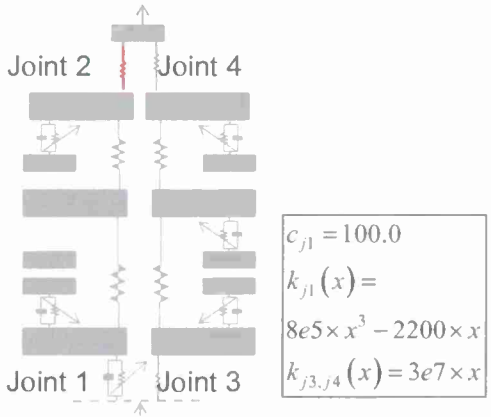

Figure IV-50: Schematic of the lumped parameters model having two identical substructures in parallel connected with a combination of linear and nonlinear joints. (Left) Substructure #1, (right) Substructure #2. Joint 1 is a bistable nonlinear joint. Joint 2, 3 and 4 are linear joints.

In an initial study, we investigated the effect of the linear stiffness of joint 2 (red element in Figure IV-50) on the overall performance. Two different stiffness values for the joint 2 were tested ($k_{j2}=3.e7$ and $k_{j2}=1.e3$). The corresponding loss factor provided by the two different structural networks is shown in Figure IV-43. When a high stiffness is used for joint 2, 3 and 4 the high stiffness of the assembly prevents substructure 1 (left) from snapping. When the stiffness of joint 2 is reduced ($k_{j2}=1e3$), the lower coupling with the substructure 2 allows the joint 1 to snap under the dynamic load produced by substructure 1. Its effect on the loss factor is shown in Figure IV-51 (b). The parameters of the snap-through devices in the substructures and in the nonlinear joint 2 are set to identical values, therefore the snap-through thresholds corresponding to the periodic snapping of both the substructures appendages and of the joint are coincident. A direct comparison between Figure IV-51 (a) and (b) shows how, when also the joint starts snapping, the overall loss factor increases of a factor 2.

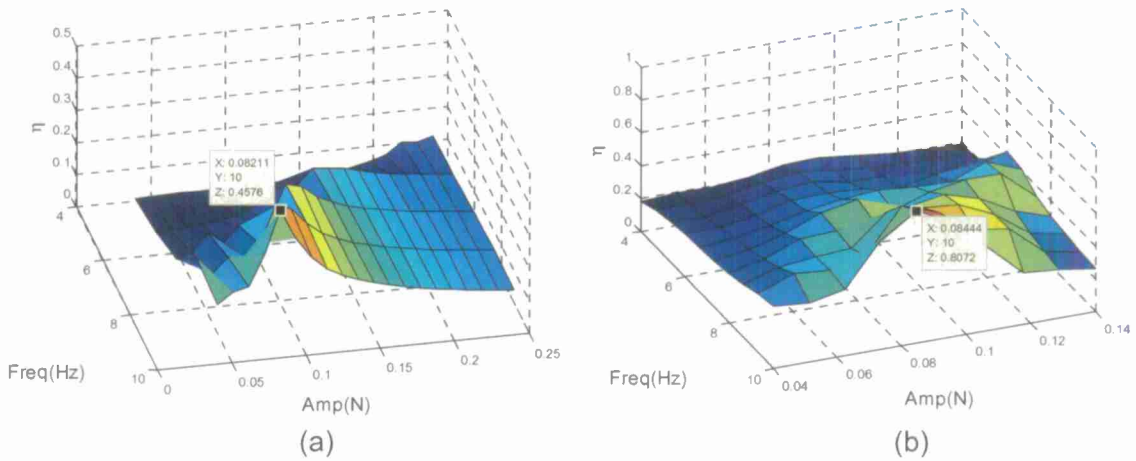

Figure IV-51: Loss factor with different stiffness values for the linear joint 2: (a) k_{j2}=3e7, (b) k_{j2}=1e3.

These preliminary results show that nonlinear joints can be successfully exploited to drastically increase the total loss factor of a structural network without increasing the overall mass of the system.

In the last case study (3), we investigated the effect of the number of substructures on the network performance. In particular, we analyzed the performance of an assembly made of three sub-structures connected in parallel. The schematic of the system is shown in Figure IV-52. Joint 1 and 3 are nonlinear joints composed of a damper (c_{j1}, c_{j3} in Figure IV-52) and a snap-through element (k_{j1}, k_{j3}) in parallel. Joint 2, 4, 5, and 6 are linear spring elements simulating the effect of a linear joint. The joint stiffness profile is shown in Figure IV-52 (b) and the corresponding Simulink model is displayed in Figure IV-52 (c). The system in Figure IV-52 is compared with the parallel connection with two substructures (as shown in Figure IV-50), with different joint stiffness ($k_{j1}=30\times(8e5\times x^3-2000x)$, red one in Figure IV-52 (a),(c)).

A preliminary assessment of the performance of the three sub-structure assembly can be made by comparing the loss factor plot with the corresponding plot from the two sub-structures subassembly (Figure IV-52(a)). Figure IV-52 (b) clearly shows the multiple thresholds can be obtained by using an increasing number of substructures. Also, the location of the thresholds (in terms of amplitude/frequency ranges) can be selected by a proper design of the substructure parameters. This result suggests that the mechanical network assembled based on combination of multiple sub-structures can offer a high degree of adaptability and tailoring of the dynamic performances.

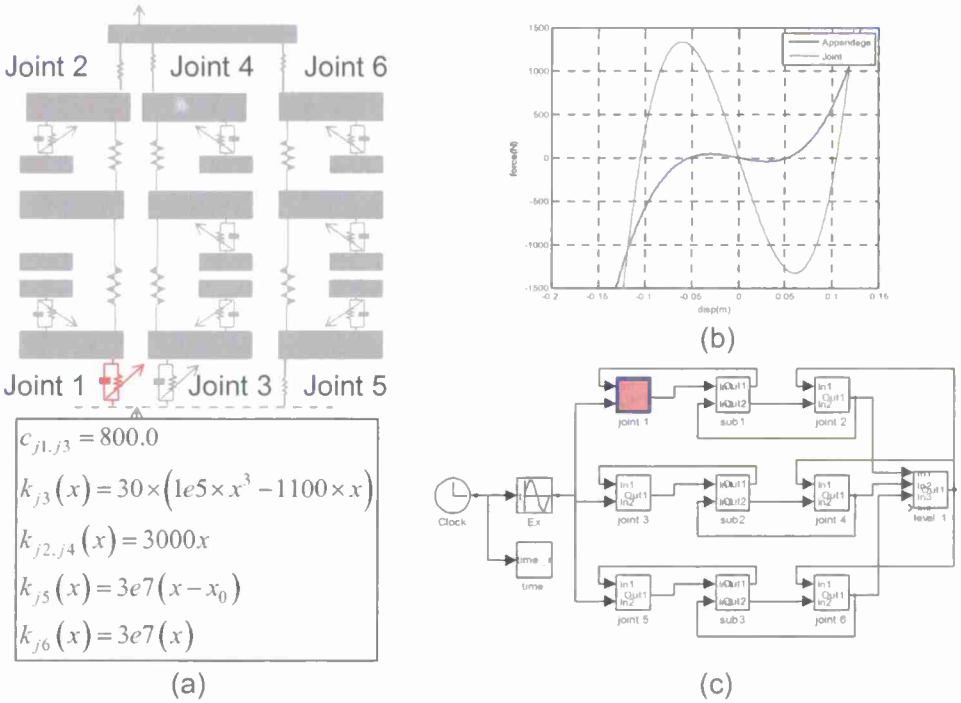

Figure IV-52: Parallel connection of 3 substructures: (a) schematic of the lumped parameter model (b) nonlinear stiffness with snap-through for appendage (blue) and joint 1 (green) (c) Simulink model.

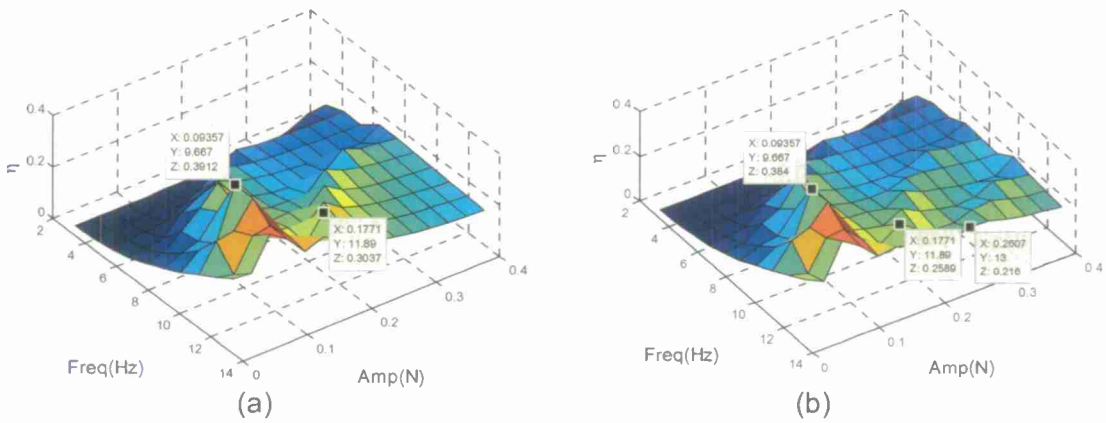

Figure IV-53: Loss factor plots for a network built using parallel connections: (a) two substructures, (b) three substructures.

Optimal network configuration by mixed-GA

The last topic we addressed in this thrust consisted in the development of the GA approach for network design. We expanded the design and optimization framework to be able to interconnect blocks in non-pre-defined manner, that is the internal sub-structure configuration as well as the type and configuration of the structural joints are selected by the GA algorithm. Both optimization strategies ((1) minimization of the total weight with constrained performance or (2) user-defined performance) can be implemented in the framework.

The framework was modified in order to automatically generate the Simulink dynamic model corresponding to the optimal configuration selected by the GA. The code uses the numeric data from the decoded chromosome to assemble the optimal configuration based on the building blocks available in the library: Substructure block, Joint block, and Level block. In future applications the library can be easily expanded to account for new building block types without requiring further modifications of the framework. Figure IV-54 shows a simple schematic example illustrating the decoded sequence for a possible mechanical connection and the corresponding substructure configuration. The first two fields in the chromosome contain the information on the connecting points for each substructure. The remaining fields are used to assign the physical parameters for each substructure and joint.

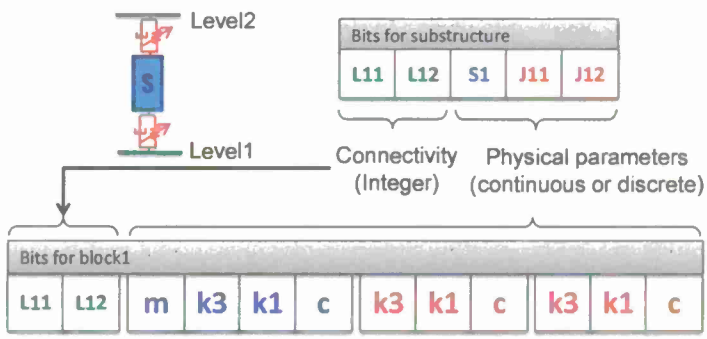

Figure IV-54: Schematic of the decoded chromosome and resulting design configuration. The S block indicate the "dummy" substructure, the spring-like elements represent the joints and the "L" elements indicate the interface level between substructures.

This schematic is automatically converted into a Simulink model that can be used to analyze the dynamic response of the assembly and to evaluate the equivalent loss factor. Figure IV-55 shows an example of the automatic generation of a network model using the proposed framework. The resulting Simulink model (bottom in model Figure IV-55) is constructed based on the connectivity information provided on the first two fields of the chromosome definition (top left in model Figure IV-55). The input excitation condition is assigned to the Level 1.

It is worth to note that this specific activity, concerning the network design, extended the actual scope of the original proposal. The results presented here are preliminary and the framework would need additional validation and further development in order to include important parameters in the optimization process, such as the number of the sub-structures (currently considered as a fixed input parameter). Nevertheless, these preliminary results indicate that the proposed GA based framework holds great potential for a structural logic approach. In

particular, it provides the ability to autonomously selecting structural elements from a pre-existing library, optimizing the structural parameters, selecting the joint type and parameters, and designing optimal network with either optimal or user-defined performance.

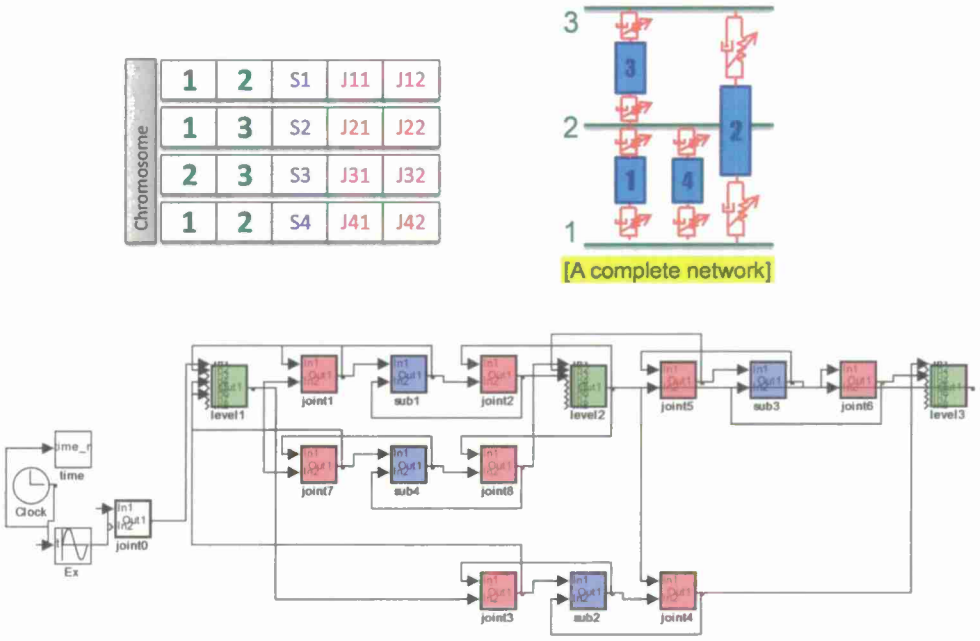

Figure IV-55: Example of network design configuration and of the corresponding Simulink model that is automatically generated by the framework based on the selected optimal configuration identified by the chromosome.

In this thrust, we have investigated the possibility to improve the performance of the structural assembly and provide further passive adaptive characteristics by exploring different options such as sub-assembly configurations, joint types and number of substructures. We also performed a preliminary investigation to explore the performance of a structural network (i.e. an ensemble of sub-assemblies).

Results have shown that the performance of the mechanical assemblies can be successfully improved and/or tailored if multiple sub-structures are connected via nonlinear joints. In this last case, results show a considerable increase in the overall loss factor performance as well as the ability to tailor the loss factor profile by introducing multiple thresholds (whose location can be controlled via substructure design). We also expanded the functionalities of the design and optimization framework by including network design capabilities. This version of the network design framework, although still limited in overall capabilities, shows a very promising approach for the design of complex mechanical assemblies according to the structural logic approach.

V. IMPORTANT FINDINGS AND CONCLUSIONS

We developed two designs of single snap through oscillator, rotational and translational, and developed analytical models and to investigate the performance. What follows are the major findings.

- The rotational device was demonstrated to be scalable with the following insights:
  - Scaling the vibration parameters (m, c_t, k) proportionally maintains performance
  - Scaling the geometry (L, R, l_0) proportionally requires a change in input amplitude Y and damping constant c_t to maintain performance
  - Scaling the geometry (L, R, l_0) proportionally down increases μ_t, making more effective use of available torsional damping
- Due to similarity in the governing equations, the translational device may scale in similar fashion, though explicit expressions were not derived.
- The translational device is a simpler design, easier to fabricate, and more robust for sub-assembly integration compared with the rotational device. Since it has similar performance also, it will be carried forward as the design of choice.
- Both the rotational and translational designs had similar qualitative performance, both predicted loss factor in excess of the Task 1 metric of 0.5, and both demonstrated adaptability to loading frequency and amplitude.

In terms of the prototype and fabrication and experimental characterizations:

- Translational bi-stable oscillator (building block) is modeled and tested. The bi-stable oscillator model predicts the behavior, both qualitatively and quantitatively, of the fabricated translational snap-through device. This fabricated device also meets the Program Task 1 metric for loss factor and stiffness.
- Sub-structure consists of translational snap-through devices coupled with linear oscillators. Through experiments performed on 10 cell sub-structure, it is demonstrated that the proposed design can effectively dissipate out energy from the primary structure and we have also achieved the Program Task 2 metric for loss factor.

In terms of the subassembly synthesis:

- Many configurations of building blocks were explored for the structural logic subassembly; two of the most successful configurations, nonlinear absorber with snap-through device and vibration absorber with snap-through device, were described herein to demonstrate the concept.
- Configuration II satisfies the entire Task II program metric, namely producing a loss factor greater than 1.0 over 1 to 10 Hz.
- Configuration II is highly adaptive, maintaining program metrics for loss factor over one magnitude of loading amplitude.
- Configuration II also responds quite effectively to shock loading.

VI. SIGNIFICANT HARDWARE DEVELOPMENT

Marine platform is one of the applications we have in mind for our structural logic concept. As shown in the Figure VI-1, the hollow pillar of the platform can be integrated with a series of inertial elements coupled with the bi-stable oscillators. As demonstrated through simulations, this kind of configuration will provide high and adaptable damping to the structure.

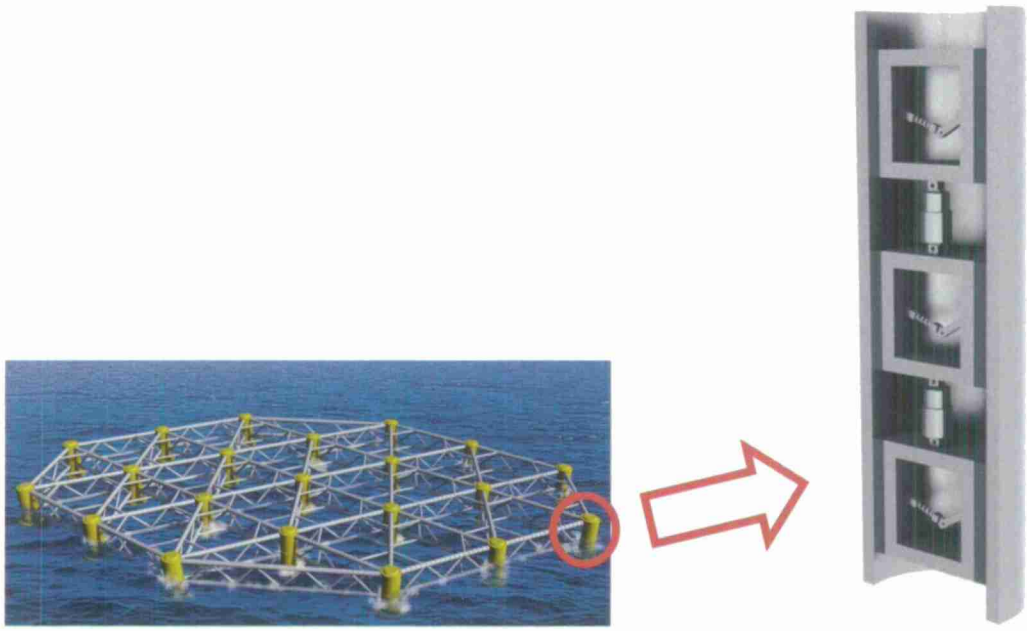

Figure VI-1: CAD model of a pillar of Marine Platform integrated with the structural logic concept developed

In order to verify these theoretical findings and to demonstrate Task 2 program metric, a laboratory setup is designed as shown in Figure VI-2. This laboratory setup represents and consists of all the features we want in the marine platform pillar. Moreover this laboratory setup can be easily debugged, tuned and evaluated in lab environment for proof of concept and validation

CAD Model

Based on the optimization results a ten-cell sub-structure is designed. CAD snapshots of the design is shown in the Figure VI-3

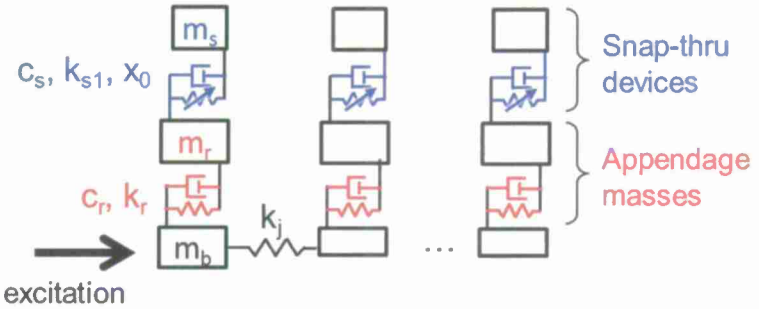

Figure VI-2: Schematic of Ten-cell structure

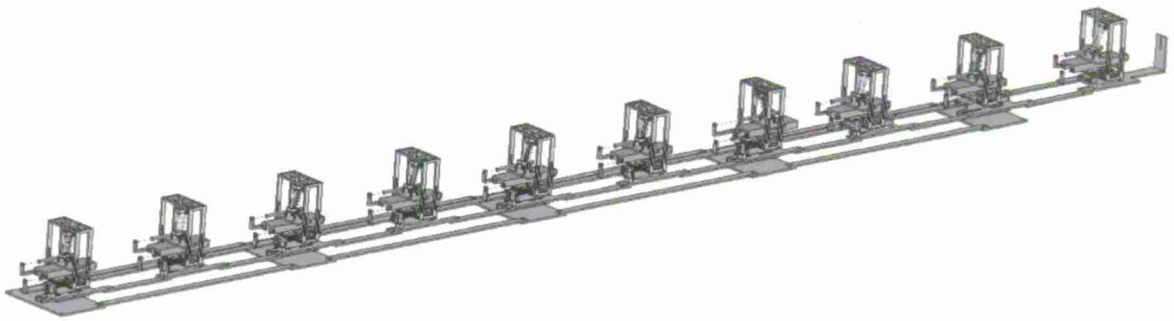

Figure VI-3: CAD model of ten-cell structure

The 10-cell structure can be divided into three layers in vertical direction. Bottom one is called Ground (Figure VI-4) and it supports all the moving parts. The middle one is called the Rod (Figure VI-5) and is attached to the Ground using a 4 inch stroke linear bearing. The top layer is composed of snap-through devices (Figure VI-6) and is attached to the Rod through springs/dampers. Their motion is constrained to the excitation direction by linear bearings.

Figure VI-4: Ground

Figure VI-5: Rod / Load Bearing Element / Primary Structure

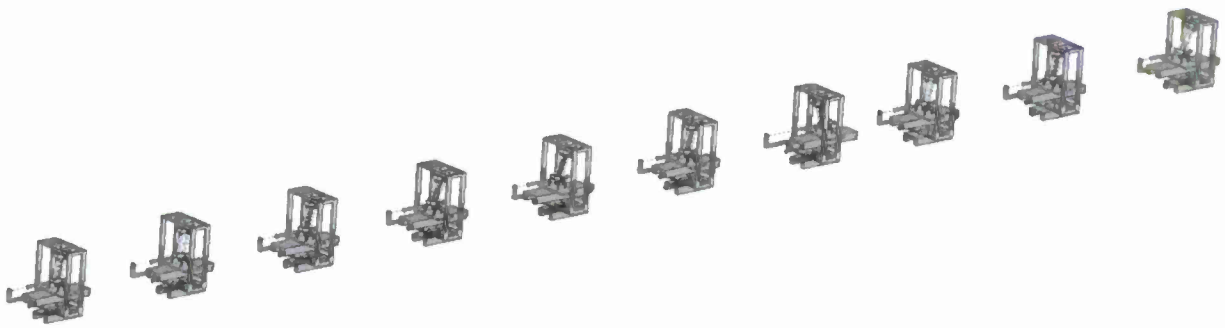

Figure VI-6: Snap-through Devices

(VI.1) 3-Cell Sub-Assembly Structure

Before building a 10-cell structure, a three-cell structure is built to verify the process and debug the system. This task will help us examine the manufacturability and assembly process. Since the optimization results couldn't be realized in the lab, we modified the parameters (

Table VI-1) to make the 3-cell structure realizable. The 3-cell structure is built as shown in Figure VI-7 and the experimental parameters are shown in Table VI-1. This structure is excited with various input frequencies and the loss factor of the system is evaluated.

Figure VI-7: Three-cell test bed

Table VI-1: 3-cell structure parameters

	X0(m)	Ks1(N/m)	Cs(N/m/s)	Cr(N/m/s)	Ms(kg)	Mr(kg)	Kr(N/m)
Cell1	1.5e-2	-16.05	1.5	1.5	0.30	1.420	1.133e+3
Cell2	1.5e-2	-19.26	1.5	2.3	0.37	1.546	2.288e+3
Cell3	1.1e-2	-15.43	1.5	1.5	0.30	1.000	3.618e+3

The displacement of the rod is recorded using a potentiometer and the force input to the system is measured using a force transducer. Data from these sensors is used to calculate the energy input and energy stored in the system and hence the loss factor of the system. Experimentally obtained loss factor data is plotted against the predicted loss factor data obtained using the model. As the results (Figure VI-8) demonstrate, experiment and simulation results match well.

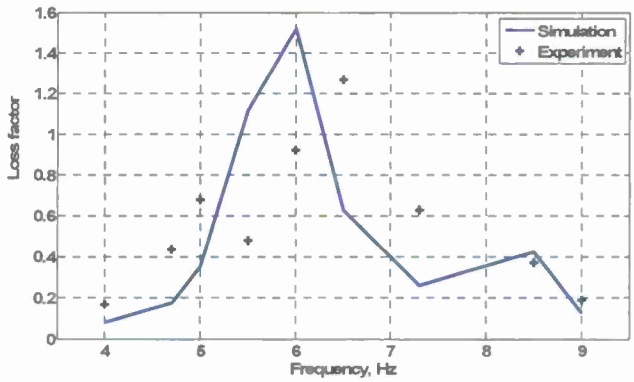

Figure VI-8: Experimental vs. predicted loss factor data

(VI.2) 10-Cell Sub-Assembly Structure

Having gained confidence in the model, a 10-cell structure as shown in Figure VI-9 is built to demonstrate the program metric. The parameters used to build this structure are shown in Table VI-2. Two tests were performed on the structure. In the first test, we excited the structure with harmonic load of different frequencies and the loss factor performance is evaluated. In the second test, we performed a transient test that demonstrates the effectiveness of the overall sub-assembly design.

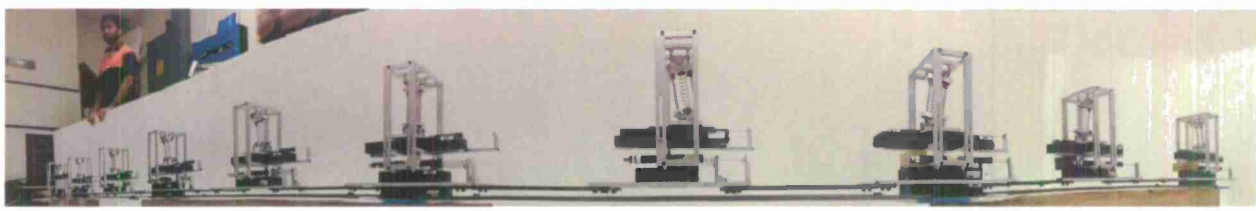

Figure VI-9: Panoramic view of 10 cell test bed

Table VI-2: 10-cell sub-structure parameters

	X0(m)	Ks1(N/m)	Cs(N/m/s)	Cr(N/m/s)	Ms(kg)	Mr(kg)	Kr(N/mm)
Cell1	0.009	-6.68	3.5	3.5	1.1	2.336	0.96
Cell2	0.015	-28.96	3	3	1.1	2.036	1.341
Cell3	0.009	-36.66	2.8	2.8	1.1	2.036	5.2
Cell4	0.013	-15.33	2.3	2.3	1.1	1.436	1.03
Cell5	0.009	-8.74	1.9	1.9	1.1	1.436	1.24
Cell6	0.015	-20.56	1.5	1.5	1.1	1.436	1.03
Cell7	0.015	-29.34	1.3	1.3	1.1	1.636	1.47
Cell8	0.007	-24.97	1.1	1.1	1.1	1.436	5.88
Cell9	0.05	-4.078	1.0	1.0	1.1	1.436	2.18
Cell10	0.015	-22.35	0.9	0.9	1.1	1.436	1.12

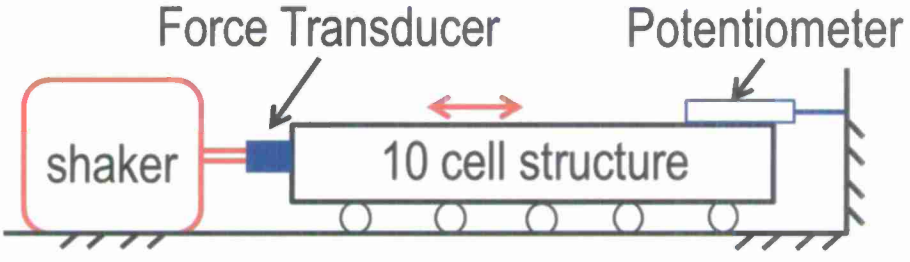

Figure VI-9: Schematic of test bed for Harmonic test

The schematic of test bed for Harmonic excitation is shown in Figure VI-9. The 10-cell structure is excited with various input frequencies and input amplitudes. Two kind of forcing amplitudes are used for the test. Because of hardware limitations (springs and bearings of few cells in the 10-cell structure are saturated), we could not excite the system with higher forcing amplitudes at lower input frequencies. We recognized that as long as we design the structure to be in periodic snap-through regime, we can achieve high loss factor. As shown in the loss factor profile shown in Figure VI-9, we have achieved loss factor over 1 for all frequency range and thus achieved the program loss factor metric.

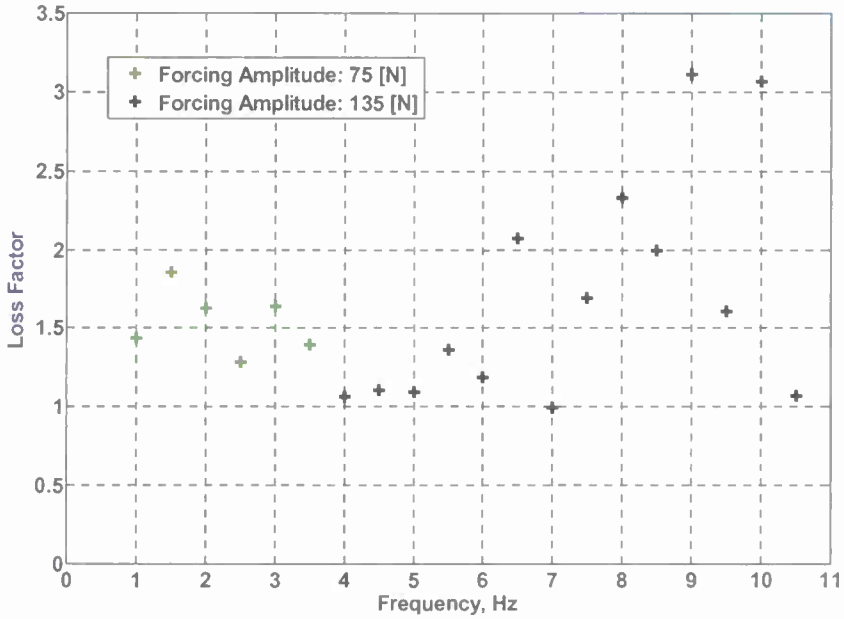

Figure VI-9: Experimentally obtained loss factor data for the 10 cell structure

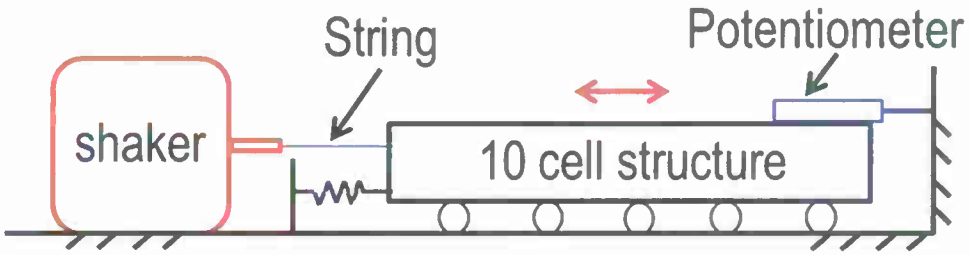

Figure VI-10: Schematic of test bed for transient test

The schematic of test bed for the transient test is shown in Figure VI-10. The 10-cell structure is attached to the ground via a spring and the structure is excited using a string and shaker arrangement. The structure is excited and the string is cut allowing the structure to shift from harmonic mode to transient mode. The overall response of the primary structure is recorded using a potentiometer.

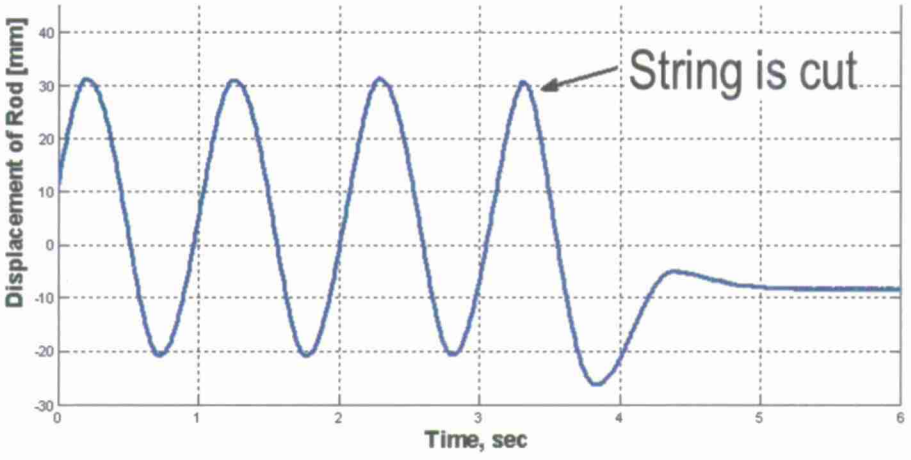

Figure VI-11: Transient response of the primary structure

The displacement of the primary structure dies out immediately after we stop pumping energy into the structure. These results as shown in Figure VI-11 demonstrate that the proposed sub-assembly design can effectively dissipate out energy from the primary structure.

(VI.3) Planar Snap-Through Units Attached to Beam Structure

In this thrust, we developed planar bistable snap-through devices as the basic building blocks and then synthesized into planar structure of beam with embedded snap-through devices sub-assembly structures. The objective is to develop bistable snap-through device in a planar configuration of for wider applications. The development evolution started off from planarization the proof-of-concept multi-part device, and then proceed to bitable metallic plate which can bulge out of the plane because of dimensional mismatch of the inner disk with the mounting holes. We then finally end up with a bistable dome and bistable arch, as shown in Figure VI-12. The shape of dome and arch provide the underlying geometry for bistable configuration. The dome and arch are made of viscoelastic material to increase the inherent damping. As a result, the viscoelastic arch functions both as the spring and damper, corresponding to the multi-part counterpart. Compare with metallic bistable plate, the snap-through threshold force of the viscoelastic arch is reduced so that it is easier to observe the triggering of snap-through action. In addition, the stroke span between two stable equilibrium positions is significantly increased, therefore, the amount of energy dissipated per cycle of snap-through is also increased.

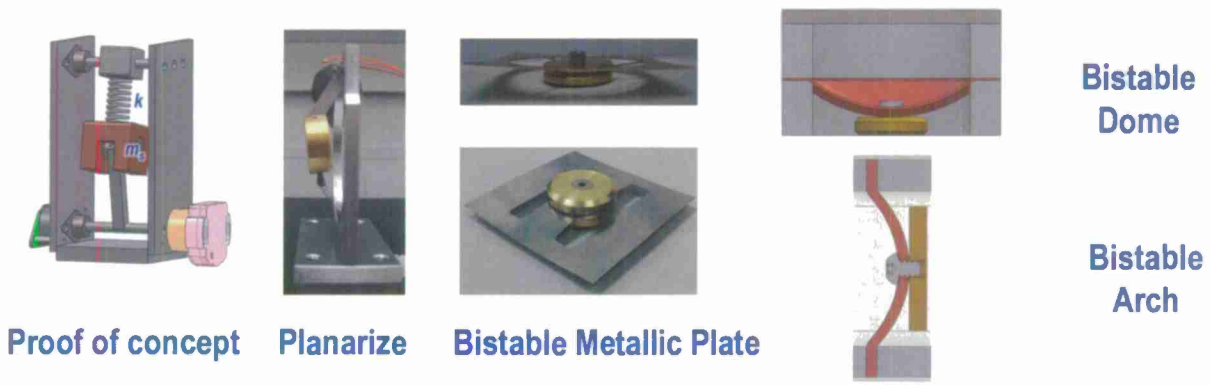

Figure VI-12: Development evolution path of planar bistable snap-through element

We then attach the developed bistable arch element to a linear structure to amplify the displacement, as shown in Figure VI-13.

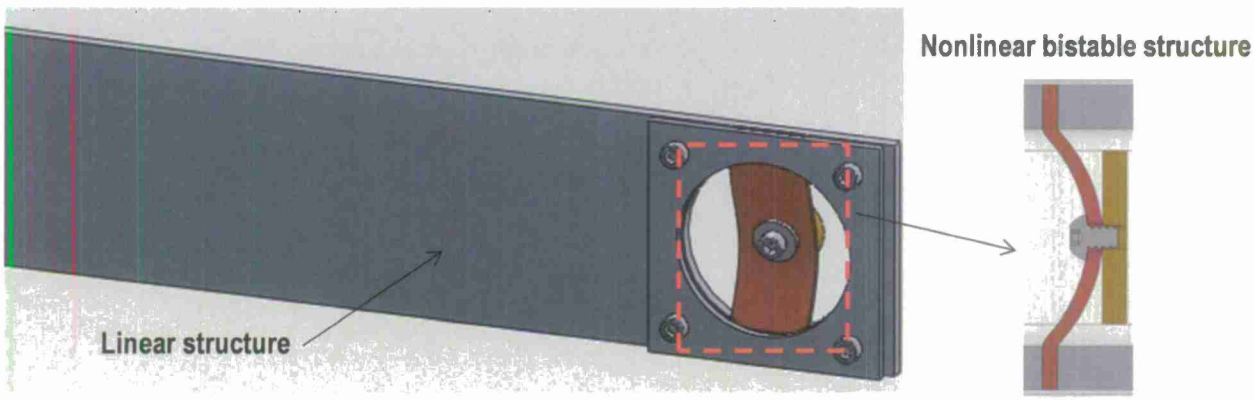

Figure VI-13: Beam structure with attached bistable structures

First, we performed detailed characterizations on the cantilever beam with attached snap-through units to investigate the overall structural performance on different snap-through configurations. The experimental setup is shown in Figure IV-14. The cantilever beam is attached to the shaker table by a fixture and excited by the horizontal vibration of the shaker table. The three snap-through units are mounted on the free end of the cantilever beam. One accelerometer is attached the shaker table as the reference input of the excitation and another accelerometer is attached at the tip of the beam free end to measure the output. The frequency response is measured as the output accelerometer at the tip compared with the input accelerometer of the shaker table.

Figure VI-14: Experimental setup of the cantilever beam with attached bistable snap through units

The shaker table is excited by a periodic sine chirp voltage signal. This excitation periodic sine chirp spans between 0.1 Hz and 120 Hz with a period of 8 seconds.

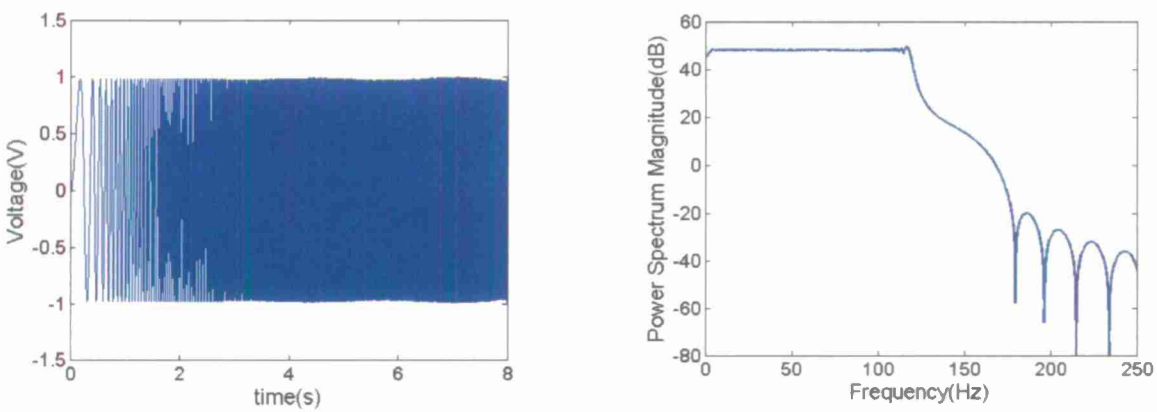

(a) (b)

Figure VI-15: periodic chirp signal to excite the shaker (a) time domain (b) frequency domain

A digital low pass filter is implemented to suppress unwanted high frequency components and reduce aliasing. The cut of frequency is at 165 Hz. The waveform was downloaded to a signal generator and it was used to drives the power amplifier in voltage mode. The time domain and frequency domain depiction of the excitation signal is shown in Figure VI-15.

Figure VI-16 shows the frequency response of the baseline cantilever beam vs. the beam with one unit of bistable snap-through at position closet to the free end. The two lowest resonant frequencies of the beam are 6.3 Hz and 34 Hz. The snap-through device significantly reduces the

response peaks at these two resonant frequencies. The first peak drops from 77.8 to 9.95 and the second peak drops from 174.72 to 19.58. In addition, the overall frequency responses drops for the frequency spectrum under investigation, which clearly demonstrate the snap-through device has a broadband frequency responses and is not just confined to a single resonant frequency of a conventional tuned mass damper.

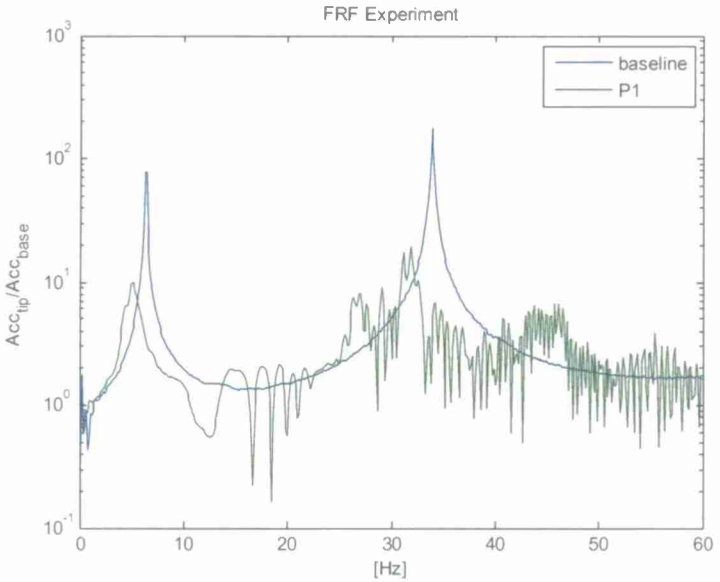

	Peak1	Peak2
baseline	77.81	174.72
P1	9.95	19.58

Figure VI-16: Frequency response: baseline cantilever beam vs. with one unit of planar bistable snap-through at position closet to the free end.

We then proceed to characterize the positional effect of the snap-through units. One single unit of bistable snap-through device is placed at three different positions, namely P1, P2, and P3, where P1 is the closet to the free end and P3 is closest to the fixed end, with a pitch distance of 3.25 inch between each position. When placing the snap-through unit at P1, the overall structure experienced the largest response drop at the two resonant peaks, at 9.95 and 19.59 respectively. When placing at the P2 position, the response is comparable with that of the P1 position, just slightly increase in it frequency response at both peaks (11.8 and 21.54 respectively). The configuration placing at P3 results in the worst performance and the frequency response increase dramatically at 49.83 and 102.64 but still significantly better than that of the baseline without any snap-through device attached. The results are shown in Figure VI-17.

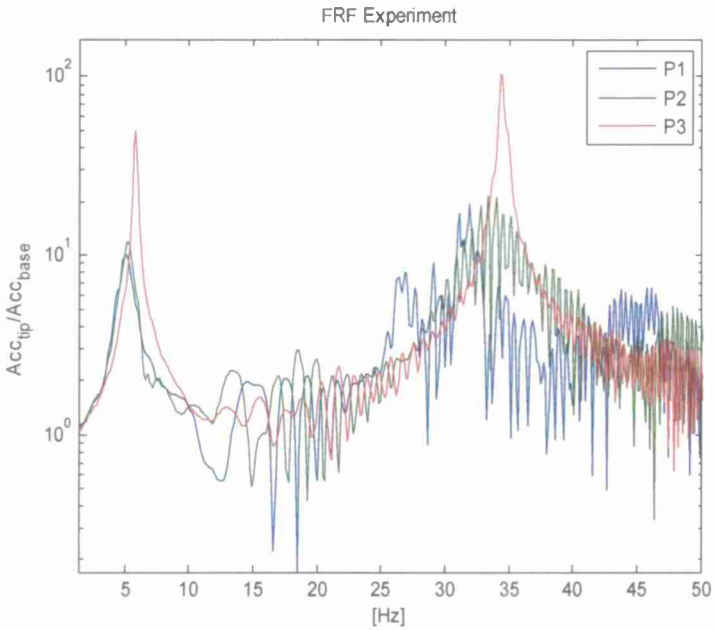

	Peak1	Peak2
P1	9.95	19.58
P2	11.80	21.54
P3	49.83	102.64

Figure VI-17: Frequency response on bistable snap-through at different positions.

Figure VI-18 shows the frequency response of the single snap-through unit vs. multiple units. The multiple-unit configuration comprises of three snap-through units and performs better at both the resonanee peaks: 6.61 vs. 9.95 for first resonant frequency and 6.61 vs. 9.95 for first resonant frequency and 10.90 vs. 19.58 for second resonance. Overall the 3-unit configuration outperforms single unit aeross the frequeney speetrum under investigation.

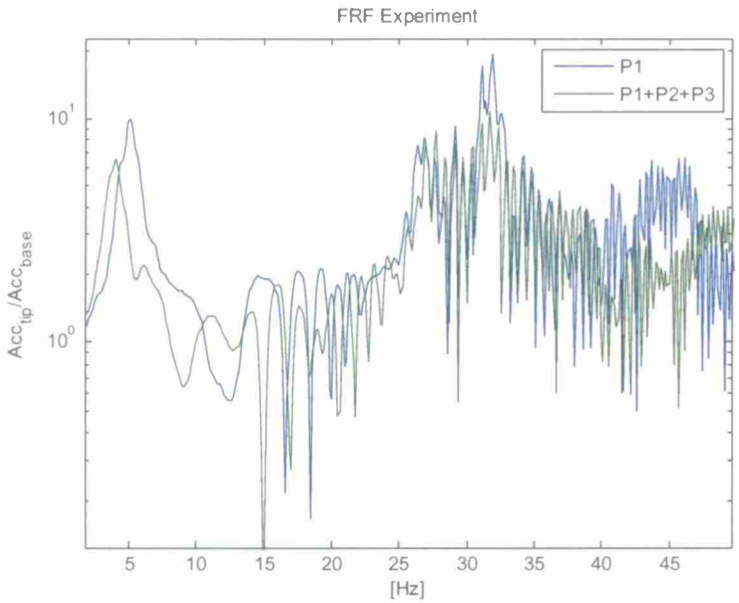

	Peak1	Peak2
baseline	77.81	174.72
P1	9.95	19.58
P1+P2+P3	6.61	10.80

Figure VI-18: Frequency Response of single unit of bistable snap-through vs. multiple units

We investigated the effect of snap-through mass on the frequency response. The 12.5g configuration is the baseline and double the weight (25g) as comparison. The result shows the double-weight configuration performs better than the baseline, at both the resonance peaks: 6.61 vs. 47.18 for first resonant frequency and 10.8 vs. 25.26 for the second resonance. As a result of the added mass, the first resonance drops. Overall the double-weight configuration outperforms single-weight unit across the frequency spectrum under investigation.

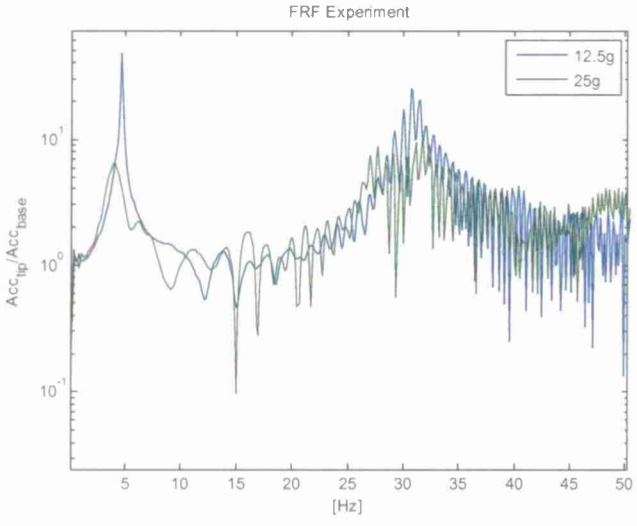

	Peak1	Peak2
12.5g	47.18	25.26
25.0g	6.61	10.8

Figure VI-19: Frequency response of single unit of bistable snap-through vs. multiple units

In addition, we also investigated the overall structural performance due to different snap-through configurations, especially on the bistable characteristics of the snap-through devices. Figure VI-20 shows the frequency response of the baseline cantilever beam vs. the beam with one unit and three units of bistable snap-through devices. The two lowest resonant frequencies of the beam are 6.3 Hz and 34 Hz at the baseline. The hangover length is configured to be 2 mm which is much smaller than the configuration reported in prior set of experiments. Figure VI-20 shows the frequency response of the overall single snap-through unit of different hangover length. The unit with larger hangover length (HL=20 mm) performs much better than that of smaller hangover length (HL=2 mm) for the device positioned close to the free end. The larger hangover length unit has higher energy dissipative capability than the smaller hangover length unit. The magnitude is lower at both resonance peaks: 41.40 vs. 9.95 for first resonant frequency and 30.22 vs. 19.58 for the second resonance. Overall the single snap-through device outperforms the baseline across the frequency spectrum under investigation.

For configurations of one units (Figure VI-20) and 3-unit (Figure VI-21), the snap-through device reduces the response peaks at these two resonant frequencies, compared with the baseline. The first peak drops from 100.43 to 41.40 and the second peak drops from 163.41 to 30.22 for the single device configuration, and the overall frequency responses drops for the frequency spectrum under investigation, which clearly demonstrate the snap-through device has broadband

frequency responses even for the snap-through device with short hangover length, which corresponds to smaller energy dissipation per unit oscillatory cycle.

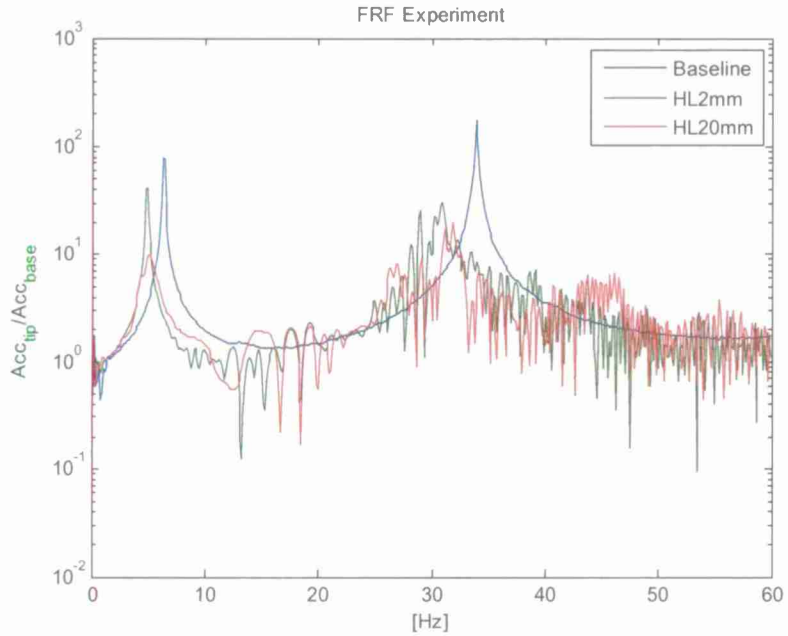

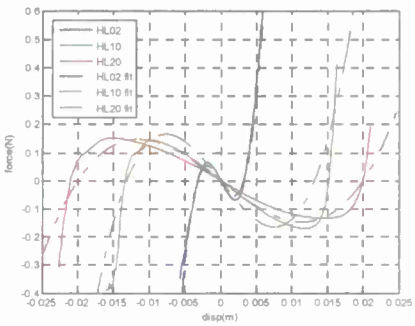

	Peak1	magnitude	Peak2	magnitude
baseline	6.4 Hz	100.43	34 Hz	163.41
HL 2 mm	4.9 Hz	41.4	31 Hz	30.22
HL 20 mm	5.1 Hz	9.95	32 Hz	19.58

Figure VI-20: Frequency response of single unit of bistable snap-through with different snap-through unit configuration (hang-over length)

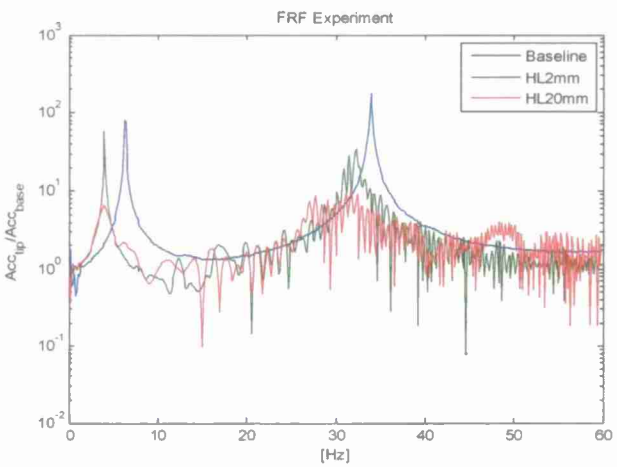

	Peak1	magnitude	Peak2	magnitude
baseline	6.4 Hz	100.43	34 Hz	163.41
HL 2 mm	4 Hz	57.97	32 Hz	34.93
HL 20 mm	4 Hz	6.61	32 Hz	10.8

Figure VI-21: Frequency response of 3-unit bistable snap-through with different hang-over length configurations

When adding more snap-through units to the overall sub-assembly structure, the 3-unit configuration does *not* further improve the performance, compared with that of the single unit. The added mass associated of the 3-unit configuration shifts the resonant frequencies, from 6.4Hz (baseline), to 4.9 Hz (1 unit) to 4.0 Hz (3 units) for the first peak and introduce additional

system wise kinetic energy, which may exceed the energy dissipative capability of shallow snap-through devices.

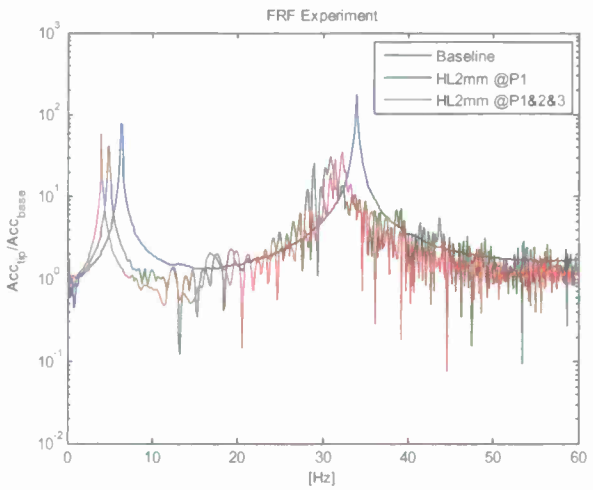

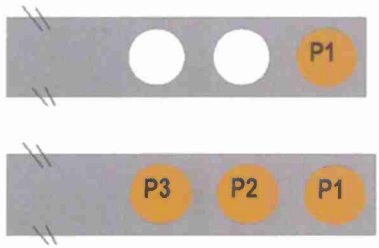

	Peak1	magnitude	Peak2	magnitude
baseline	6.4 Hz	100.43	34 Hz	163.41
P1	4.9 Hz	41.4	31 Hz	30.22
P1&P2&P3	4.0 Hz	57.97	32 Hz	34.93

Figure VI-22: Frequency response of baseline cantilever beam vs. bistable snap-through devices with short hangover length, single unit vs. multiple units

Bistable Composite Laminate

We developed bistable composite laminates with higher energy dissipative capability per unit than the arch-type bistable unit, with even higher stroke between bistable equilibrium positions. It is well known that an unsymmetrical laminates exhibit out-of-plane displacements at room temperature even if cured flat. The unsymmetrical sequence of composite laminate result in anisotropic thermal expansion. The out-of-plane displacements are caused by residual stress fields induced during the cooling process from the curing temperature to the room temperature. In the fabricated 0-90 composite sequence, the laminate assumes two cylindrical stable shapes. At the snap-through event, the composite laminate can change from one cylindrical shape into the other cylindrical configuration, as shown in Figure VI-23. When adding fours snap-through masses at the four edges to increase the inertial effort, the unsymmetrical composite laminate becomes an embodiment of the bistable snap-through device with desired characteristics: light weight and large stroke between two equilibrium position.

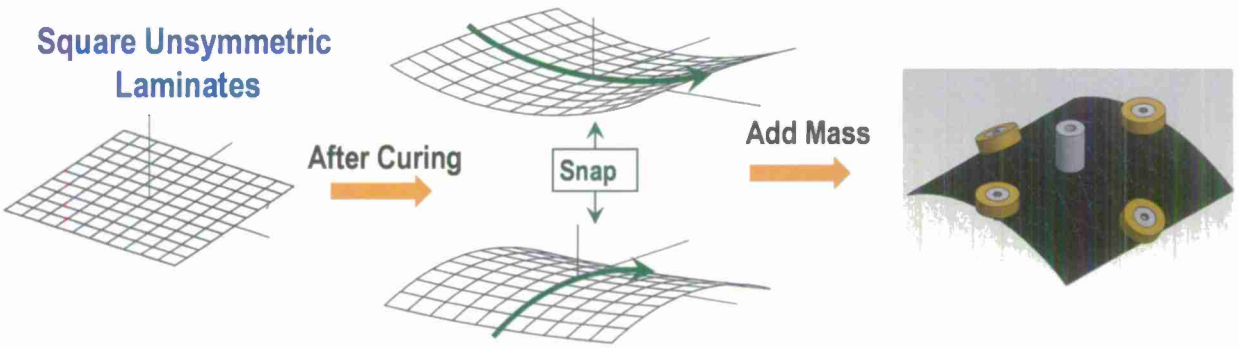

Figure VI-23: bistable snap-through laminate

We can design the bistable laminates to tailor its bistable characteristic features. Including Ply type, ply thickness, ply-angle. In addition, we can design the basic building block of bistable composite laminate with well-establish design and manufacturing protocols widely practiced by laminate composite industry.

We also performed simulation on the laminate plate to determine the force-displacement characteristic. The laminate consist of 0-90 plies. The simulation is performed by pining the four corners of the plate and applies force at the center of the plate. The obtained force-displacement profile is shown in Figure VI-24. The bistable equilibrium span is significantly increased, compared with the arch shape bistable structure.

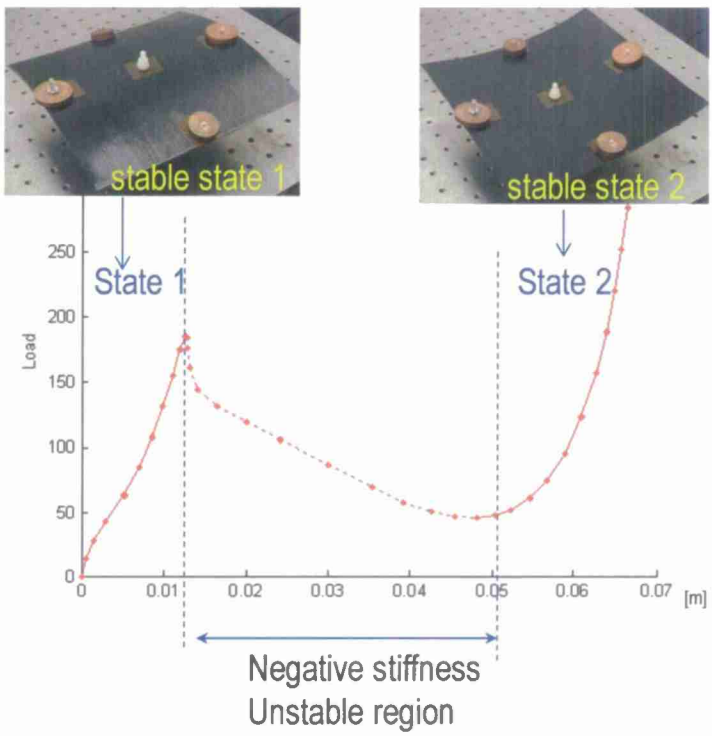

Figure VI-24: Simulation of bistable laminate, snap-through between two equilibrium configurations

We developed a sub-assembly of composite beam to demonstrate reaching program metrics. This composite beam consists of hybrid of snap-through units with three arch-shaped bistable units close to the tip of the free end and two bistable composite laminate attached near the middle of the composite beam. Because not enough clearance for housing two bistable composite laminate near the middle, we placed the bistable composite laminate units at both side of the composite beam. The fabricated sub-assembly of composite beam of hybrid snap-through units is shown in Figure VI-25.

This sub-assembly of composite beam is mounted on a shaker table to characterize its damping performance subject to harmonic excitation. The displacement/velocity of shaker table base is recorded using a laser vibrometer and the force input to the composite beam is measured

using a force transducer. These daya from these sensors is used to calculate the energy input and energy stored in the system and hence the loss factor of the system.

Figure VI-25: sub-assembly of a composite beam with hybrid bistable snap-through units.

Experimentally obtained loss factor data is plotted and shown in Figure VI-26. The result demonstrates the loss factor of the sub-assembly unit exceed 1.0 for the frequency spectrum of 1 to 10 Hz.

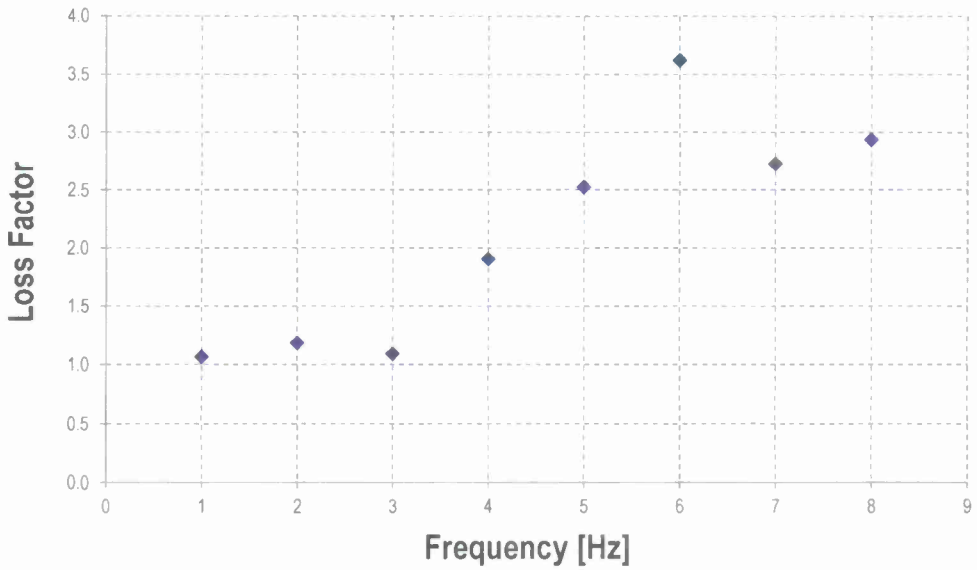

Figure VI-26: Harmonic Excitation Test Results

VII. SPECIAL COMMENTS

None

VIII. IMPLICATIONS FOR FURTHER RESEARCH

In this program, we have we have successfully demonstrated the we can improve the performance of the structural assembly and provide passive adaptive characteristics by exploring different design using the bistable snap-through units. Results have shown that the performance of the mechanical assemblies can be further improved and tailored if multiple building block of bistable snap-through unit and/or sub-structures are connected in a specially tailor fashion.

We expanded the functionalities of the design and optimization framework by including network design capabilities. Although the current version of the network design framework is limited to the two implemented configurations of the developed sub-assembly, ie. rod and planar beam configurations, it clearly manifests to be a very promising approach for the design of complex mechanical assemblies according to the structural logic approach. By combining structural logic sub-assembly of rod and planar configuration, we can present a futuristic rendering of a marine platform using these two configurations of sub-assembly structures as depicted in Figure VIII-1.

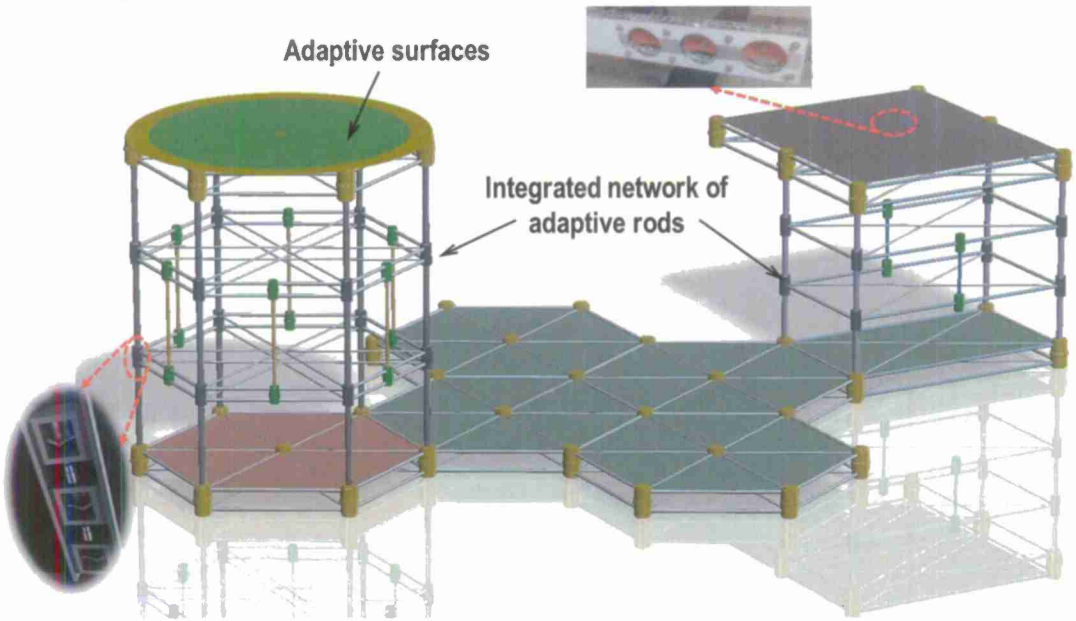

Figure VIII-1: Futuristic rendering of the demonstrated sub-assembly structure to be integrated on marine platform.

IX. REFERENCES

1. Allaei, D., and Tarnowski, D.J., 1997, "Enhancing the performance of constrained layer damping confining vibrational energy," Proceedings of ASME, Aetive/Passive Vibration Control and Nonlinear Dynamics of Structures, DE-Vol.95/AMD-Vol.223, pp. 31-46.
2. Arruda, J. R. F., and Mas, P., 1996, "Predicting and measuring flexural power flow in plates," Proc. SPIE, 2868, pp. 149–163.
3. Avramov K V and Mikhlin Y V 2004 Snap-Through Truss as a Vibration Absorber *J. of Vib. and Control* **10** 291–308.
4. Bouzit, D. and Pierre, C., 1992, "Vibration confinement phenomena in disordered, mono-coupled, multi-span beams," ASME Journal of Vibration and Acoustics, 114(4), pp. 521-530.
5. Buzhinskii V A 1989 Use of the snap-through membrane effect to limit dynamic loads *Mech. of Solids* **24** 40–5
6. Castanier, M.P. and Pierre, C., 1995, "Consideration on the benefits of intentional blade mistuning for the foreed response of turbomachinery rotors," IMECE AD55, pp. 419-425.
7. Cho S-W, Jung H-J and Lee I-W 2005 Smart passive system based on magnetorheological damper *Smart Mater. and Struct.* **14** 707–14.
8. Choi K M, Jung H J, Lee H J and Cho S W 2007 Feasibility study of an MR damper-based smart passive control system employing an electromagnetie induction device *Smart Mater. and Struct.* **16** 2323.
9. Choura, S., 1995, "Control of flexible structures with the confinement of vibrations," ASME Journal of Dynamic Systems, Measurement, and Control, 117(2), pp. 155-164.
10. Constans, E. W., et al., 1998, "The use of modal tailoring to minimize the radiated sound power of vibrating shells: theory and experiment," J. Sound Vib., Vol. 217(2), pp. 335-350.
11. Cornwell, P.J., and Bendiksen, O.O., 1989, "Localization of vibrations in large space reflectors," AIAA Journal, 27(2), pp. 219-226.
12. Daley, M. J. and Hambric, S. A., 2005, "Simulating and measuring structural intensity fields in plates induced by spatially and temporally random excitation," J. Vib. Acoust., 127, 451.
13. Elliott, S. J. and Johnson, M. E., 1993, "Radiation modes and the active control of sound power," Journal of Acoustical Society of America, Vol. 94, No. 4, pp. 2194-2204.
14. Fuller, C. R., 1990, "Active control of sound transmission/radiation from elastic plates by vibration inputs: I. analysis," J. of Sound and Vibration, 1990, 136 (1), pp. 1-15.
15. Gendelman O V and Lamarque C H 2005 Dynamics of linear oscillator coupled to strongly nonlinear attachment with multiple states of equilibrium *Chaos, Solitons & Fractals* **24** 501–9.
16. Hambric, S. A., and Szwerc, R. P., 1999, "Predictions of structural intensity fields using solid finite elements," Noise Control Eng. J., 47, pp. 209–217.
17. Hodges, C.H., 1982, "Confinement of vibration by structural irregularity," Journal of Sound and Vibration, 82(3), pp. 411-424.
18. Jensen, J. S., 2003, "Phononic band gaps and vibrations in one- and two-dimensional mass-spring structures," J. Sound Vibration, 266, pp. 1053-1078
19. Lakes, R. S., 2001a, "Extreme damping in compliant composites with a negative-stiffness phase," Phil. Mag. Lett., 2001, 81(2), pp. 95–100.

20. Lakes R S, Lee T, Bersie A and Wang Y C 2001b, Extreme damping in composite materials with negative-stiffness inclusions *Nature* **410** 565–7
21. Lakes, R. S., 2001c, "Extreme Damping in Composite Materials with a Negative Stiffness Phase," Phys. Rev. Lett., 86(13), pp. 2897-2900.
22. Lakes, R. S., 2004, "Extreme stiffness systems due to negative stiffness elements," Am. J. Phys., 72 (1), pp. 40-50.
23. Lee, C.-M., Goverdovskiy, V.N., and Temnikov, A.I., 2007 "Design of springs with negative stiffness to improve vehicle driver vibration isolation," J. Sound Vib., 302, pp. 865–874.
24. Li H, Liu J and Ou J 2011 Seismic response control of a cable-stayed bridge using negative stiffness dampers *Struct. Control and Health Monit.* **18** 265–88
25. Liu, Z., et al., 2000, "Locally Resonant Sonic Materials," Science 289, 1734.
26. Mester, S.S. and Benaroya, H., 1995, "Periodic and near-periodic structures," Shock and Vibration, 2(1), pp. 69-95.
27. Mignolet, M.P. and Hu, W., 1998, "Direct prediction of the effects of mistuning on the forced response of bladed disks," J. of Eng. for Gas Turbines and Power, 120, pp. 626-634.
28. Naghshineh, K. and Koopmann, G. H., 1993, "Active control of sound power using acoustic basis functions as surface velocity filters," J. Acoust. Soc. Am., 93(5), pp. 2740-2752.
29. Nashif, A.D., Jones, D.I.G., and Henderson, J. P., 1985, Vibration Damping, Wiley, NY.
30. Noiseux, D. U., 1970, "Measurements of power flow in uniform beams and plates," J. Acoust. Soc. Am., 47, pp. 238–247.
31. Pascal, J.-C., Loyau, T. and Carniel, X., 1993, "Complete determination of structural intensity in plates using laser vibrometers," J. Sound Vib., 161, pp. 527–531.
32. Pavic, G., 1976, "Measurement of structure-borne wave intensity. I. Formulation of methods," Journal of Sound and Vibration, 49, pp. 221–230.
33. Pierre, C., 1990, "Weak and strong vibration localization in disordered structures," Journal of Sound and Vibration, 126(3), pp. 485-502.
34. Pierre, C., and Cha, P.D., 1989, "Strong mode localization in nearly periodic disordered structures," AIAA Journal, 27(2), pp. 227-241.
35. Pierre, C. and Dowell, E.H., 1987, "Localization of vibrations by structural irregularity," Journal of Sound and Vibration, 114, pp. 549-564.
36. Platus D. L., 1999, "Negative stiffness mechanism vibration isolation systems," Proc. SPIE, 3786, pp. 98-105.
37. Richards, D., and Pines, D. J., 2003, "Passive reduction of gear mesh vibration using a periodic drive shaft," J. Sound Vib., 264(2), Pages 317-342.
38. Semperlotti, F., and Conlon, S. C., 2010, "Structural Damage Identification in plates via Nonlinear Structural Intensity Maps," JASA-EL, Vol.127 (2), pp. 48-53.
39. Shelley, F.J., and Clark, W.W., 1996, "Eigenvector scaling for mode localization in vibrating systems," AIAA Journal of Guidance, Control, and Dynamics, 19(6), pp. 1342-1348.
40. Sheng, P. et al., 2003, "Locally resonant sonic materials," Phys. B: Condens. Mat., 338, 201.
41. Sinha, A. and Chen, S., 1989, "A higher order technique to compute the statistics of forced response of a mistuned bladed disk assembly," J of Sound and Vib., 130(2), pp. 207-221.

42. Slater, J.C., Minkiewicz, G.R., and Blair, A.J., 1999, "Forced response of bladed disk assemblies – a survey," The Shock and Vibration Digest, 31(1), pp. 17-24.
43. Song, B.-K., and Jayasuriya, S., 1993, "Active vibration control using eigenvector assignment for mode localization," Proc. American Control Conference, pp. 1020-1024.
44. Tang, J. Liu, Y., and Wang, K. W., 2000, "Semi-Active and Active-Passive Hybrid Structural Damping Treatments via Piezoelectric Materials," Shock Vib. Digest, 32(3), 189.
45. Tang, J. and Wang, K. W., 2004, "Vibration confinement via optimal eigenvector assignment," ASME Journal of Vibration and Acoustics, 126(1), pp. 27-36.
46. Vakakis A F, Gendelman O V, Bergman L A, McFarland D M, Kerschen G and Lee Y S 2008 *Nonlinear Targeted Energy Transfer in Mechanical and Structural Systems* (Springer)
47. Wang, T., and Fuller, C. R., 1992, "Near-field pressure, intensity, and wave-number distributions for active structural acoustic control of plate radiation: Theoretical analysis," J. Acoust. Soc. Am., 92(3), pp. 1489-1498.
48. Wang Y-C and Lakes R 2004 Negative stiffness-induced extreme viscoelastic mechanical properties: stability and dynamics *Philos. Magazine* **84** 3785–801
49. Wu, T. Y. and Wang, K. W., 2007, "Periodic isolator design via vibration confinement through eigenvector assignment and piezoelectric circuitry," J. Vib. Cont., 13, pp. 989-1006.
50. Wu, T. Y. and Wang, K. W., 2008, "Vibration isolation via simultaneous left-right eigenvector assignment," Smart Materials and Structures, 17(1), 015048.
51. Wu, T. Y. and Wang, K. W., 2009, "Reduction of structural acoustic radiation via left and right eigenvector assignment approach," J. Intell. Mater. Syst. Struct., 20(18), pp. 2173-2186.
52. Yu, H. and Wang, K. W., 2007, "Piezoelectric networks for vibration suppression of mistuned bladed disks," ASME Journal of Vibration and Acoustics, 129 (5), pp. 559-566.
53. Yu, H. and Wang, K. W., 2009, "Vibration suppression of mistuned coupled-blade-disk systems using piezoelectric circuitry network," J. Vibration and Acoustics, 131(2), 021008.